

UNIVERSIDADE DE LISBOA
FACULDADE DE CIÊNCIAS
DEPARTAMENTO DE ENGENHARIA GEOGRÁFICA, GEOFÍSICA E ENERGIA



Dynamic triggering of seismic activity in rifting and volcanic settings

Miguel João Góis Ferreira Gaspar Neves

Mestrado em Ciências Geofísicas
Geofísica Interna

Dissertação orientada por:
Professora Doutora Susana Inês da Silva Custódio

Acknowledgments

First and foremost I would like to express my gratitude to Prof. Dr. Susana Custódio for giving me the opportunity to work with such interesting and intriguing theme. Her guidance, encouragement and time to hear all my doubts made this work possible.

I would also like to thank Prof. Zhigang Peng for his availability to review some of the results, answering some doubts that came up during the work and making available online the essential tools for the processing made. I would also like to acknowledge Prof. Graça Silveira for looking into some of the results and her suggestions and tips.

To everyone who was at the laboratory throughout this year thank you for the tips, opinions and the great work environment. Special thanks to Joana Carvalho for reviewing the geophysical and geological setting.

The most important acknowledgment of all goes to my family. To my parents, brother, sister and grandparents for believing in me and making possible for me to study what I like, for the encouragement and the incessant curiosity for what I was doing in this work and its status. To my father special thanks for helping me review the dissertation.

I cannot go without mentioning all the friends for their friendship and encouragement that made my path at the university easier. A special mention goes to Maria, Carolina and Lima whose support was very important in the final stages of this work.

Resumo

As interações entre sismos são importantes objetos de estudo em sismologia. O exemplo mais óbvio destas interações é o despoletar de réplicas que podem ocorrer após um sismo perto da fonte. Pensa-se que estas réplicas são despoletadas pela tensão estática que deforma o solo até uma distância de um a dois comprimentos de falha. Outro tipo destas interações é o despoletar de sismicidade a grandes distâncias devido à tensão dinâmica imposta pela passagem das ondas sísmicas. Este fenómeno chamado de *Dynamic Triggering* (sismicidade despoletada pela tensão dinâmica) foi reportado pela primeira vez por Hill *et al.* [1993] que observaram um aumento na sismicidade no Oeste do Estados Unidos após o sismo de magnitude 7.3 de 28 de Junho de 1992 em Landers. O aumento da sismicidade verificou-se até mais de 1250 km e iniciou-se na sua maioria durante a passagem das ondas de superfície. *Dynamic Triggering* é atualmente um fenómeno bem documentado, mas os mecanismos para sua ocorrência não são ainda completamente percebidos, existindo vários modelos propostos. É também habitualmente aceite devido a várias observações que estruturas vulcânicas podem ser afetadas pela passagem de ondas sísmicas. Este fenómeno pode ser uma importante ferramenta para perceber os processos que despoletam o movimento de uma falha, a nucleação de sismos e medir as tensões necessárias para uma falha movimentar-se e assim aumentar o conhecimento da mecânica dos sismos e melhorar os estudos de risco sísmico. Novas observações do fenómeno em diferentes ambientes são por isso essenciais para perceber os mecanismos que levam ao *dynamic triggering* e em que condições o fenómeno ocorre. De forma a fortalecer a relação causal entre o aumento da sismicidade e a passagem das ondas sísmicas vários testes estatísticos podem ser utilizados, sendo o mais utilizado a estatística β [Matthews and Reasenber, 1988; Aron and Hardebeck, 2009].

O *dynamic triggering* foi amplamente observado em regimes vulcânicos e distensivos. Este trabalho tem como objetivo procurar evidências de sismicidade despoletada pelas tensões dinâmicas impostas pelas ondas de superfície (*instantaneous dynamic triggering*) em quatro regiões onde este fenómeno não foi anteriormente estudado detalhadamente: Arquipélago de Cabo Verde, Moçambique e na Dorsal Mesoatlântica no vulcão submarino Lucky Strike e no Arquipélago dos Açores. Estes são ambientes vulcânicos e de *rifting* (regime distensivo).

Na região de Cabo Verde foram utilizados dados de duas redes sísmicas temporárias, uma composta por 7 estações de banda larga com três componentes instaladas entre 2002 e 2004 [Helffrich *et al.*, 2010] e outra instalada entre 2007 e 2008 no âmbito do projeto CV-Plume composta por 40 estações de banda larga com três componentes [Vales *et al.*, 2014]. A estes dados foram ainda adicionados os registos da estação SACV da rede sísmica global. Em Moçambique foram utilizados dados de uma rede temporária de 30 estações de banda larga com três componentes instalada no âmbito do projeto MOZART entre 2011 e 2013 [Fonseca *et al.*, 2014]. No vulcão Lucky Strike foram utilizados dados OBS (*Ocean Bottom Seismometer*) obtidos no âmbito do projecto MOMAR [Crawford *et al.*, 2013]. No Arquipélago dos Açores foram utilizados os dados das estações permanentes CMLA, da rede sísmica global, e ROSA, da rede sísmica portuguesa, localizadas em São Miguel e São Jorge, respetivamente.

Os eventos analisados foram escolhidos obtendo um catálogo de sismos do United States Geological Survey (USGS) com as seguintes características: magnitude ≥ 5.5 , profundidade ≤ 100 km, distância epicentral ≥ 100 km e tensão dinâmica estimada ≥ 1 kPa para a onda de Rayleigh de 20 segundos. Em Cabo Verde foram ainda analisados eventos adicionais com magnitude ≥ 7 , profundidade ≤ 100 km e distância epicentral ≥ 100 km. Para cada evento foram analisados os dados para as 6 horas antes e depois do tempo de origem do evento. Foi retirada a resposta instrumental aos dados e foram rodados para as componentes radial, transversal e vertical (nos dados de OBS esta rotação não foi feita). Os dados foram depois filtrados com um filtro passa-alto (>5 Hz), ou outro filtro no caso de existência de ruído local, e obtida a função envelope. Com a função envelope das três componentes foi calculada uma função envelope média das três componentes que foi utilizada na detecção dos sinais de alta frequência. A detecção de sinais de alta frequência e avaliação do seu aumento através da estatística β foram feitas utilizando um algoritmo de detecção automática STA/LTA (*short-term average/long-term average*) feito por Peng *et al.* [2014], baseado em Earle and Shearer [1994]. Foram utilizadas janelas STA e LTA de 2 e 10 segundos, respetivamente, para detetar sinais de alta frequência de curta duração e de 10 e 50 segundos, respetivamente, para detetar sinais de alta frequência de duração mais longa. Foi utilizada uma razão STA/LTA de 1.5 como *threshold*. β foi calculado comparando os sinais detetados na janela de *triggering*, entre a chegada das ondas com 5 e 2 km/s, com os sinais detetados antes da chegada da onda P. Valores de $\beta \geq 2$ indicam um aumento estatisticamente significativo da atividade de alta frequência. Todos os resultados foram depois inspecionados visualmente de forma a evitar falsos positivos.

Foram analisados 52 eventos sísmicos diferentes e foram utilizados dados de 88 estações sísmicas diferentes em 4 áreas de estudo diferentes. Nas 4 áreas de estudo foram detetados 6 possíveis casos positivos de *dynamic triggering*. Foi detetado um caso positivo de *triggering* em Cabo Verde, 2 casos em Moçambique e 3 casos no Arquipélago dos Açores. A sismicidade detetada é na sua maioria emergente e os sinais não foram detetados em mais de duas estações. Não foi por isso possível determinar as fontes dos sinais observados.

Na maioria dos dados de Cabo Verde é identificado um forte ruído cultural de alta frequência que pode estar a afetar os resultados. Apenas se detetou um resultado claro de aumento significativo em sinais de alta frequência na estação MLOS, na ilha do Fogo, durante a passagem das ondas sísmicas do sismo de 2002 de Denali, Mw7.9. Esta é uma estação que não apresenta o forte ruído cultural. Os sinais possivelmente despoletados pelo sismo estão numa banda de frequência também ocupada pelo ruído cultural observado nas outras estações. Outros dois casos onde foi identificado um aumento significativo generalizado nas ilhas noroeste e sudoeste durante a passagem das ondas de superfície ocorreram no período de aumento do ruído cultural. Uma análise mais aprofundada que permita determinar a origem dos sinais e distinguir os sinais despoletados pela tensão dinâmica do ruído cultural é necessária para melhor interpretar estes resultados.

Em Moçambique foi observado um claro aumento da atividade de alta frequência em quatro estações durante a passagem das ondas de superfície do sismo de 6 de Fevereiro de 2013 das ilhas Salomão, Mw8.0. Estas quatro estações estavam na área das estruturas tectónicas ativas identificadas em Moçambique. Nenhum sinal coerente foi observado entre as quatro estações e não foi possível uma localização e ligar claramente o aumento da atividade de alta frequência às estruturas tectónicas. Foi ainda identificado um aumento significativo na atividade de alta frequência numa estação no Cratão do Kapvaal, zona onde não estão identificadas estruturas ativas, durante a passagem das ondas sísmicas do sismo de 16 de Abril de 2013 de Saravan, Mw7.7.

Nenhuma evidência clara de *dynamic triggering* foi identificada no vulcão submarino Lucky Strike. Foram detetados problemas instrumentais nos dados que afetaram os resultados obtidos.

Os dados do Arquipélago dos Açores mostram que na ilha de São Jorge não foi registado nenhum aumento significativo da atividade durante a passagem das ondas sísmicas de vários eventos. Em Chã de Macela, na ilha de São Miguel foram registados vários casos de aumento de atividade significativos. Os sinais detetados são emergentes e parecem ser tremor. As ondas sísmicas podem estar a ativar as estruturas vulcânicas na ilha.

Estes resultados mostram que as regiões dos Açores, Cabo Verde e Moçambique são regiões onde podem ocorrer eventos despoletados pelas tensões dinâmicas impostas pelas ondas sísmicas (*dynamic triggering*).

Os resultados também sugerem que a sismicidade *triggered* pelas ondas sísmicas não tão frequente e comum como proposto por estudos anteriores.

Dados de estações mais protegidas de fontes de ruído cultural ou um método para melhor determinar quais os sinais do ruído cultural podiam melhorar as observações e a compreensão deste fenómeno nestas regiões. Nos Açores um estudo mais detalhado com dados de uma rede mais extensa e com maior cobertura ajudaria a confirmar as evidências detetadas na estação de Chã de Macela.

Palavras-chave: *Dynamic triggering*, Ondas de Superfície, Estatística β , Tremor

Abstract

Earthquake-earthquake interactions are still important questions of study in earthquake seismology. One of the most obvious example of these interactions are the aftershock sequence that can occur in the aftermath of mainshocks near the source. Since observations of the seismicity rate increase in Western United States at distances up to more than 1250 km after the Landers (Mw7.3) earthquake in California, 1992 [Hill *et al.*, 1993], widespread evidences for a new mode of interaction at remote distances has been recorded. This mode, called remote Dynamic Triggering, is now considered a robustly observed phenomenon. It is also widely recognized that volcanic structures can be affected by the passage of seismic waves from remote large earthquakes. The understanding of dynamic earthquake triggering could help improve the understanding of earthquake mechanics and therefore better assess seismic hazard by being a possible tool to study the processes that trigger slip on a fault, earthquake nucleation and to measure the stresses needed for a fault to fail. For this, a better understanding of the triggering mechanisms and the conditions for it to occur is necessary. More observations of the phenomenon could help address this questions.

The objective of this study is to search for evidence of dynamic triggering in four regions not thoroughly searched before for this phenomenon: Cape Verde, Mozambique and in the Mid-Atlantic Ridge in the Lucky Strike volcano and the Azores archipelago. These are volcanic and rifting (extensive regime) settings where the majority of remote dynamic triggering observations have been made. Events studied were chosen with the following criteria: epicentral distance ≥ 100 km, depth ≤ 100 km and magnitude ≥ 5.5 , with an estimated dynamic stress of the 20 second Rayleigh wave ≥ 1 kPa. For Cape Verde additional events with an epicentral distance ≥ 100 km, depth ≤ 100 km and a magnitude ≥ 7 were studied. With a STA/LTA automatic detection algorithm [Peng *et al.*, 2014] we assessed the statistical significance of the increase of high-frequency seismic energy during the passage of surface waves using a β statistics [Aron and Hardebeck, 2009]. $\beta \geq 2$ indicates a statistically significant increase. All results were visually inspected to avoid false positives.

A total of data from 52 different mainshocks was analysed and data from 88 different seismic stations was used in this study in 4 different study regions. In the 4 regions of study 6 cases of possible positive dynamic triggering were detected. One positive case was detected in Cape Verde, 2 cases in Mozambique and 3 cases in Azores. The observed seismicity is in its majority emergent and signals were not detected in more than two stations. Determination of the sources of the observed signals was therefore not possible.

In Cape Verde, a strong cultural noise with diurnal variation was identified. Only one clear case of significant increase in high-frequency seismic energy bursts was identified in the Fogo island in the Fogo volcano during the passage of the 2002 Mw7.9 Denali earthquake. The triggered signals identified in this case had frequencies in the same band of the cultural noise and so this noise could be masking triggered signals. Other two cases of increased high-frequency energy bursts with the passage of the seismic waves in the southwestern and northwestern islands were identified but these occurred in the period where the increase in cultural noise starts.

In Mozambique, a clear significant increase in high-frequency signals was identified in four stations in the area of Mozambique identified active structures during the passage of the February 6th, 2013 Mw8.0 Solomon islands earthquake. No coherent signals between the four stations were identified. During the passage of the April 16th, 2013 Mw7.7 Saravan earthquake a significant increase was identified in a single station in the Kapvaal craton.

No evidences of dynamic triggering were detected in the Lucky Strike volcano. Data had instrumental problems that affected the results.

In Azores, no evidence of dynamic triggering was found in the island of São Jorge a known seismic gap. Chã de Macela in São Miguel appears to be a location of repeated triggering. Signals detected are emergent and appear to be tremor-like. The seismic waves could be activating the volcanic structures in the area. A study with network with better coverage of the archipelago would help to better understand these results.

This results show that Azores, Cape Verde and Mozambique are areas where dynamic triggered seismic events may possibly occur.

The results also suggest that dynamic triggering is not so frequent and common as proposed by previous studies, particularly in the regions of study.

Data from stations deployed in locations better sheltered from cultural noise sources or a method to better constraint cultural noise signals would probably greatly improve the observations and the comprehension of the phenomenon in these regions.

Keywords: Dynamic triggering, Surface waves, β -statistic, Tremor

Contents

Acknowledgments	i
Resumo	iii
Abstract	vii
Contents	ix
List of Figures	xiii
List of Tables	xxi
1 Introduction	1
2 Dynamic Triggering	3
2.1 Seismic waves and their propagation through Earth	4
2.2 Triggering by dynamic stress changes	6
2.2.1 Microearthquakes	9
2.2.2 Tremor	9
2.3 Proposed models for the generation of dynamic triggering	11
2.4 Interaction between earthquakes and volcanoes	12
2.5 Triggering statistics	13
3 Geophysical and Geological Setting	15
3.1 Cape Verde	15
3.1.1 Tectonics and geology of the archipelago	15
3.1.2 Seismicity of Cape Verde	17
3.2 Mozambique	20
3.2.1 Geology and tectonics of Mozambique	20
3.2.2 Seismicity of Mozambique	23
3.3 Mid-Atlantic Ocean Ridge	25
3.3.1 Azores	25
3.3.2 Lucky Strike	27
4 Data	31
4.1 Deployments in Cape Verde	31
4.2 Mozambique - project MOZART	31
4.3 OBS deployments in the Lucky Strike Volcano	33

4.4	Permanent stations in the Azores Archipelago	35
5	Methods	37
5.1	Selection of distant mainshocks	37
5.2	Data processing	38
5.3	Burst detection and triggering statistics	39
6	Cape Verde	41
6.1	Results	41
6.1.1	Cultural Noise	45
6.1.2	The May 12th, 2008, Mw7.9 Eastern Sichuan and the June 30th, 2008, Mw7.0 South Sandwich Islands Region earthquakes (Mainshocks L and O)	47
6.1.3	Mainshocks with epicenter in the Mid-Atlantic Ridge (C, D, E and F)	49
6.1.4	The November 3rd, 2002, Mw7.9 Denali earthquake (Mainshock H)	51
6.2	Discussion	53
7	Mozambique	55
7.1	Results	55
7.1.1	February 6th, 2013 Mw8.0 Solomon islands earthquake (mainshock D)	57
7.1.2	April 16th, 2013 Mw7.7 Saravan earthquake (mainshock C)	57
7.2	Discussion	61
8	Mid-Atlantic Ocean Ridge	63
8.1	Lucky Strike volcano	63
8.1.1	Data problems	63
8.1.2	Results	65
8.1.3	Discussion	66
8.2	Azores archipelago	67
8.2.1	Results	67
8.2.2	Discussion	74
9	Conclusions	77
	Bibliography	79
	Appendices	85
A	Determined β-values for all stations and mainshocks in Cape Verde	87
B	Determined β-values for all stations and mainshocks in Mozambique	91
C	Determined β-values for all stations and mainshocks in Lucky Strike volcano	95
D	Determined β-values for all stations and mainshocks in Azores	97
E	Maps of β for all events analyzed in more than one station in Cape Verde not present in main text	99
F	Stations coordinates	105

G	Fittings for the analysis made in section 6.1.3. Results are shown in table 6.6	109
----------	--	------------

List of Figures

- 2.1 Diagram from *Kilb et al.* [2000] illustrating differences between static and dynamic stresses with distance in terms of idealized time histories for peak changes in dynamic (CFF(t)) and static (CFF) Coulomb stress. CFF(t) is the time dependent version of CFF (eqn 2.3). The double arrows show peak values for CFF(t) and CFF.[Adapted from *Hill and Prejean, 2007*]. 4
- 2.2 Global seismic ray paths and phase names, computed for the PREM velocity model. P waves are shown as solid lines, S waves as wiggly lines. The different shades indicate the inner core, the outer core, and the mantle. [From *Shearer, 2009*] 5
- 2.3 Three-component seismograms of the Mw6.0 Kyrgyzstan earthquake on the 19th of July 2011 recorded at station SUR in South Africa. The data have been rotated to the great circle path and Butterworth band-pass filtered between 0.0125-0.035 Hz. Seismograms are identified with P- and S-phases, as well as the surface waves (Love and Rayleigh). [From *Domingues, 2016*] 6
- 2.4 Examples of triggered seismicity detected within the surface wave coda from the Denali Fault earthquake at Mammoth Mountain. The top trace is a broadband seismogram, and the middle trace is a high-pass filtered version of the broadband record revealing the locally triggered activity as a spasmodic burst consisting of rapid-fire earthquakes. The bottom panel is a spectrogram of the broadband seismogram from station OMM located 4km southeast of Mammoth Mountain. Note the utility of the spectrogram display in revealing local earthquakes within the low-frequency coda as narrow vertical bands rich in high-frequency energy. Modified from *Prejean et al.* [2004]. [Adapted from *Hill and Prejean, 2007*] 7
- 2.5 Coulomb stress changes caused by the Joshua Tree, Landers, and Big Bear earthquakes mapped at a depth of 6.25km (halfway down the fault) and (M1) aftershock distribution during the 25 days following the Landers main shock. Source parameters are those used by *King et al.* [1994]. The location (open star) and the surface rupture (solid black line) of the M 7.1, 1999, Hector Mine earthquake epicenter is shown on the map. The Coulomb stress changes are plotted with a reduced amplitude (color) scale with respect to those of the previous figures. Redrawn from *King et al.* [1994] . [Adapted from *Hill and Prejean, 2007*] 8

2.6	Examples of triggered tremor during the surface waves of the 2001 November 14 Mw 7.8 Kunlun earthquake. (a) Broad-band transverse component seismogram recorded at station TPUB. The time is relative to the origin time of the Kunlun earthquake. The two arrows mark the approximate arrival time of the P and S waves. (b) 2–8 Hz bandpass-filtered transverse-component seismogram showing the high-frequency P waves and the triggered tremor during the passage of the Love waves. (c) The spectrogram of the transverse-component seismogram at station TPUB. The triggered tremor signals are shown as narrow vertical bands rich in high-frequency energy as compared with the teleseismic P and surface waves. [Adapted from <i>Peng and Chao, 2008</i>]	10
3.1	Cape Verde archipelago major islands with elevation. Location of the archipelago in the North Atlantic off the coast of africa	16
3.2	(a) Oblique 3-D image of Fogo and Brava, viewed from the southeast, based on swath bathymetry offshore and SRTM data onshore. (b) Plan (map) view of Fogo and the surrounding seafloor. Contours are at 200 m intervals with thousand meter contours in bold (orange, 1000 m; green, 2000 m; blue, 3000 m). The volcanic cones on the right of the image are on the lower slope of Santiago island. [Adapted from <i>Masson et al., 2014</i>]	18
3.3	Hypocentres of all locatable events registered between Nov. 2007–Sep. 2008 in the Cape Verde archipelago (red); final area selected for derivation of the 1D model and events complying with the selection criteria (black). To the bottom and left of the epicentral map are W–E and S–N vertical cross-sections. [From <i>Vales et al., 2014</i>]	19
3.4	Map with the location of Mozambique (MOZ) in Southeast Africa. Tanz - Tanzania; Zimb - Zimbabwe; SA - South Africa.	20
3.5	Hypsographic DEM of the East African rift system. Black lines: main faults; white surfaces: lakes; grey levels from dark (low elevations) to light (high elevations). The East African rift system is a series of several thousand kilometers long aligned successions of adjacent individual tectonic basins (rift valleys), separated from each other by relative shoals and generally bordered by uplifted shoulders. It can be regarded as an intra-continental ridge system comprising an axial rift. [Adapted from <i>Chorowicz, 2005</i>]	21
3.6	Simplified map of Mozambique with the main geological and tectonic units. ZC—Zimbabwe craton; LB—Limpopo; KC—Kapaal craton. [From <i>Domingues et al., 2016</i> , and references therein]	22
3.7	Preliminary locations of the earthquakes recorded during the first half of the MOZART deployment (April 2011 to July 2012). The map view of all the epicenters with horizontal uncertainty below 10 km (307 events). A joint focal mechanism solution is shown for four earthquakes with $M_L > 2.4$ located in the Urema graben, inside the outlined rectangle (P-wave first motions, 21 polarities, 3 violations). [Adapted from <i>Fonseca et al., 2014</i>]	24
3.8	Location of the Azores archipelago and the Lucky Strike volcano (black box) in the North Atlantic. The red thin line marks the Mid-Atlantic Ocean Ridge.	25

3.9	Azores region main tectonic structures. The shaded area represents the sheared western segment of the Eu–Nu plate boundary. Lithospheric plates: NA, North America; Eu, Eurasia; Nu, Nubia. Tectonic structures: MAR, Mid-Atlantic Ridge; NAFZ, North Azores Fracture Zone; WAFZ, West Azores Fracture Zone; TR, Terceira Rift; EAFZ, East Azores Fracture Zone; GF, Gloria Fault; EAVTS, East Azores Volcano-tectonic System. Islands: C, Corvo; Fl, Flores; F, Faial; P, Pico; SJ, São Jorge; G, Graciosa; T, Terceira; SM, São Miguel; Fo, Formigas islets; ST, Santa Maria. Azores bathymetry adapted from <i>Lourenço et al.</i> [1997] and world topography and bathymetry from GEBCO_08 database 2010. [From <i>Gaspar et al.</i> , 2015]	26
3.10	Historical seismicity and volcanism in the Azores archipelago. a) Epicentral locations of destructive earthquakes during historical times. b) Location of historical eruptions. [Adapted from <i>Gaspar et al.</i> , 2015, and references therein]	28
3.11	Maps of the Lucky Strike volcano. (A) The solid contour outlines Lucky Strike volcano. (B) Volcano scale. Solid contours are isodepths outlining the volcano base (1900 m beneath sea level (mbsl)), the western volcanic ridge (1660 mbsl), the summit depression (1710 mbsl) and its three surrounding peaks (1660 mbsl). Red dashed line marks the bounds of the Axial Magma Chamber (AMC) reflector. Black dashed lines mark significant surface faults. Black crosses mark hydrothermal vents. Circles mark OBS sites deployed in the MOMAR project cruises (blue (outer) 2007–2008, red (inner) 2008–2009) (section 4.3). [Adapted from <i>Crawford et al.</i> , 2013, and references therein]	29
3.12	Across-axis cross-sections of seismic events located by <i>Crawford et al.</i> [2013] and subsurface structure. Solid lines=faults imaged using seismic reflection data, dashed lines=faults extrapolated from seafloor observations. Dashedgrey line=AMC reflector. (A) Cross-section across the central graben north of the hydrothermal field. (B) Cross-section across the hydrothermal field, with seafloor hydrothermal discharge zones indicated in grey.(C) Cross-section across the south peak. [Adapted from <i>Crawford et al.</i> , 2013]	30
4.1	Locations of the stations from the two temporary deployments and the permanent SACV station. A) 2002-2004 deployment and SACV station from the Global Seismological Network. B) 2007-2008 deployment. Coordinates of stations are given in appendix F.	32
4.2	Locations of the stations from the MOZART deployment between 2011 and 2013. Red triangles - Taurus stations; Blue squares - Guralp stations; Green circles - stations of Africa Array. Coordinates of stations are given in appendix F.	32
4.3	Locations of the OBSs deployed as part of the MOMAR project. A) BBMOMAR I; B) BBMOMAR II; C) BATHYLUCK09; D) MomarSat2010. Coordinates of OBSs are given in appendix F.	34
4.4	Abrupt jump in data observed in several OBS stations. This was recorded in station D1 before the arrival of mainshock C that will be analyzed in section 8.1	35
4.5	Locations of the permanent stations in Azores. ROSA station is located in São Jorge island and CMLA in São Miguel island. Coordinates of stations are given in appendix F.	36

5.1	Example of a STA/LTA automatic detection algorithm to determine phase arrivals. (a) Short-period seismogram with autopicks plotted as vertical lines. (b) Envelope function and STA-LTA windows. The LTA and STA windows have been enlarged for visualization. (c) STA/LTA ratio (solid) and threshold (dashed). The trigger points are the intersections of the increasing STA/LTA ratio and the threshold. The pick times (vertical lines) are defined by the inflection point that precedes the local maximum immediately following the trigger point. [Adapted from <i>Earle and Shearer, 1994</i>]	39
6.1	Map of 20 mainshocks (tables 6.1 and 6.2) analyzed in Cape Verde (CV - green triangle). The epicenters are marked by the yellow stars. Mainshocks have $M_w \geq 5.5$ and hypocentral depths ≤ 100	41
6.2	Data analyzed for mainshock L in station CVFG4. a) Raw vertical component; b) 5 Hz high-pass filtered vertical component; c) Vertical component spectrogram. An increase in high-frequency energy bursts occurs during the passage of the surface waves that is sustained after the surface wave train end.	43
6.3	Data analyzed from station CVFG3 for mainshock Q . a) Three-component average envelope; b) STA/LTA ratio; c) Raw transverse component; d) Raw vertical component; e) 5 Hz high-pass filtered vertical component. Green line marks the manual picked P-wave arrival; Red lines delimit the triggering window. An increase in detected high-frequency signals occurs during the passage of the seismic waves.	45
6.4	Data analyzed from station MLOS for mainshock H . a) Three-component average envelope; b) STA/LTA ratio; c) Raw transverse component; d) Raw vertical component; e) 5 Hz high-pass filtered vertical component. Green line marks the manual picked P-wave arrival; Red lines delimit the triggering window. An increase in detected high-frequency signals occurs during the passage of the seismic waves.	46
6.5	Dayplot of the 5 Hz high-pass filtered vertical component envelope from station CVFG4, from 2008/05/02 to 2008/05/12 (day of mainshock L)	46
6.6	Maps with the registered β 's during the passage of the mainshocks L (figure A) and O (figure B) surface waves. Red circles represent stations with a significant increase in high-frequency activity and blue a significant decrease. A generalised increase is observed in the more western islands.	47
6.7	Example of a case where the increase in high-frequency activity during the passage of mainshock O seismic waves appears to start with the arrival of the S-wave. a) Three-component >5 Hz average envelope; b) Raw transverse component; c) Raw vertical component; d) 5 Hz high-pass filtered vertical component. Detections are marked by the red and yellow circles. The first vertical line (green) corresponds to the picked P-wave arrival and the next two red lines delimit the triggering window.	48
6.8	Surface waves from mainshock L recorded at station CVFG4. a) Transverse (top) and vertical (bottom) 0.01-1.0 band-pass filtered components; b) 3-component >5 Hz average envelope; c) 5 Hz high-pass filtered vertical component. Yellow lines mark the start of some of the high-frequency detected signals. These appear to start near a surface wave velocity maximum.	48

6.9	Surface waves from mainshock O recorded at station CVSN2. a) Transverse (top) and vertical (bottom) 0.01-1.0 band-pass filtered components; b) 3-component >5 Hz average envelope; c) 5 Hz high-pass filtered vertical component. Yellow lines mark the start of some of the high-frequency detected signals. These appear to start near a surface wave velocity maximum.	49
6.10	Two high-frequency bursts observed during the passage of mainshock J in MAIO station (blue circles). These bursts were observed in all the stations. The thin blue dashed lines mark the theoretical arrivals of the S, SS and sS waves, using the <i>iasp91</i> model. a) Three-component average envelope; b) Raw transverse component; c) Raw vertical component; d) 5 Hz high-pass filtered vertical component. Green vertical line corresponds to the manual picked P-wave and the red lines delimit the triggering window.	50
6.11	Nonlinear least-squares Marquardt-Levenberg fitting of $r = vt$ linear function (green line) to the distance of the stations to the epicenter (r) and the determined arrival times (t) of the observed second burst (in purple) for mainshock E . The fitting parameter corresponds to the average propagation speed with a result of 1.560 ± 0.002 km/s equal to the observed approximate propagation speed of the T-wave.	50
6.12	Mainshock H recorded in station MLOS. a) Raw vertical component; b) 5 Hz high-pass filtered vertical component; c) Vertical component spectrogram. High-frequency energy bursts are detected during the passage of the surface waves and similar signals occur after the surface wave train end. This result does not appear to be affected by the strong cultural noise.	52
6.13	Surface waves from mainshock H recorded at station MLOS. a) Transverse (top) and vertical (bottom) 0.01-1.0 band-pass components; b) 3-component >5 Hz average envelope; c) 5 Hz high-pass filtered vertical component. Yellow lines mark the start of some of the high-frequency detected signals. These appear to start near a surface wave velocity maximum.	52
7.1	Map of mainshocks (table 7.1) analyzed in Mozambique (green triangle). The epicenters are marked by the yellow stars. Mainshocks have $M_w \geq 5.5$ and hypocentral depths ≤ 100	56
7.2	Clipped records of the vertical components during the passage of the Rayleigh waves of mainshock A in stations 3901 (A) and 3A16 (B). In high-passed >5 Hz seismograms several impulsive bursts followed by periods of absence of movement are recorded.	57
7.3	A significant increase in high-frequency activity is recorded in 4 stations in the northern part of the study area in Mozambique (Red circles).	58
7.4	Data analyzed from station A0302 for mainshock D . a) Three-component average envelope; b) STA/LTA ratio; c) Raw transverse component; d) Raw vertical component; e) 5 Hz high-pass filtered vertical component. Green line marks the manual picked P-wave arrival; Red lines delimit the triggering window. An increase in detected high-frequency signals starts with the arrival of the Love wave.	58
7.5	Mainshock D recorded in station A0302. a) Raw vertical component; b) 5 Hz high-pass filtered vertical component; c) Vertical component spectrogram. An increase in high-frequency energy bursts with a tremor-like signal is detected during the passage of the surface waves.	59

7.6	Zoom of figure 7.5, from the mainshock origin time to the end of the surface train. a) Raw vertical component; b) 5 Hz high-pass filtered vertical component; c) Vertical component spectrogram.	59
7.7	Surface waves from mainshock D recorded at station A0302. a) Transverse (top) and vertical (bottom) 0.01-1.0 band-pass filtered components; b) 3-component >5 Hz average envelope; c) 3-5 Hz band-pass filtered vertical component. Yellow lines mark the start of some of the high-frequency detected signals. These appear to start near a surface wave velocity maximum.	60
7.8	Data analyzed for mainshock D recorded in station 3A16. a) Raw vertical component; b) 5 Hz high-pass filtered vertical component; c) Vertical component spectrogram. High-frequency noise with frequencies higher than 10 Hz is present in the records. High-frequency energy bursts with a larger frequency band than the noise bursts are detected during the passage of the seismic waves.	60
8.1	Map of mainshocks (table 8.1) analyzed in the Lucky Strike volcano (LS - green triangle). The epicenters are marked by the yellow stars. Mainshocks have $M_w \geq 5.5$ and hypocentral depths ≤ 100	63
8.2	Data analyzed from station C1 for mainshock D in the Lucky Strike volcano. The increase in high-frequency seismic energy signals starts before the arrival of the seismic waves. a) Three-component average envelope; b) STA/LTA ratio; c) Raw vertical component; d) 5 Hz high-pass filtered vertical component. Green line marks the theoretical arrival of the P-wave with model <i>iasp91</i> ; Red lines delimit the triggering window.	66
8.3	Data analyzed from station D1 for mainshock C in the Lucky Strike volcano. A significant decrease in high-frequency activity is detected during the passage of the surface waves. a) Three-component average envelope; b) STA/LTA ratio; c) Raw vertical component; d) 5 Hz high-pass filtered vertical component. Green line marks the theoretical arrival of the P-wave with model <i>iasp91</i> ; Red lines delimit the triggering window.	67
8.4	Map of mainshocks (table 8.3 and 8.4) analyzed in Azores (AZ - red triangle). The epicenters are marked by the yellow stars. Mainshocks have $M_w \geq 5.5$ and hypocentral depths ≤ 100	67
8.5	Mainshock J recorded in Azores archipelago in station CMLA. a) Raw vertical component; b) 5 Hz high-pass filtered vertical component; c) Vertical component spectrogram. An increase in high-frequency energy bursts is detected during the passage of the surface waves.	70
8.6	Mainshock AA recorded in Azores archipelago in station CMLA. A significant decrease in high-frequency activity appears to start with the passage of the seismic. a) Three-component >5 Hz average envelope; b) Raw transverse component; c) Raw vertical component; d) Raw transverse component; e) 5 Hz high-pass filtered vertical component. Detections are marked by the red and yellow circles. The first vertical line (green) corresponds to the picked P-wave arrival and the next two red lines delimit the triggering window.	71

8.7	Data analyzed from station CMLA for mainshock A in Azores archipelago. A clear increase in activity is observed after the passage of the seismic waves. The calculated β is due to the detection of what appear to be the seismic waves higher frequencies, this could not be filtered. a) Three-component average envelope; b) STA/LTA ratio; c) Raw transverse component; d) Raw vertical component; e) 5 Hz high-pass filtered vertical component. Green line marks the theoretical arrival of the P-wave with model <i>iasp91</i> ; Red lines delimit the triggering window.	72
8.8	Mainshock A recorded in Azores archipelago in station CMLA. a) Raw vertical component; b) 5 Hz high-pass filtered vertical component; c) Vertical component spectrogram.	72
8.9	Signal detected after the passage of mainshock A surface waves in Azores archipelago. It has two impulsive phases.	73
8.10	A) Stem plot with the events located close to mainshock A epicenter in Azores archipelago between 1st June and 31st August, 1997, from the International Seismological Centre catalog. An increase occurs in the day of the mainshock and the days after. B) Histogram with the determined intervals between P and S phases of the 35 impulsive signals detected after mainshock A	73
8.11	Mainshock J recorded in Azores archipelago in station CMLA. During the passage of the seismic waves two groups of high-frequency energy bursts were detected. One occurs with the arrival of the Love waves and the other during the passage of the Rayleigh waves. Signals have emergent onsets and are tremor-like. a) Three-component >5 Hz average envelope; b) Raw transverse component; c) Raw vertical component; d) 5 Hz high-pass filtered vertical component. Detections are marked by the red and yellow circles. The first vertical line (green) corresponds to the picked P-wave arrival and the next two red lines delimit the triggering window.	74
8.12	Surface waves from mainshock J recorded in Azores archipelago at station CMLA. a) Transverse (top) and vertical (bottom) 0.01-1.0 band-pass filtered components; b) 3-component >5 Hz average envelope; c) 3-5 Hz band-pass filtered vertical component. Yellow lines mark the start of some of the high-frequency detected signals. These appear to start near a surface wave velocity maximum.	75
8.13	Plot of determined β -values vs calculated σ from the recorded peak ground velocities from equation 5.1. A clear relation between the two variables does not appear to exist.	75
G.1	Nonlinear least-squares Marquardt-Levenberg fitting of $r = vt$ linear function (green line) to the distance of the stations to the epicenter (r) and the determined arrival times (t) of the observed second burst (in purple) for mainshock J (A) and mainshock K (B) (section 6.1.3). The fitting parameter corresponds average propagation speed with a result of 1.508 ± 0.027 km/s for mainshock J and 1.513 ± 0.026 km/s for mainshock K	110
G.2	Nonlinear least-squares Marquardt-Levenberg fitting of $r = vt$ linear function (green line) to the distance of the stations to the epicenter (r) and the determined arrival times (t) of the observed second burst (in purple) for mainshock I . The fitting parameter corresponds average propagation speed with a result of 1.550 ± 0.030 km/s.	110

List of Tables

6.1	Events analyzed in Cape Verde, selected with the criteria including a limitation in expected dynamic stress	42
6.2	Additional events with magnitudes ≥ 7 analyzed in Cape Verde for the 2007-2008 deployment	42
6.3	Cases with $ \beta \geq 2$ for the stations of the 2002-2004 deployment and the permanent SACV station in Cape Verde	43
6.4	Cases with $ \beta \geq 2$ for the stations of the 2007-2008 deployment in Cape Verde	44
6.5	Determined β -values for the 7 days before mainshock L in the same time period of the passage of the surface waves, for all stations analyzed in this mainshock	51
6.6	Results of the fitting to the the second bursts identified with a a nonlinear least-squares Marquardt-Levenberg algorithm	52
7.1	Events analyzed in Mozambique	55
7.2	Cases with $ \beta \geq 2$ in Mozambique, using a 5 Hz high-pass filter	56
7.3	Cases with $ \beta \geq 2$ in Mozambique for mainshocks C and D , using a 3-5 Hz band-pass filter	57
8.1	Events analyzed in the Lucky Strike volcano	64
8.2	Cases with $ \beta \geq 2$ in the Lucky Strike volcano	65
8.3	18 of the 34 events analyzed in the Azores archipelago.	68
8.4	16 of the 34 events analyzed in the Azores archipelago	69
8.5	Cases with $ \beta \geq 2$ in Azores and the respective dynamic stress determined by the record peak ground velocity with equation 5.1. Only CMLA station had significant variations.	70
A.1	Determined β 's for all mainshocks for station SACV and stations from the 2002-2004 deployment.	88
A.2	Determined β 's for all mainshocks for stations from the 2007-2008 deployment.	89
B.1	Determined β 's for all mainshocks for the 5 Hz high-pass filtered data in Mozambique.	92
B.2	Determined β 's for all mainshocks for the 3-5 Hz band-pass filtered data in Mozambique.	93
C.1	Determined β 's for all mainshocks for all the OBS deployments.	96
D.1	Determined β 's for all mainshocks in Azores.	98
F.1	Coordinates of the stations in Cape Verde.	106
F.2	Coordinates of the stations in Mozambique.	107
F.3	Coordinates of the OBS stations deployed in Lucky Strike volcano.	108

F.4 Coordinates of the stations deployed in Azores. 108

Chapter 1

Introduction

Earthquake-earthquake interactions are still important questions of study in earthquake seismology. One of the most obvious examples of this interactions are the aftershock sequence that can occur in the aftermath of a mainshock near its source. Since observations of the seismicity rate increase in Western United States at distances up to more than 1250 km after the Landers (7.3 Mw) earthquake in California, 1992, widespread evidences for a new mode of interaction at remote distances have been recorded. This mode called Dynamic Triggering is now considered a robustly observed phenomenon. It is also widely recognize that volcanic structures can be affected by the passage of remote large earthquakes seismic waves.

The understanding of the dynamic earthquake triggering could help improve the understanding of earthquake mechanics and therefore better assess seismic hazard by being a possible tool to study the processes that trigger slip on a fault, earthquake nucleation and to measure the stresses needed for a fault to fail. For this a better understanding of the triggering mechanisms and the conditions for it to occur is necessary. More observations of the phenomenon could help address this questions.

This study is based in previous studies, *Peng et al.* [2014] and *Aiken and Peng* [2014], and its objective is to search for evidences of dynamic triggering in four regions not thoroughly searched before for this phenomenon: Cape Verde, Mozambique and in the Mid-Atlantic Ridge in the Lucky Strike volcano and the Azores archipelago. These are volcanic and rifting (extensive regime) settings where the majority of remote dynamic triggering observations have been made.

A detailed introduction to the phenomenon of dynamic triggering is made in chapter 2 where the fundamentals of seismic waves propagation and dynamic stress are presented as well as the previous observations of dynamic triggering, the proposed mechanisms for the phenomenon and the mathematical tools used to link observations of increased seismicity to the passage of seismic waves. In chapter 3 the main geophysical and geological features of the studied regions are briefly outlined and a summary of reported seismic events in the regions is made. Data used in the study is presented in chapter 4. Chapter 5 describes the methods and tools used to assess seismicity changes during the passage of remote earthquakes surface waves. In each of chapters 6, 7 and 8 the results from the study are reported and discussed for each of the study regions. Chapter 9 presents the main conclusions of this work and propose further work that can improve the complete understanding of the results.

Chapter 2

Dynamic Triggering

The Earth's crust is brittle and many faults occur along its extent. These faults slowly accumulate the long wave length stresses due to the motions of the tectonic plates for decades, centuries or longer, remaining below their frictional strength. The accumulated stress is mainly released by brittle failure when the local failure threshold is exceeded and two sides of a fault move in relation to each other. This movement can be a sudden slip generating an earthquake or a continuous slow slip that generates tremor-like seismic events that have durations between days to years. Faults are also affected by short to mid-term short-wavelength stresses that provoke fluctuations in the stress field possibly exceeding the failure threshold and triggering a seismic event. *Hill and Prejean* [2007] list the most likely significant sources of these short to mid-term short-wavelength stresses as: shallow earthquakes, magmatic intrusions, anthropogenic activities, solid earth tides and ocean loading and seasonal meteorological factors.

It is commonly assumed that the relationship between changes in the stress field and the occurrence of an earthquake on a fault can be expressed by a change in the Coulomb failure function (CFF), equations 2.1 to 2.3 [*Hill and Prejean, 2007*]. τ and σ_n represent, respectively, the shear and the normal stress components acting on a fault and μ_s and C are the static coefficient of friction and the cohesive strength, respectively. CFF is by convention ≤ 0 and according to Byerlee's law for frictional failure $CFF = 0$ corresponds to Coulomb failure. A $\Delta CFF > 0$ means the stress state is closer to failure.

$$CFF = |\tau| - \mu_s \sigma_n - C \quad (2.1)$$

$$CFF = CFF_i + \Delta CFF \quad (2.2)$$

$$\Delta CFF = \Delta\tau - \mu_s \Delta\sigma_n \quad (2.3)$$

Triggering is the term used to describe the process by which stress changes resulting from an earthquake induce or retard seismic activity. It can be caused by three stress transfer modes: static, quasi-static or dynamic.

Static and quasi-static triggering occur due to the permanent stress changes produced by the main-shock that alter the stress field in the vicinity of the source (near field or aftershock zone), within one or two fault lengths, decaying with distance approximately as Δ^{-3} and Δ^{-2} , respectively (Δ is the distance from the epicenter). In zones of stress shadow, zones where the stress field is relieved by the near earthquake, is also thought to occur an inhibition of earthquake activity.

Dynamic triggering is the triggering of seismicity, microearthquakes or tremor, by the dynamic

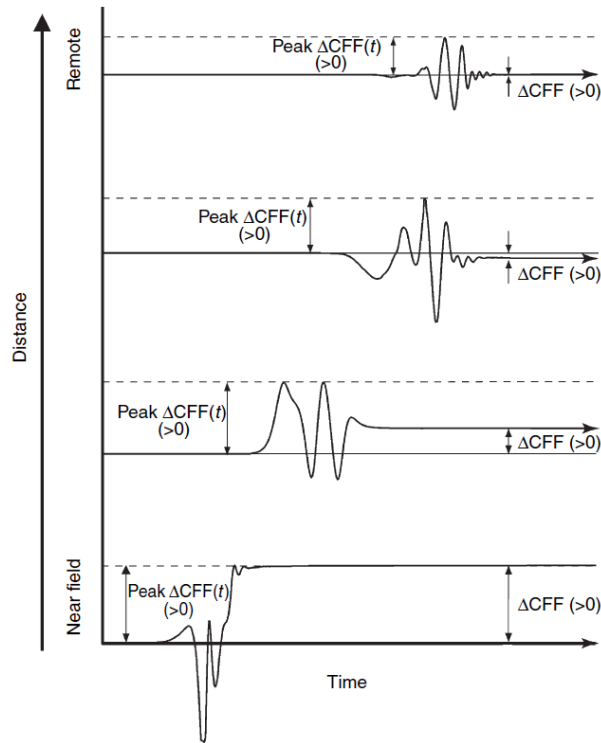


Figure 2.1: Diagram from *Kilb et al.* [2000] illustrating differences between static and dynamic stresses with distance in terms of idealized time histories for peak changes in dynamic ($CFF(t)$) and static (CFF) Coulomb stress. $CFF(t)$ is the time dependent version of CFF (eqn 2.3). The double arrows show peak values for $CFF(t)$ and CFF . [Adapted from *Hill and Prejean*, 2007].

stresses that propagate as seismic waves and temporarily alter the stress field. These stresses can act in the far-field as they decay slower than static stresses ($\sim \Delta^{-2}$ for the body waves and $\sim \Delta^{-3/2}$ for the surface waves). Figure 2.1 illustrates the changes in stress with distance to epicenter representing the changes of dynamic ($\Delta CFF(t)$) and static (ΔCFF) Coulomb stress.

2.1 Seismic waves and their propagation through Earth

To comprehend the phenomena of dynamic triggering it is necessary to understand the basics of seismic waves and how they propagate through the Earth.

When considering the three-dimensional homogeneous vector equation of motion for a uniform, isotropic, linear elastic medium (Equation 2.4, *Shearer* [2009]) two solutions are possible: the compressional, P, waves and the shear, S, waves, called body waves. In equation 2.4 u is the displacement vector and λ and μ are the Lamé parameters.

$$\rho \ddot{u} = (\lambda + 2\mu) \nabla \nabla \cdot u - \mu \nabla \times \nabla \times u \quad (2.4)$$

P waves travel faster than S waves and their particle motion is perpendicular to the wavefront in the direction of wave propagation. Therefore the P wave produces motion only in the vertical and radial directions. The S waves have a particle motion perpendicular to the direction of wave propagation and cannot propagate in mediums where rigidity disappears, as fluids.

As P and S waves travel through the different layers of the Earth (Mantle, inner Core and outer Core),

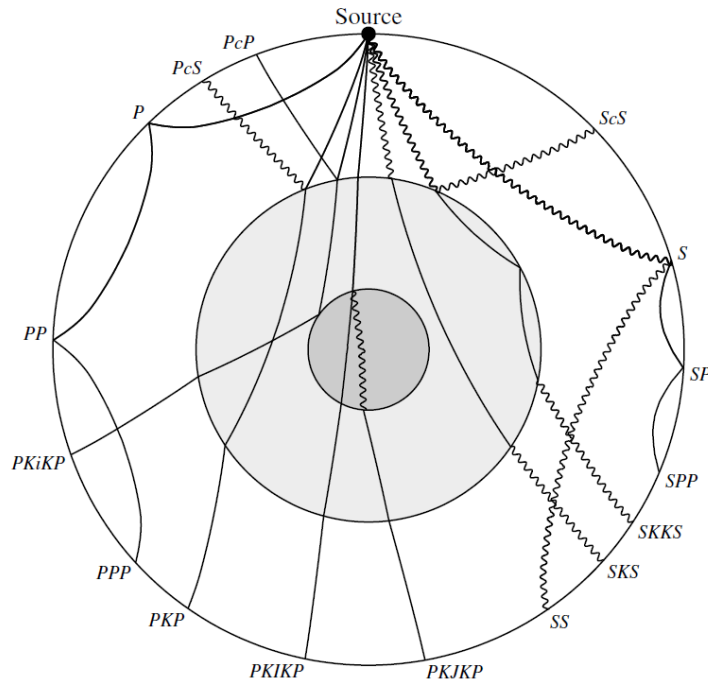


Figure 2.2: Global seismic ray paths and phase names, computed for the PREM velocity model. P waves are shown as solid lines, S waves as wiggly lines. The different shades indicate the inner core, the outer core, and the mantle. [From *Shearer*, 2009]

they interact with the discontinuities giving rise to different seismic phases, due to the change of seismic velocities and conversions between compressional and shear waves. These seismic phases have different travel times and amplitudes than the direct waves and some can be identified in seismograms. Figure 2.2 shows an example of the ray paths of these seismic phases.

When body waves reach the free surface other solutions are possible, the surface waves. These can be of two types: Rayleigh waves and Love waves. These propagate parallel to the Earth's surface. Surface waves travel slower and, as stated above, have a slower decay than body waves. Their velocity depends strongly on the wave frequency and at teleseismic distances they generally are the strongest arrivals recorded. Love waves are formed through constructive interferences of multiples of the S wave horizontal motion component in a surface layer with increasing velocity with depth and are transversely polarized. The Rayleigh waves are formed by the interaction of the P wave and S wave vertical motion component, are radially polarized and can exist at any free surface. Rayleigh waves involve shearing and compressional and dilational particle motion and Love waves involve only shearing.

Figure 2.3 shows an example of the identified P, S, Love and Rayleigh waves in a three-component seismogram with the radial, transverse and vertical components.

At solid-liquid interfaces the seismic waves can be converted to acoustic waves. In the ocean these acoustic waves can propagate in the SOFAR (Sound Fixing and Ranging channel) channel, a water layer where sound velocity is minimum and acts like a waveguide. The acoustic wave is converted to seismic waves at the shore or at islands and can then be recorded by seismometers. These waves are called Tertiary (T) waves as they travel slower than the P and S waves, at the speed of sound ~ 1500 m/s. T waves have emergent onsets and are also identified in hydrophones at the ocean. Since T waves have a decay $\sim \Delta 10^{-1}$ they can be used to detect small earthquakes in marine environments. The physical mechanism that leads the waves into propagating in the SOFAR channel and where the acoustic-seismic

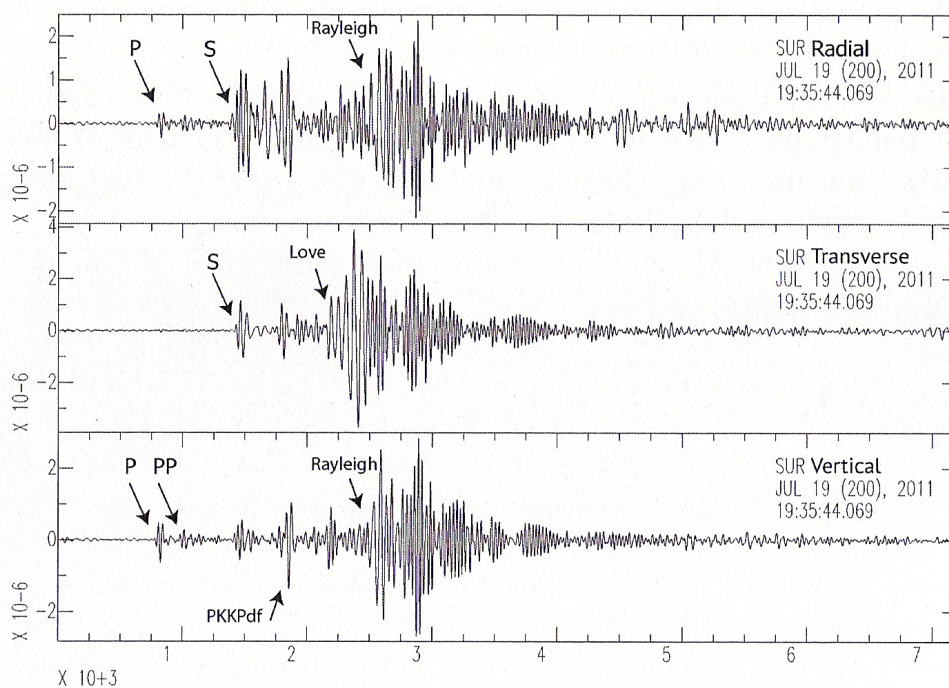


Figure 2.3: Three-component seismograms of the Mw6.0 Kyrgyzstan earthquake on the 19th of July 2011 recorded at station SUR in South Africa. The data have been rotated to the great circle path and Butterworth band-pass filtered between 0.0125-0.035 Hz. Seismograms are identified with P- and S-phases, as well as the surface waves (Love and Rayleigh). [From *Domingues*, 2016]

conversion occurs is still not understood [*Okal*, 2008; *Dziak et al.*, 2004].

2.2 Triggering by dynamic stress changes

Remote triggering after major earthquakes was first reported by *Hill et al.* [1993] that observed an increase in seismicity across the western United States after the magnitude 7.3 Landers earthquake of 28 June 1992. Activity was observed over 1250 km from the mainshock and most of it started during the passage of the large amplitude Love and Rayleigh waves trains, with some delayed increase in seismicity also observed in some areas. The distance of this triggered seismicity could not be explain by static or quasi-static stress that decay quickly with distance neither by viscous deformation that acts in the scale of years. The coincidence with the passage of the surface waves led to the hypothesis that the triggered activity was associated with the dynamic stresses imposed during the passage of the seismic waves. Dynamic Triggering is now a well documented phenomenon. *Brodsky and van der Elst* [2014] review reports observations in more than 30 major earthquakes. However, the mechanisms of dynamic triggering are still unknown. The observation of cases of delayed activity increase and of prolonged activity increase also pose a challenge to understanding the mechanisms of dynamic triggering [*van der Elst and Brodsky*, 2010].

Most of the observed onsets of the remote increased seismicity occur during the passage of the surface waves train (figure 2.4), called instantaneous dynamic triggering, with the Rayleigh waves being the most effective waves at triggering in most cases. Remote triggering coinciding with the arrival of the S wave was also observed in one occasion by *Prejean et al.* [2004]. Triggered seismicity can continue after the passage of the seismic waves and some cases of increase seismicity beginning hours or days after the passage of the waves have also been observed, this is called delayed dynamic triggering [*Brodsky and*

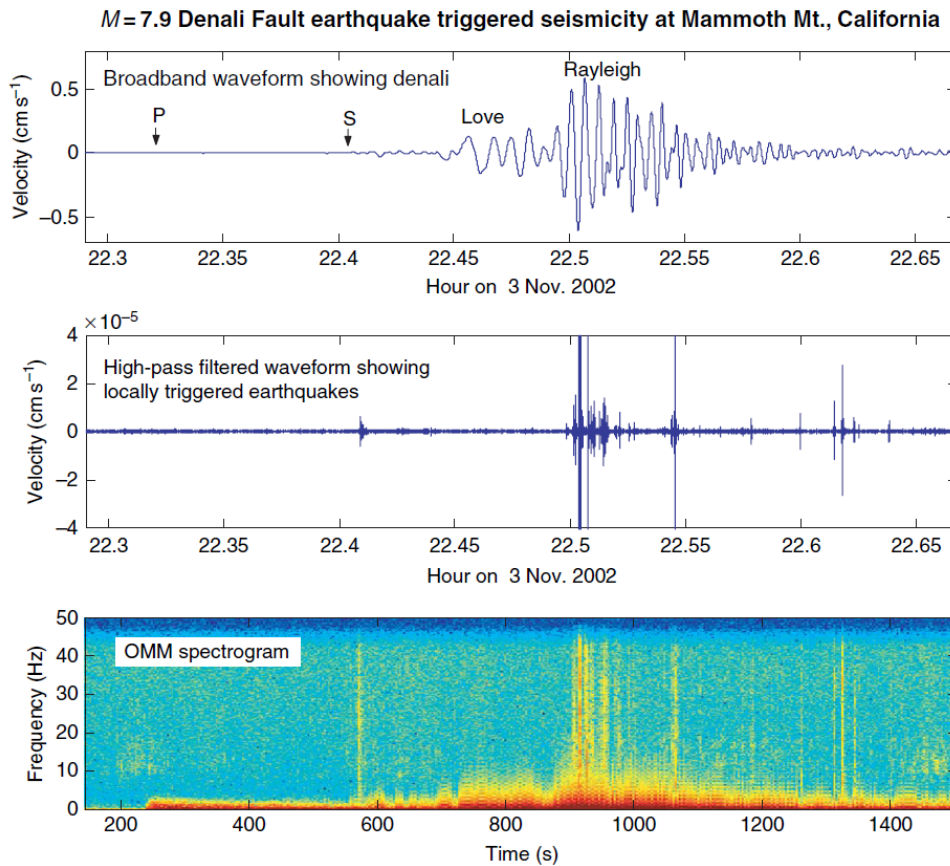


Figure 2.4: Examples of triggered seismicity detected within the surface wave coda from the Denali Fault earthquake at Mammoth Mountain. The top trace is a broadband seismogram, and the middle trace is a high-pass filtered version of the broadband record revealing the locally triggered activity as a spasmodic burst consisting of rapid-fire earthquakes. The bottom panel is a spectrogram of the broadband seismogram from station OMM located 4km southeast of Mammoth Mountain. Note the utility of the spectrogram display in revealing local earthquakes within the low-frequency coda as narrow vertical bands rich in high-frequency energy. Modified from *Prejean et al.* [2004]. [Adapted from *Hill and Prejean, 2007*]

van der Elst, 2014]. Figure 2.4 has an example of triggered seismicity detected during the passage of the Rayleigh waves, in the surface wave coda and after the surface wave train from the Denali earthquake. Triggering in the near field, aftershock zone, where static and dynamic stresses have similar amplitudes, is ambiguous and different authors attribute it to static, postseismic or dynamic agents. Some attribute the observed aftershocks in shadow zones to dynamic triggering. Figure 2.5 has an example where earthquakes occurred in zones of stress shadow. *Hill and Prejean* [2007] and *van der Elst and Brodsky* [2010] found that a portion of aftershocks in the near field can be related to dynamic stresses but there must be additional triggering components.

Dynamic triggering of seismicity has been observed in various tectonic settings. The majority of observations were made at extensional regimes and geothermal and volcanic systems but observations have also been made in subduction zones, convergent regimes and at transform faults [e.g. *Gomberg et al., 2008*]. *Velasco et al.* [2008] in a global search for dynamic triggered seismicity found that its occurrence is independent of the mainshock mechanism and its found in all tectonic regimes. *Velasco et al.* [2008] using open data from IRIS found cases of increased seismicity in Azores and no case was reported in the SACV station in Cape Verde. In East Africa positive clear cases of dynamic triggering were reported in

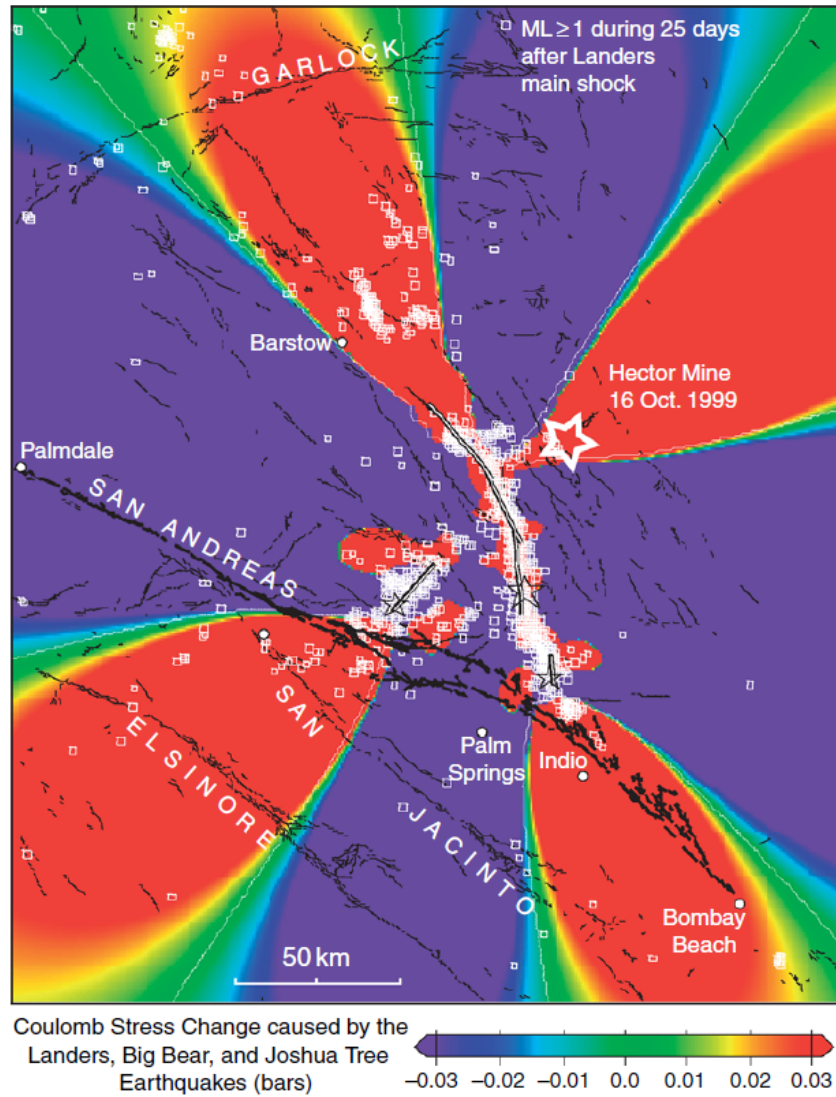


Figure 2.5: Coulomb stress changes caused by the Joshua Tree, Landers, and Big Bear earthquakes mapped at a depth of 6.25km (halfway down the fault) and (M1) aftershock distribution during the 25 days following the Landers main shock. Source parameters are those used by *King et al.* [1994]. The location (open star) and the surface rupture (solid black line) of the M 7.1, 1999, Hector Mine earthquake epicenter is shown on the map. The Coulomb stress changes are plotted with a reduced amplitude (color) scale with respect to those of the previous figures. Redrawn from *King et al.* [1994]. [Adapted from *Hill and Prejean, 2007*]

the region of the Main Ethiopian rift and in East South Africa. Earthquakes with strong directivity also affect the characteristics of the dynamically triggered seismicity by enhancing the amplitudes of dynamic stresses in specific quadrants.

Most observed cases of dynamic triggering are due to mainshocks with magnitudes > 6.5 , and bigger magnitude events seem to be more effective at triggering. *Brodsky and Prejean* [2005] studied triggered seismicity at the Long Valley Caldera and found that longer-period seismic waves are more effective at triggering in this region. As to the dynamic stresses necessary for triggering there does not seem to exist a global threshold [*Aiken and Peng*, 2014] and cases with dynamic stresses < 1 kPa (below solid Earth tides stresses) have been reported [*Wang et al.*, 2015]. Sites with repetitive dynamic triggered seismicity have been observed, although do not always respond to similar distanced large earthquakes, this could mean each site has a specific recharge time to return to a near-critical state after the passage of dynamic stresses [*Hill and Prejean*, 2007].

Types of dynamic triggered seismicity include earthquakes (mostly microearthquakes) and tremor.

2.2.1 Microearthquakes

Triggering of microearthquakes has been observed mostly at extensional and transtensional stress regimes and at geothermal and volcanic areas. The few observed examples of remotely triggered earthquakes in transpressional regimes are in volcanic regions where earthquakes in or below the volcanic edifice show dominantly normal faulting. One reason for this observations might be that faults in extensional regimes tend to be weaker than those found in compressional regimes. Some evidences for dynamic triggering in the near-field in compressional and transpressional regimes seem to exist based on pre-instrumental descriptions in the Ohio River Valley and in Coast Ranges but *Hill and Prejean* [2007] argue that there is a lack of evidences for dynamic triggering in well-instrumented compressional or stable-intraplate settings.

The triggered microearthquakes occur within the brittle crust with depths less than 15-20 km and instantaneous triggering may or may not be in phase with the surface waves.

2.2.2 Tremor

Tremor outside volcanic regions was first observed in a subduction zone southwest of Japan [*Obara*, 2002] and was described as tectonic or nonvolcanic tremor because it was not related to magma movements. Some studies observe that triggered tectonic tremor have similar character to the tremor observed around volcanoes and argue that, although sources may be different, the generative mechanisms may be similar and so describe it only as tremor [*Peng et al.*, 2009]. Triggered tremor is characterized by a noise-like signal with no clear impulsive phase and with a duration that can go up to days. These signals have been associated with slow slip events that occur for periods of time longer than classical earthquakes, events that can also be aseismic.

Triggered tremor has been observed in subduction zones, for example in Japan and Cascadia [*Rubinstein et al.*, 2007], in transform fault environments in California [*Peng et al.*, 2009] and in arc-continent collision environments in Taiwan [*Peng and Chao*, 2008]. An example of the triggered tremor detected in Taiwan is in figure 2.6

The triggered tremor was observed in zones where ambient tremor is known to occur and seems to be triggered both by Love and Rayleigh waves, Rayleigh waves being the most effective. The events are mostly located below the brittle-ductile transition zone deeper than triggered microearthquakes [*Chao et al.*, 2013].

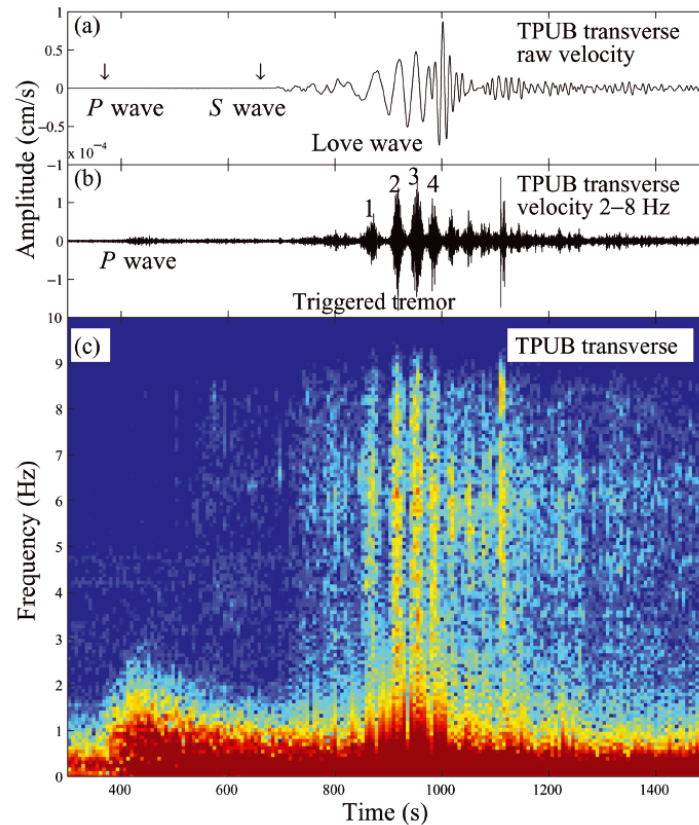


Figure 2.6: Examples of triggered tremor during the surface waves of the 2001 November 14 Mw 7.8 Kunlun earthquake. (a) Broad-band transverse component seismogram recorded at station TPUB. The time is relative to the origin time of the Kunlun earthquake. The two arrows mark the approximate arrival time of the P and S waves. (b) 2–8 Hz bandpass-filtered transverse-component seismogram showing the high-frequency P waves and the triggered tremor during the passage of the Love waves. (c) The spectrogram of the transverse-component seismogram at station TPUB. The triggered tremor signals are shown as narrow vertical bands rich in high-frequency energy as compared with the teleseismic P and surface waves. [Adapted from *Peng and Chao, 2008*]

2.3 Proposed models for the generation of dynamic triggering

Several models have been proposed for the mechanism that generate the response to the passing dynamic stresses but none seems to explain all the observed cases and it is possible that different mechanisms exist. Most models have difficulty to explain triggering by small perturbing stresses and the common occurrence of delayed triggering.

Coulomb failure

The most simple explanation is that the seismic wave apply an extra loading in a fault near failure, $CFF \sim 0$, that leads to shear failure.

This mechanism has difficulty explaining the reason why so small dynamic stresses are necessary for triggering. One explanation considers high pore pressure. According to *Brodsky and van der Elst* [2014] an increase in pore pressure would have to be extreme, $\gg 99\%$, if faults were in the beginning of their loading cycle. These extreme levels of pore pressure are possible in geothermal areas but it is also possible that triggering occurs only in areas in late loading cycle.

It agrees with tidal stresses bigger than the dynamic stresses of the seismic waves not leading to widespread regular triggering considering fault orientation. Tidal stresses have fixed orientations and waves can load different orientations. The delayed triggering is explained by considering that a first event can then trigger aftershocks that can lead to a cascade of events.

This model does not explain the observations that the Rayleigh waves seem to be more effective at triggering than Love waves and that extensional regimes seem to be more susceptible to triggering than compressional regimes [*Brodsky and van der Elst*, 2014].

Rate-state friction

This model considers experimental observations that a fault frictional strength depends on the history of stress, the slip rate (sliding velocity) and an evolving state empirical parameter that indicates if the frictional interface weakens with increasing velocity, described by the Dietrich-Ruina rate-state friction laws. If the frictional interface weakens with increasing velocity it is considered unstable and the stresses of the seismic waves can reduce friction and increase the sliding velocity even more leading to failure. This can explain the delayed triggering.

The shortcomings of this model are that laboratory experiments showed that seismic waves have short periods to be effective at triggering, unlike tidal stresses, and it cannot explain prolonged triggering by itself. This model also permits that seismic waves drive a stable or locked fault to an unstable state [*Brodsky and van der Elst*, 2014].

Viscous creep

This mechanism explains the prolonged sequence of triggered events as a result of local creep or slow slip events. Slow slip would be triggered by the seismic waves resulting in the sustained deep triggered tremor and low-frequency earthquakes observed in some areas. The mechanism that triggers the slow slip is unclear [*Brodsky and van der Elst*, 2014].

Permeability enhancement

Seismic waves can affect permeability by unclogging fractures and so enhance permeability inside a fault zone. This mechanism makes possible that small stresses result in large flows.

Earthquakes could be triggered by pore pressure redistribution or drainage. Drainage would lead to a sudden increase in permeability allowing seismic slip. A permeability enhancement would also facilitate fluid flow from high to low-pressure regions changing the strength in lock portions of the fault that can fail leading to earthquakes [*Brodsky and van der Elst, 2014*].

Granular flow

This mechanism is based in the fact that grains in fault zones do not support uniform stresses. A large distribution of stress may be supported by individual grains and most of the grains are only held together by small stresses and so have weak frictional locking. These grains could therefore be affected by small perturbations and have a major effect. This can explain the small stresses necessary for triggering. Granular mediums are also more easily weakened by dilatational strains making possible that Rayleigh waves are more effective at triggering [*Brodsky and van der Elst, 2014*].

Subcritical crack growth

Cracks in fault zones can grow due to chemical reactions enhanced by hot fluids. The stress transferred due to the passing seismic waves can assist the growth of the cracks to a critical length at which there is a release of elastic energy. It is considered that this mechanism needs more study and laboratory data to be fully assessed [*Brodsky and van der Elst, 2014*].

2.4 Interaction between earthquakes and volcanoes

It has been observed that distant earthquakes perturb volcanic systems and *Linde and Sacks [1998]* concluded that in one or two days after large earthquakes more eruptions occurred in a radius of 750 km to the epicenter. *Manga and Brodsky [2006]* however concluded that the stresses related to earthquakes are smaller than those needed to start an eruption since large earthquakes like Sumatra 2004 and Alaska 1964 were followed by an absence of reported eruptions and observations show that only a small fraction of eruptions are triggered immediately by large earthquakes. Nonetheless, as stated before, cases of triggered earthquakes have been observed in volcanic regions and these are thought to be a secondary effect of the deformation of the magma bodies triggered by the earthquakes that can explain delayed triggering in volcanic regions.

Various mechanisms for the interaction of the seismic waves with magmatic fluids have been proposed.

Bubble excitation

Bubble excitation is considered an obsolete model. This model was based in changes in bubble pressurization in a two-phase fluid. This could be done by rectified diffusion where gas in the fluid is pumped into bubbles during the dilatational phase of the passing seismic waves, increasing pressure in bubbles that consequently increases pore pressure in the interstitial fluid and triggers earthquakes. Another hypothesis is the advective overpressure model that considers that bubbles in the walls of a magma body

can be loosened by the strains of the seismic waves and start to rise in the magma so increasing its pressure and deforming the chamber triggering earthquakes [Hill and Prejean, 2007].

This mechanism was deemed ineffective as bubbles seem to resorb before the pressurization [Ichihara and Brodsky, 2006].

Magmatic intrusions

This model proposes that the seismic waves can trigger magmatic intrusions that fracture the shallow crust triggering earthquakes, as a secondary response, by changing the static stress field or increasing pore pressure [Hill and Prejean, 2007].

Relaxing magma body

Partially crystallized magma bodies can accumulate deviatoric stresses that can be released by the dynamic stresses of the seismic waves. The deviatoric stresses change the stress field that can lead to triggered seismicity [Hill and Prejean, 2007]. This model would require a rather long relaxation period and other mechanisms would have to be involved in sites with observed repetitive triggered seismicity.

Sinking crystal plumes

This model considers the effects that the seismic waves can have in crystals in ceilings and walls of magma chambers. These crystals can fall and sink in the magma stimulating convection. This could lead to the formation and growth of bubbles increasing the pressure and deforming the crust. This mechanism can lead to triggered earthquakes and eruptions [Hill and Prejean, 2007].

2.5 Triggering statistics

Various statistical tests are used in order to investigate the causal link between the observations of increase in local seismicity and the passing of seismic waves of remote large earthquakes. The most used test for the statistical significance of dynamic triggering is the β -statistic of Matthews and Reasenberg [1988] [Hill and Prejean, 2007]. This statistic calculates the significance of the changes in the seismicity comparing the number of events occurring in the analyzed period of time with the expected number of events in that period assuming a constant seismicity rate, normalized by the standard deviation of the expected number of events [Aron and Hardebeck, 2009]. The expected number of events is assumed by determining a background seismicity of the area of study. The β -statistic is calculated with equations 2.5 and 2.6, where T_a and T_b are the time period analyzed and the time period considered for the background seismicity, respectively, and N_a and N_b are the number of events observed during T_a and T_b , respectively. In studies of instant dynamic triggering T_a , also called the triggering window, usually corresponds to the time between the arrival of seismic energy traveling at 5 and 2 km/s when most of the surface wave energy passes.

$$\beta = \frac{N_a - N(T_a/T)}{\sqrt{N(T_a/T)(1 - (T_a/T))}} \quad (2.5)$$

$$T = T_a + T_b, \quad N = N_a + N_b \quad (2.6)$$

A difference in seismicity rate between the two time periods is significant at 90% confidence for $|\beta| \geq 1.64$, at 95% for $|\beta| \geq 1.96$ and at 99% for $|\beta| \geq 2.57$. In general, β -statistic absolute values ≥ 2 are considered a significant rate change (with $\sim 95\%$ confidence).

Chapter 3

Geophysical and Geological Setting

Data from four different regions were analyzed in this study: Cape Verde archipelago, Mozambique and Azores archipelago and Lucky Strike volcano in the Mid-Atlantic Ocean Ridge. These regions allowed the search for evidences of dynamic instant triggering in volcanic regions, Cape Verde, Azores and the Lucky Strike volcano, and in rifting environments in different stages of development, Mozambique, Azores and Lucky Strike.

3.1 Cape Verde

Cape Verde is an Archipelago composed by 10 major volcanic islands and several islets located in the crest of the Cape Verde Rise, the largest swell in the Atlantic Ocean, in the North Atlantic at about 500 km off the West African Coast (figure 3.1).

3.1.1 Tectonics and geology of the archipelago

The Cape Verde archipelago is set in the Cape Verde Rise. The Cape Verde Rise is a 2,2 km elevation above the expected depth of about 6000 m (depth of early Cretaceous aged seafloor), with about 1200 km in diameter [Pim *et al.*, 2008]. The identification of magnetic anomalies in the vicinity of the islands suggests they are set on a 150-122 Ma-old (Late Jurassic - Early Cretaceous) oceanic crust. The crust has a thickness of about 7 km [Pim *et al.*, 2008] in the ocean and about 22 km under the islands [Lodge and Helffrich, 2006]. The swell and magmatism in the region are generally attributed to a hotspot that is sustained by a plume whose root location is still debated, in the deep mantle [Pim *et al.*, 2008] or in the upper mantle [Helffrich *et al.*, 2010]. Some studies also found evidences that other processes such as buoyancy forces due to magmatic underplating [Watts *et al.*, 1997] or hotspot related melting processes in the sub-lithospheric mantle [Lodge and Helffrich, 2006] must also contribute to the swell.

The islands are distributed in a horseshoe shape with two chains that open to the west. Although they do not exhibit a clear age progression of the eruptive activity as in other volcano archipelagos, in general, the oldest islands are located to the east and the youngest at the northwest and southwest with separated islands having erupted simultaneously on the geological timescale (for example Maio and Santo Antão). One of the explanations for the lack of a clear age progression is that the African Plate is practically stationary in relation to the plume since the velocity of rotation of the African Plate at Cape Verde is very small (about 20 mm/year) [as cited in Faria, 2006].

Igneous activity due to the hotspot began about 19 Ma ago and the volcanic activity seems to have started in Sal about 16 Ma ago [Holm *et al.*, 2006]. Boavista is also thought to be one of the islands where

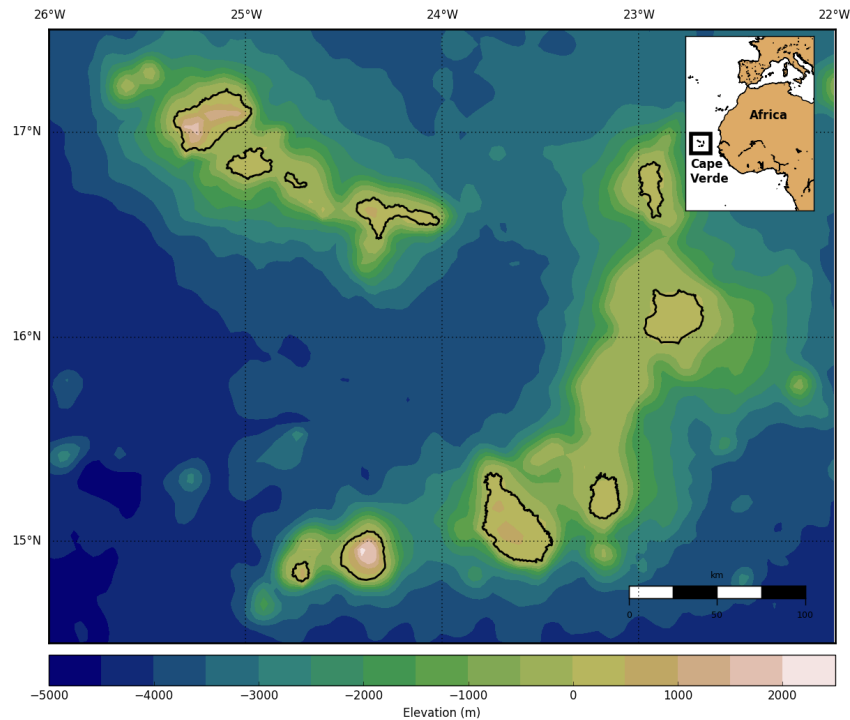


Figure 3.1: Cape Verde archipelago major islands with elevation. Location of the archipelago in the North Atlantic off the coast of Africa

volcanic activity started. In Sal, volcanic activity was present until 1 Ma ago. Volcanic activity occurred between 12 and 7 Ma ago in the island of Maio, 7.5 and 0.1 Ma ago in Santo Antão, 7 and 0.3 Ma in São Vicente, 6 and 0.3 Ma in Santiago and 6.5 Ma and 50 ka in São Nicolau. Brava is the youngest island with intrusions in its base being dated about 2.1 Ma ago and its most young rocks dated of about 1000 years ago and the island is still in formation [as cited in *Faria, 2006*].

Geological evidences show that volcanic activity seems to be intermittent, with long periods of quiescence separating eruptive phases. Since the discovery of the archipelago by the Portuguese volcanism has only been reported in Fogo island, with the most recent eruption in 2014. Geological investigations in the islands of Brava and Santo Antão revealed recent volcanic events (Holocene) that point to the presence of active volcanic systems.

The islands can be divided in two main groups:

- Santo Antão, São Nicolau, Santiago and Fogo, that present a youthful strong relief.
- São Vicente, Santa Luzia, Sal, Boavista and Maio, that have topography leveled by both subaerial and marine erosion.

Brava is not part of any of these groups because it presents a strong relief but has also been deeply eroded, so that its southern half corresponds to exhumed magma chambers characterized by a plutonic complex of pyroxenites, syenites and hyaloclastites that form an uplifted submarine sequence [*Vales et al., 2014*]. Erosion is stronger in Sal, Boavista and Maio since these islands were submersed.

Multibeam bathymetry and backscatter data collected by the Meteor and the RSS Charles Darwin cruise of the sea-floor around the islands of Santo Antão, São Vicente, Fogo, and Brava revealed the presence of youthful cone fields between the islands of Brava and Fogo, between the islands of Fogo and

Santiago (figure 3.2) and south of São Nicolau. Southwest of Brava was located the growing Cadamosto seamount [Masson *et al.*, 2014].

The most common volcanic products found in the archipelago are lava flows, cinders e phonolitic tuff [Faria, 2006].

The southern group of islands has a prevalence of tectonic or tectono-volcanic structures [Vales *et al.*, 2014]. These structures trend NW-SE, NE-SW, N-S and E-W. In the island of Fogo NW-SE scarps interpreted as a graben were found in northwest flank. The Cachaço and Vigia fault are NW-SE trending normal faults in Brava. Brava has also a major NE-SW fault zone that separates the northwest of the island and strike slip faults were also identified. E-W strike-slip faults with dominant left-lateral displacement were observed in the northwest coast of Brava.

3.1.2 Seismicity of Cape Verde

Due to few data available from permanent seismic stations in the archipelago, international catalogs rely mostly in the global network. Seismicity in the archipelago is scarce and was reported mainly in Fogo and Brava islands [Vales *et al.*, 2014]. Seismic activity was recorded in the periods of 1941-1954 33 events and 1955-1971 88 events, felt in Fogo, Brava, Santo Antão and São Vicente. Some of these correspond to seismic swarms. From December 1980 to May 1981, 135 earthquakes with magnitudes up to 2.9 occurred around the islands of Brava and Fogo. 58 events were also recorded during the 1995 Fogo eruption.

Two earthquakes with magnitude $m_b > 4$ occurred southwest of Brava in the Cadamosto seamount area, in 18 September 1998 and 17 August 2004 [Grevemeyer *et al.*, 2010].

Vales *et al.* [2014] analyzed the data from the CV-Plume project temporary deployment between 2007 and 2008 and detected 358 events (figure 3.3). Seismicity was mainly concentrated in the westernmost areas of the archipelago and no significant activity was detected in island of Fogo or in easternmost islands. Events between the Cadamosto seamount and Brava suggest an active linear tectono-volcanic NE-SW and NW-SE trending structure with normal faulting. In the northwest, seismicity is more dispersed with the most important clusters located south-southwest of Santo Antão and São Vicente associated with a submarine cone field.

Faria and Fonseca [2014] analyzed the data from a 15 stations network in Santo Antão, São Vicente, Sal, Fogo and Brava from July 2010. No seismicity was recorded in Sal and São Vicente.

In Fogo various volcanic seismic events were recorded: cigar-shaped (between 5 to 15 Hz), hybrid (between 0 and 5 Hz, duration of about 1 minute), long-period, volcano-tectonic and spasmodic tremors (very emergent and last between minutes to hours, spectra similar to cigar-shaped and hybrid events). An average of 8 events per day occurred and events increased during the rainy season. 57 volcano-tectonic events were also detected with local magnitudes between 0.1 and 3.5. Locatable events seemed to occur below the crater of the 1995 eruption. In Brava most events were volcano-tectonic with magnitudes between 0.7 and 3.2. An average of 1 event per day was observed but varies a lot due to frequent seismic swarms. Most epicenters occur offshore NE in the region of the submarine volcanic cones and also SE where a recent eruption seems to have occurred. In Santo Antão events are mostly volcano-tectonic events, medium frequency events and harmonic volcanic tremor, with local magnitudes ranging from 0.1 to 4.5. An average of 3 events per day was observed but frequent seismic swarms were also present. Epicenters are diffuse and cover most of the island but are grouped in two main zones: NW that seems to be related with Nola Seamount and SW that seems to be related with the Charles Darwin volcanic field.

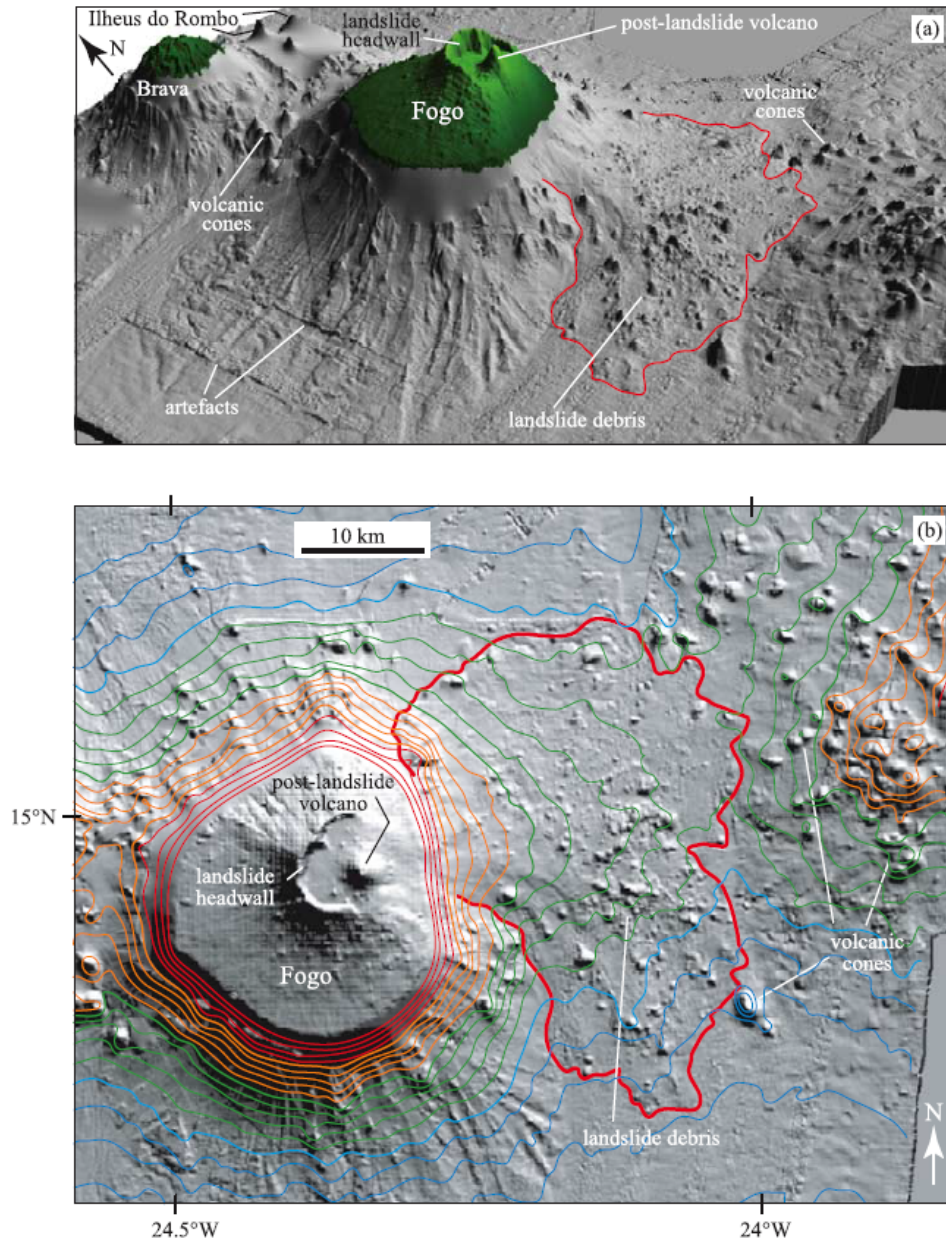


Figure 3.2: (a) Oblique 3-D image of Fogo and Brava, viewed from the southeast, based on swath bathymetry offshore and SRTM data onshore. (b) Plan (map) view of Fogo and the surrounding seafloor. Contours are at 200 m intervals with thousand meter contours in bold (orange, 1000 m; green, 2000 m; blue, 3000 m). The volcanic cones on the right of the image are on the lower slope of Santiago island. [Adapted from *Masson et al.*, 2014]

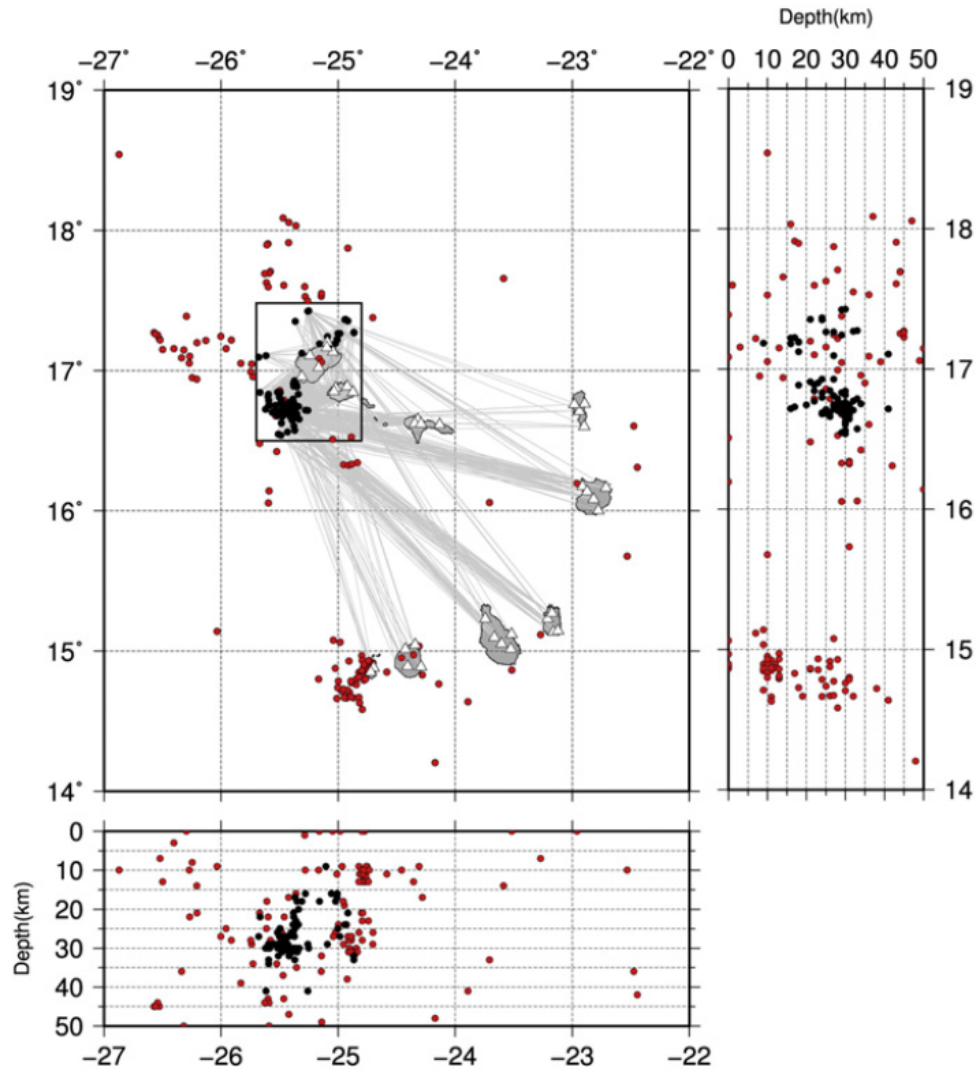


Figure 3.3: Hypocentres of all locatable events registered between Nov. 2007–Sep. 2008 in the Cape Verde archipelago (red); final area selected for derivation of the 1D model and events complying with the selection criteria (black). To the bottom and left of the epicentral map are W–E and S–N vertical cross-sections. [From *Vales et al.*, 2014]

3.2 Mozambique

Mozambique is a country located in Southern Africa (figure 3.4), in the eastern border of the African Plate (Nubia). It is bordered by Tanzania and Zambia to the North, by Zimbabwe to the West, by South Africa to the Southwest and by the Indian Ocean to the East.

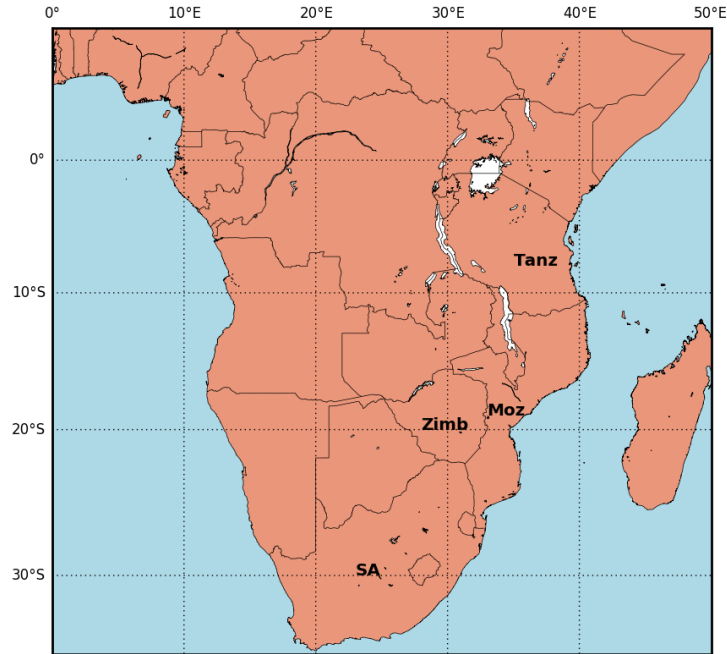


Figure 3.4: Map with the location of Mozambique (MOZ) in Southeast Africa. Tanz - Tanzania; Zimb - Zimbabwe; SA - South Africa.

3.2.1 Geology and tectonics of Mozambique

Mozambique is located at the southern end of the East African Rift [Domingues *et al.*, 2016]. The East African Rift System (EARS) is an intra-continental ridge system, characterized at the surface by a succession of several adjacent individual tectonic basins controlled by faults that form subsiding grabens or troughs that separate the Nubian Plate from the Somali Plate. The EARS can be divided into two main branches, the Eastern Branch and the Western Branch [Chorowicz, 2005] (figure 3.5). Structures in Mozambique are along the continuation of the Western Branch.

The Eastern Branch spreads from the Afar region southwards to the north of Tanzania (North Tanzanian divergence) along preexisting weak zones. This branch is in a more matured stage of the rifting process [Craig *et al.*, 2011]. The Western Branch is separated from the Eastern Branch in the the Aswa shear zone that presents a transtensional motion. The Western Branch spreads from Lake Albert (Uganda), south of the Aswa shear zone, to the Malawi rift from where its extent south is unclear. One proposal is that it extends through the Urema Rift in Central Mozambique, which is supported by the 2006 Mw7 earthquake and its aftershocks in Mozambique [Yang and Chen, 2010]. Seismic activity is present all along the Western Branch from Uganda to Mozambique.

The formation and the kinematics of the EARS are still not well understood and several models have been proposed: active rifting due to mantle convection and plume movements that deform the lithosphere by asthenospheric intrusions; passive rifting by lithospheric extension as a reaction to stresses generated in plate boundaries and an uplift of the asthenosphere as a response; a mixed model that combines pas-

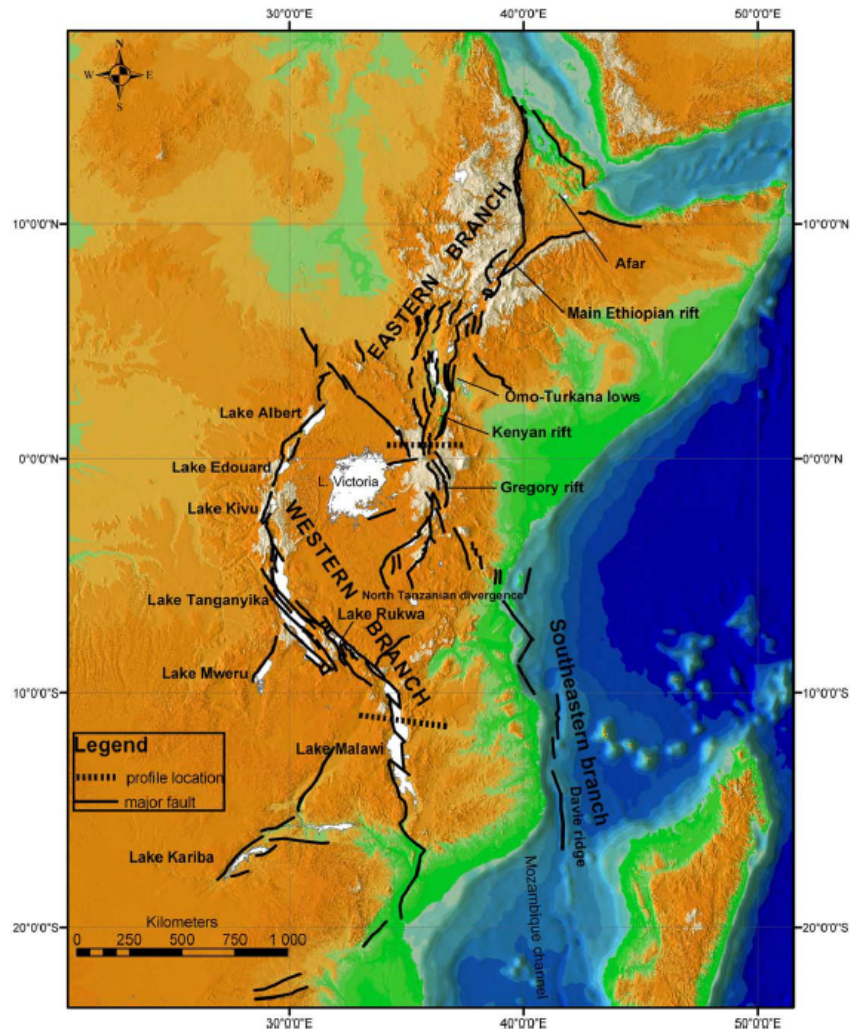


Figure 3.5: Hypsographic DEM of the East African rift system. Black lines: main faults; white surfaces: lakes; grey levels from dark (low elevations) to light (high elevations). The East African rift system is a series of several thousand kilometers long aligned successions of adjacent individual tectonic basins (rift valleys), separated from each other by relative shoals and generally bordered by uplifted shoulders. It can be regarded as an intra-continental ridge system comprising an axial rift. [Adapted from *Chorowicz, 2005*]

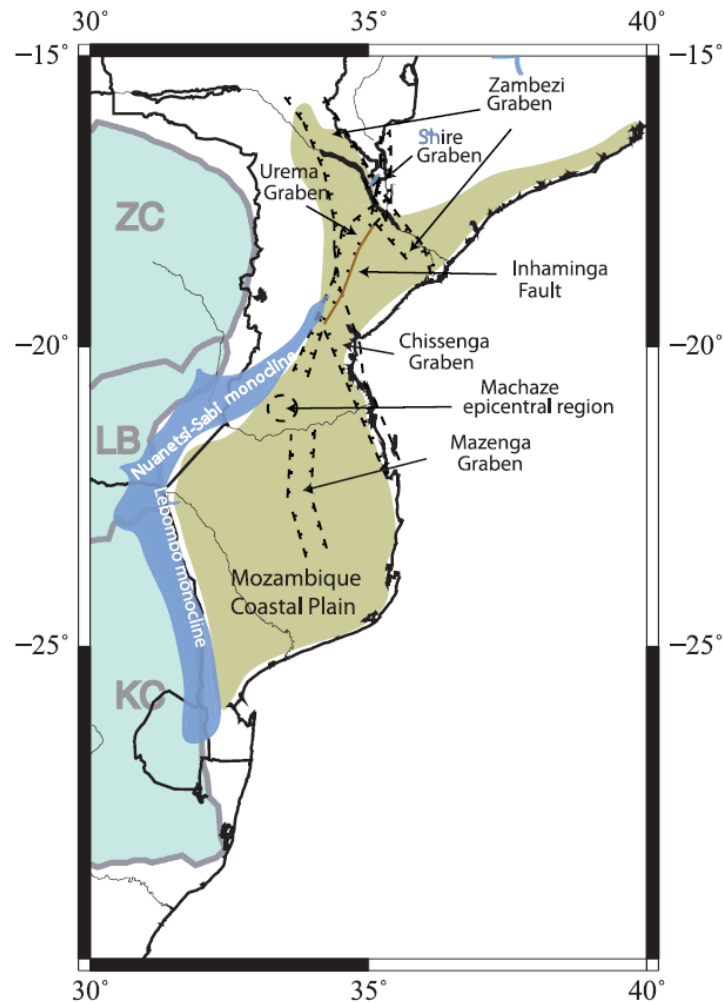


Figure 3.6: Simplified map of Mozambique with the main geological and tectonic units. ZC—Zimbabwe craton; LB—Limpopo; KC—Kaapvaal craton. [From *Domingues et al.*, 2016, and references therein]

sive and active rifting. Recent studies [e.g., *Stamps et al.*, 2008] show that the opening rate along the Western Branch increases from the north, close to Lake Albert, down to the Malawi Rift, from 1 to 4.5 mm.y^{-1} , and then decreases from the Malawi Rift southwards to 1.5 mm.y^{-1} at the latitude of the southern Mozambique coastal plain. Data is also consistent with a kinematic model that includes 3 additional plates between the Nubian and the Somalian Plate, the Victoria, Lwandle and Rovuma Plates. The proposed Rovuma Plate has its boundary with the Nubian Plate in the section of the EARS in Mozambique.

Mozambique is flanked on the West by two Archaean cratons, the Kaapvaal and the Zimbabwe Cratons (figure 3.6). The Kaapvaal Craton is a granite-greenstone terrain, that includes deformed greenstone of basic and ultrabasic volcanics, with age between 3.6 and 2.7 Ga and is one of the only two sizable areas in the world with crust this age pristinely preserved [*Zegers et al.*, 1998]. The Zimbabwe Craton has an age between 3.0 and 2.5 Ga and is formed by greenstones, gneisses, mafic and ultramafic volcanic rocks, intrusive granites, migmatites and intrusions of granitoids and porphyry [*Dirks and Jelsma*, 2002]. The two Archaean Cratons are separated by the Limpopo Belt that collided with the Kaapvaal Craton at 2.68 Ga and with the Zimbabwe Craton at 2.58 Ga forming the Limpopo Orogen [*Kusky*, 1998].

The Zimbabwe Craton is bounded in the east by the north-south trending Mozambique Belt which is part of the Pan-African Orogen and is related to the amalgamation of East and West Gondwana (600-550

Ma) [Grantham *et al.*, 2003]. The Lurio Belt, a ENE-WSW-trending structure part of the Mozambique Belt that crosses northeast Mozambique, belongs to the Mesoproterozoic Kibaran Orogeny (1.4 Ga) and was repeatedly reactivated by the Pan-African Orogeny [Engvik *et al.*, 2007]. In this region the Mozambique Belt can be identified by high-grade gneisses, granulites, quartzites, granitoides and migmatites and cover northern and western central parts of Mozambique [Domingues *et al.*, 2016; Leinweber *et al.*, 2013].

Southern and eastern central Mozambique is covered by the Mozambique Coastal Plains, a large sedimentary basin. They are limited to the north-west by the Nuanetsi-Sabi monocline and the Zimbabwe Craton and to the west by the Lebombo monocline and the Kaapvaal Craton. During the early stages of Mesozoic rifting (Gondwana breakup) eruptions formed the Karoo flood basalts, being the Lebombo and the Nuanetsi-Sabi monoclines their most prominent parts. In the Mozambique Coastal Plains the Karoo basalts are found at depths of about 3200 m and covered by Upper Cretaceous and Tertiary sediments. The type of crust of the Mozambique Coastal Plains is still not determined and the transition between continent and oceanic crust is a matter of debate [Leinweber *et al.*, 2013; Fonseca *et al.*, 2014].

During the Cenozoic deformation in Mozambique has occurred along two fault systems: the Zambezi Tectonic System, formed by two NW-SE faults in the limits of the Lower Zambezi graben, and the younger Inhaminga Tectonic System, formed by the N-S Shire graben and the NW-SE Urema graben (figure 3.6). The Shire graben connects to the Malawi rift to the North. Another active structure has been proposed in southern Mozambique, the Mazenga graben [Fonseca *et al.*, 2014].

3.2.2 Seismicity of Mozambique

Mozambique has a limited coverage by seismometer networks, having only four intermittent operating stations [Fenton and Bommer, 2006], and most analyses are limited to the Global Seismic Network so small earthquakes are not detected and present in the catalogues. Location errors can be large, making the association with the active structures not clear. Pule and Saunders [2009] reported a magnitude of completeness of 4.5.

Seismicity shows a NE-SSW trend across central Mozambique between 18° S and 21° S [Fonseca *et al.*, 2014]. Four major earthquakes have occurred in Mozambique since the 20th century: the May 20th, 1951 with magnitude 6; the July 20, 1957 with magnitude 6.2; the September 5th, 1957 with magnitude 6.0; and the February 26th, 2006 Mw7 near Machaze . The Machaze earthquake has a focal mechanism that indicates normal faulting and an estimated depth of 12 km according to Fenton and Bommer [2006] and 14.8 km according to Attanayake and Fonseca [2016].

A preliminary analysis of the MOZART data [Fonseca *et al.*, 2014] (figure 3.7) determined the epicenters of 307 earthquakes with local magnitudes ranging from 0.9 to 3.9 between April 2011 and July 2012. The preliminary locations were obtained with a velocity model of the Kaapvaal Craton and show a straight NNE-SSW linear pattern that correlates with the Urema rift valley and extends for about 300 km from the Zambezi fault to the region of the Machaze earthquake epicenter. The earthquakes had depths up to 30 km which suggests the presence of an active fault potentially of crustal scale that corresponds to the Inhaminga fault. The analysis of four earthquakes shows normal faulting in agreement with the Inhaminga fault orientation (strike N31°E).

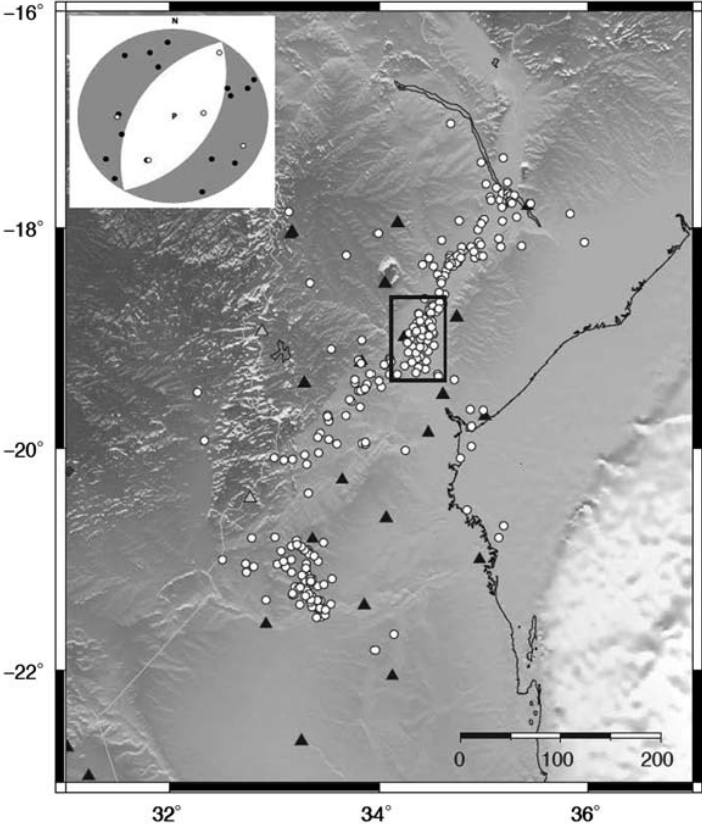


Figure 3.7: Preliminary locations of the earthquakes recorded during the first half of the MOZART deployment (April 2011 to July 2012). The map view of all the epicenters with horizontal uncertainty below 10 km (307 events). A joint focal mechanism solution is shown for four earthquakes with $M_L > 2.4$ located in the Urema graben, inside the outlined rectangle (P-wave first motions, 21 polarities, 3 violations). [Adapted from *Fonseca et al.*, 2014]

3.3 Mid-Atlantic Ocean Ridge

Two regions of the Mid-Atlantic Ocean Ridge were studied. Data from Ocean Bottom Seismometers (OBS) deployed in the Lucky Strike volcano and also data from two permanent stations in the Azores archipelago, in the islands of São Miguel and São Jorge, were analyzed.

In mid-ocean ridges there is crust formation through a combination of magmatic and tectonic processes. In slow-spreading ridges like the Mid-Atlantic Ridge magmatism seems to be discontinuous and episodic, and strong interactions between lithospheric faulting and the melt supply system can exist.

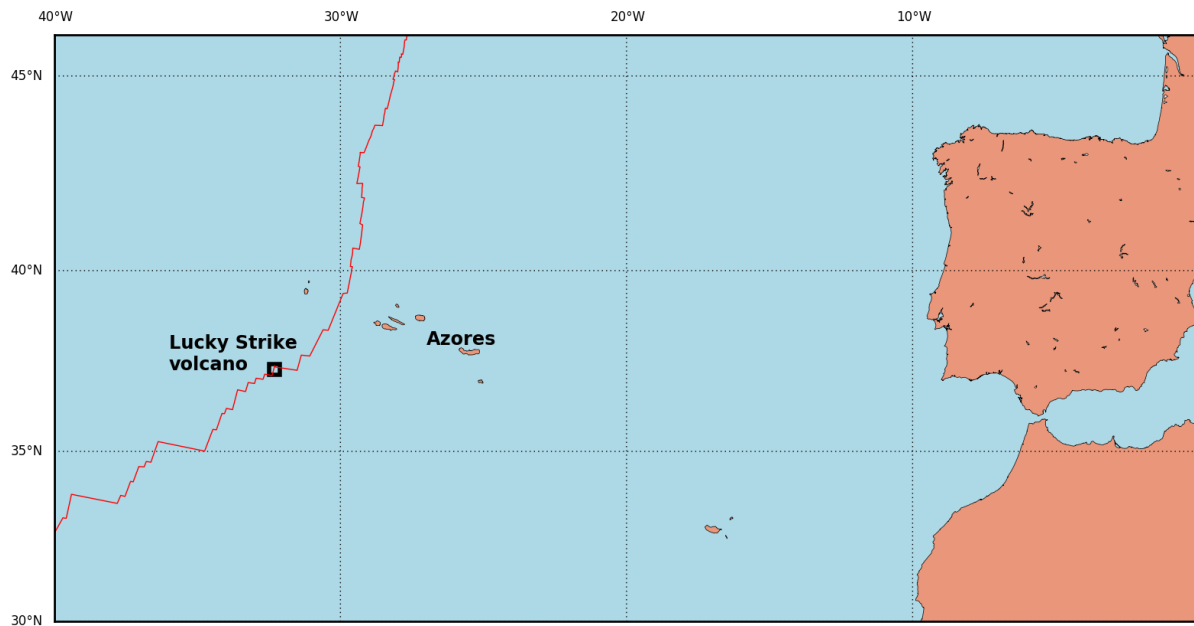


Figure 3.8: Location of the Azores archipelago and the Lucky Strike volcano (black box) in the North Atlantic. The red thin line marks the Mid-Atlantic Ocean Ridge.

3.3.1 Azores

The Azores archipelago is formed by nine volcanic islands and is located in the North Atlantic Ocean about 1400 km west of continental Europe in the Azores Plateau, an area with an abnormal thick crust defined by the 2000 m bathymetric curve and with an area of 5.8 million km². The islands spread along a NW-SE direction. In this region the North American, Eurasia and African plates join in the Azores Triple Junction. In this region, an anomalous magmatic production is observed that is attributed to a mantle plume. Seismic and volcanic activity is located mainly at the plate boundaries [Gaspar *et al.*, 2015].

The main tectonic structures (figure 3.9) are the extensional Mid-Atlantic Ridge that crosses the Azores plateau between the islands of Faial and Flores and is bounded by two transform faults with dextral strike-slip north of Azores and left-lateral strike-slip south of Azores, the inactive East Azores Fracture Zone that bounds the Azores Plateau in the south, the also inactive West Azores Fracture Zone, the North Azores Fracture Zone that intersects the Mid-Atlantic Ridge and the Terceira Rift.

The Terceira Rift developed from a transform fault into an obliquely ultraslow spreading rift [Beier *et al.*, 2008]. It was formed very recently (1 Ma ago) and has a NW-SE trend and affects the islands of Graciosa, Terceira and São Miguel.

The island of São Jorge is a volcanic ridge with WNW-ESE trend [Mendes *et al.*, 2013].

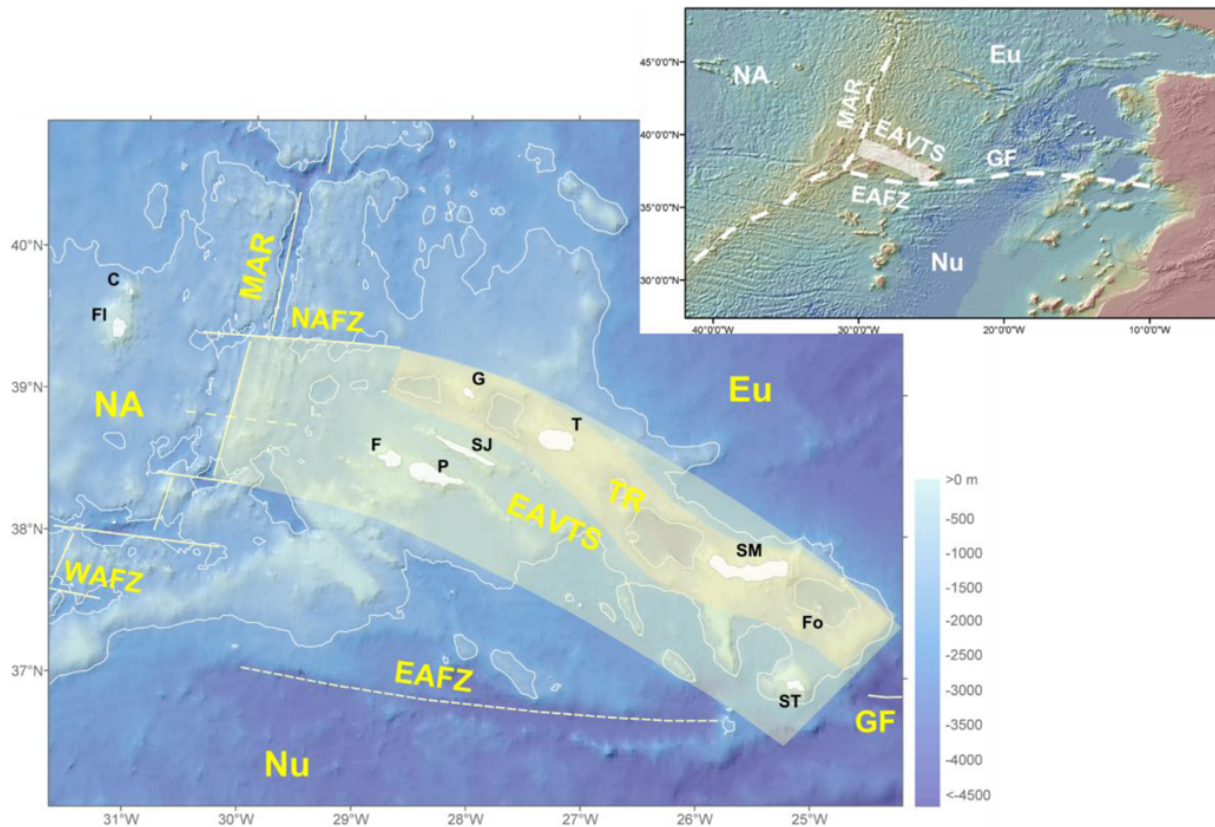


Figure 3.9: Azores region main tectonic structures. The shaded area represents the sheared western segment of the Eu–Nu plate boundary. Lithospheric plates: NA, North America; Eu, Eurasia; Nu, Nubia. Tectonic structures: MAR, Mid-Atlantic Ridge; NAFZ, North Azores Fracture Zone; WAFZ, West Azores Fracture Zone; TR, Terceira Rift; EAFZ, East Azores Fracture Zone; GF, Gloria Fault; EAVTS, East Azores Volcano-tectonic System. Islands: C, Corvo; FI, Flores; F, Faial; P, Pico; SJ, São Jorge; G, Graciosa; T, Terceira; SM, São Miguel; Fo, Formigas islets; ST, Santa Maria. Azores bathymetry adapted from *Lourenço et al.* [1997] and world topography and bathymetry from GEBCO_08 database 2010. [From *Gaspar et al.*, 2015]

In the historical period 5 eruptions occurred in the island of São Jorge, 4 in land through vents and 1 offshore in the Velas submarine volcano. In the region of São Miguel 6 eruptions occurred offshore and 5 in land, in the Furnas Volcano, the Fogo Volcano and in Picos Fissural Volcanic system [Gaspar *et al.*, 2015].

São Jorge was formed by the eruption of basaltic lava flows and in the region of Rosais correlative cinder cones were identified [Gaspar *et al.*, 2015]. São Miguel island was formed by alternating basaltic and trachytic eruptions [Beier *et al.*, 2006].

Seismicity of Azores

Since settlement in the Archipelago, 15 major earthquakes and 16 seismic crises, 10 of which related to volcanic eruptions, were registered. Two were located in the vicinity of São Jorge, the 1757 and 1964 earthquakes, and 6 in or near the island of São Miguel, the most recent are the 1932, 1935 and 1952 earthquakes located southeast of the island.

In the region of the island of São Miguel various seismic crises have also occurred: October 1988, at the São Miguel Basin, SE of São Miguel island; November 1988 to January 1989, at Hirondele basin, NW of São Miguel; 1989, at Fogo Volcano in São Miguel; 1998, at Sete Cidades Volcano, São Miguel; 1997, between the islands of São Miguel and Terceira near the Dom João de Castro Bank (figure 3.10).

The central area of São Miguel, that includes the Fogo Volcano and the Congro Fissural Volcano System, is a zone of almost permanent activity often related to magmatic and hydrothermal activity. By contrast São Jorge seems to be in an area of a seismic gap and, because the stronger earthquakes registered in historical times had epicenters in the area surrounding the island, seems to be at a stage of stress accumulation [Gaspar *et al.*, 2015].

3.3.2 Lucky Strike

Lucky Strike (figure 3.11) is a slow spreading segment about 65 km long along the Mid-Atlantic Ridge at 37°20', close to the Azores hotspot. This region of the Mid-Atlantic Ridge spreads at a rate of 22 mm/yr with a N110° direction. The segment has a 20 km wide axial valley with depths from 1550 m in the center to >4000 m at the nodal basins near the segment ends. In the center the segment shallows due to the large central Lucky Strike volcano. The segment is bound by two non-transform offsets in the north and in the south.

The rift valley is bound by two major normal faults with a vertical throw >500 m and several other smaller faults are present in the rift valley floor that mark a inner rift zone 1-4 km wide at the center of the valley. The most recent volcanic activity seems to concentrate in the inner rift zone.

The Lucky Strike volcano lies on the eastern half of the valley and spreads along 15 km of the valley axis and is 9 km wide. It rises about 400 m above the valley floor. The summit is crosscut by faults oriented along axis that define a graben and has three high faulted peaks. The peaks surround a depression that is also surrounded by high and low temperature thermal vents. In the depression were found relict sulfide deposits and debris believed to be related to a long hydrothermal history and young lavas with no alterations which suggests the volcanic activity had a recent resurgence, probably due to the reactivation of the hydrothermal fields [Crawford *et al.*, 2013].

The system seems to have two hydrothermal cells and an axial magma chamber (AMC) was identified 3.0-3.8 km beneath the volcano seafloor by a reflector in a seismic reflection/refraction study [Crawford *et al.*, 2013]. The chamber spreads for 2-3 km across-axis and 4-7 km along-axis. This chamber is

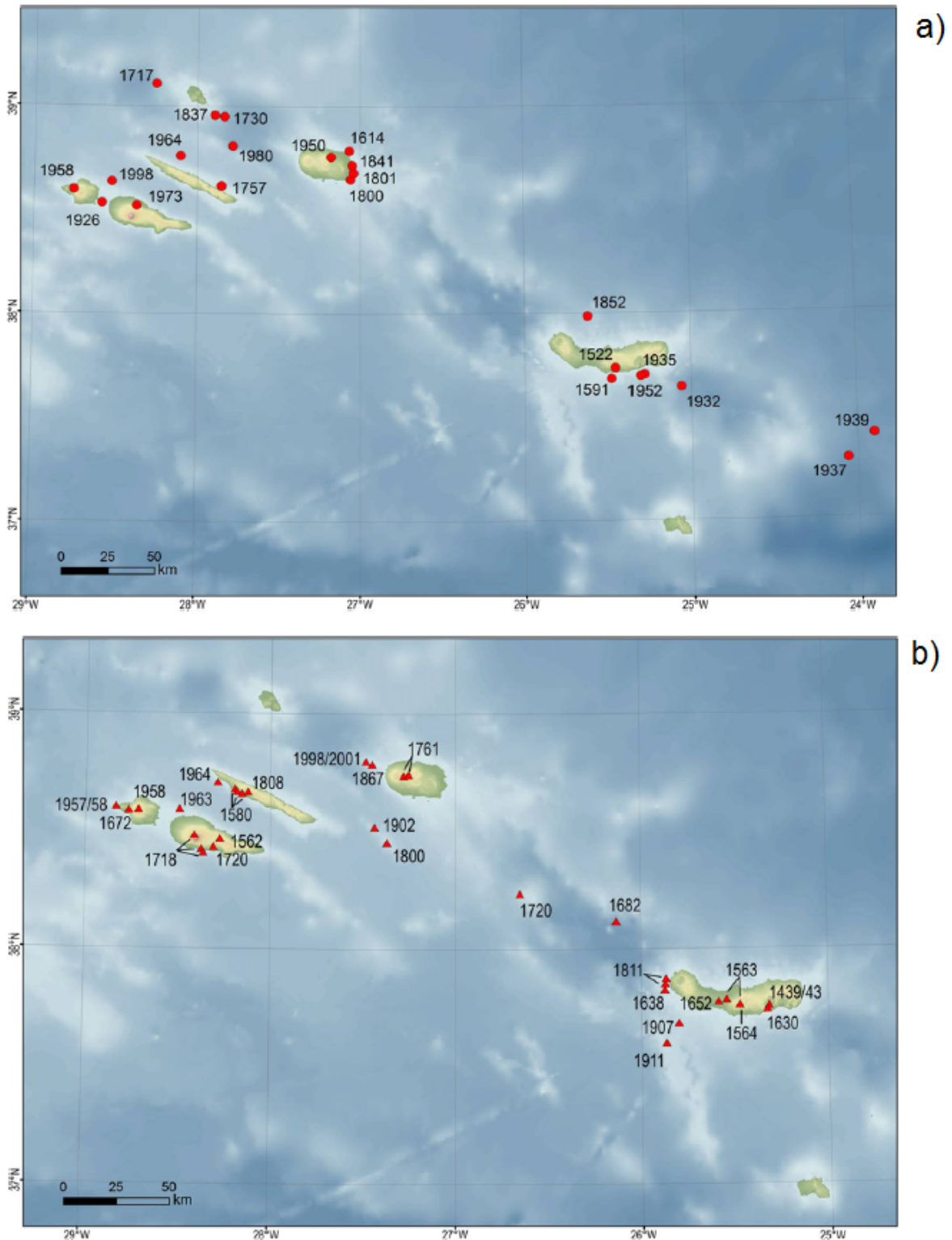


Figure 3.10: Historical seismicity and volcanism in the Azores archipelago. a) Epicentral locations of destructive earthquakes during historical times. b) Location of historical eruptions. [Adapted from *Gaspar et al.*, 2015, and references therein]

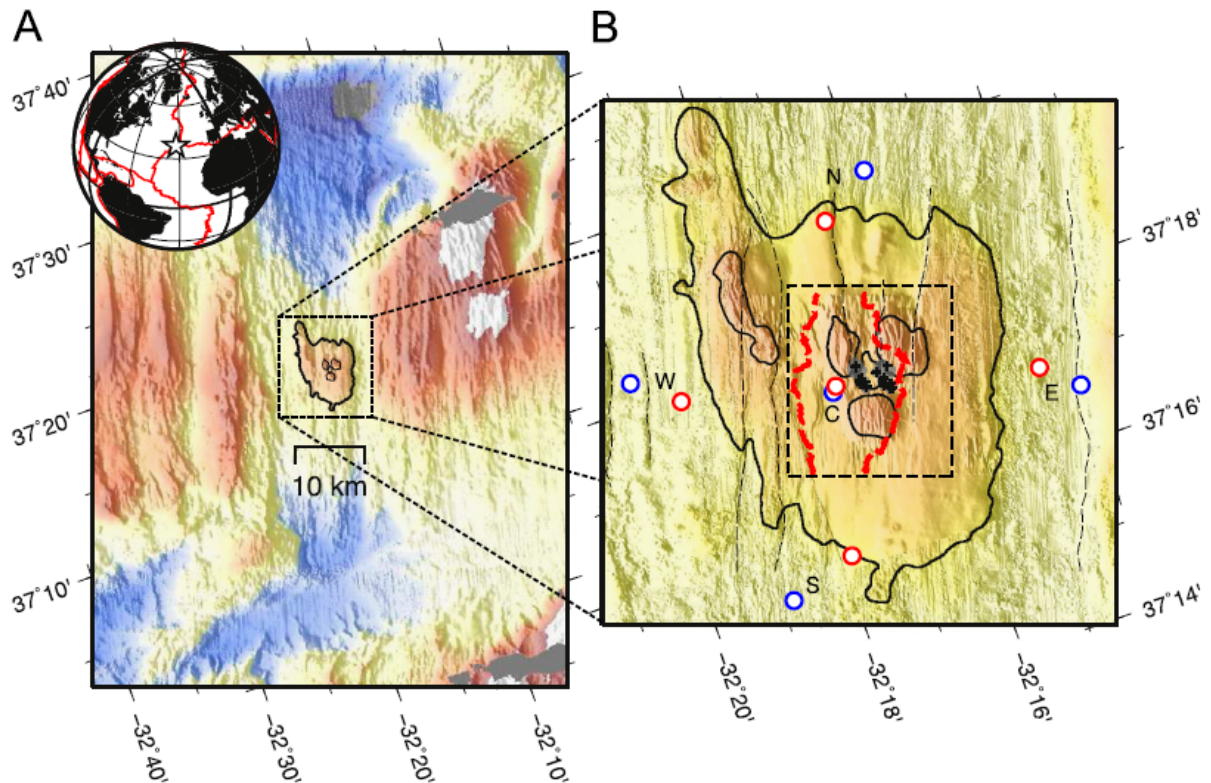


Figure 3.11: Maps of the Lucky Strike volcano. (A) The solid contour outlines Lucky Strike volcano. (B) Volcano scale. Solid contours are isodepths outlining the volcano base (1900 m beneath sea level (mbsl)), the western volcanic ridge (1660 mbsl), the summit depression (1710 mbsl) and its three surrounding peaks (1660 mbsl). Red dashed line marks the bounds of the Axial Magma Chamber (AMC) reflector. Black dashed lines mark significant surface faults. Black crosses mark hydrothermal vents. Circles mark OBS sites deployed in the MOMAR project cruises (blue (outer) 2007–2008, red (inner) 2008–2009) (section 4.3). [Adapted from *Crawford et al.*, 2013, and references therein]

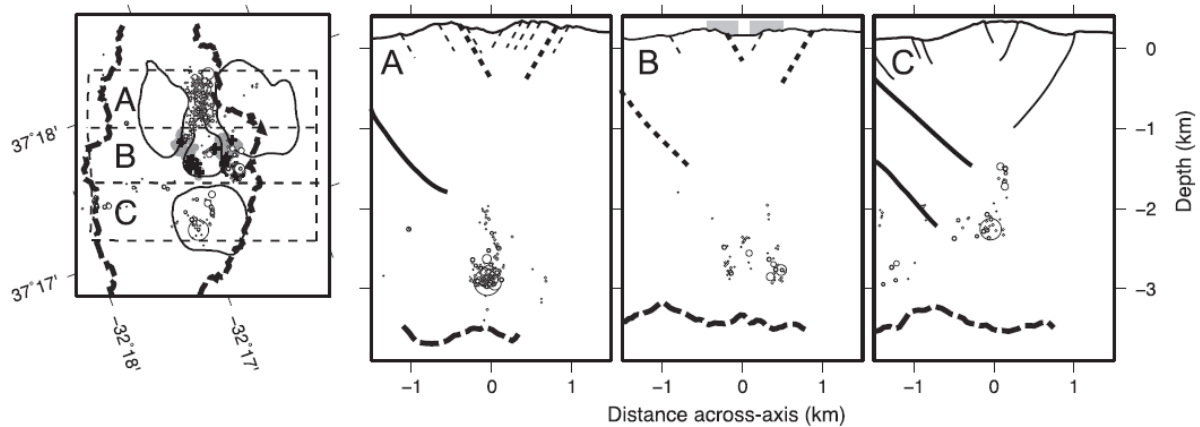


Figure 3.12: Across-axis cross-sections of seismic events located by *Crawford et al.* [2013] and subsurface structure. Solid lines=faults imaged using seismic reflection data, dashed lines=faults extrapolated from seafloor observations. Dashed grey line=AMC reflector. (A) Cross-section across the central graben north of the hydrothermal field. (B) Cross-section across the hydrothermal field, with seafloor hydrothermal discharge zones indicated in grey. (C) Cross-section across the south peak. [Adapted from *Crawford et al.*, 2013]

probably the heat source of the Lucky Strike hydrothermal system. Under the reflector was identified a seismic low velocity zone that extends down to the Moho [*Dusunur et al.*, 2009].

Seismicity on the Lucky Strike system

Dusunur et al. [2009] analysed the data from 21 OBS deployed centered at the hydrothermal field and the central volcano between 1st June and 3rd July 2005 during the SISMOMAR cruise. More than 400 events were detected at individual OBS stations with about 320 recorded only at one station that were interpreted as local seismicity with low magnitude. 71 events were located with local magnitudes up to 1.4. Most activity occurs at the northern (21 events) and southern (38 events) non-transform offsets that bound the Lucky Strike segment. The epicentral depths determined are superior to 10 km, in the upper mantle. In the central segment seismicity is scarce with 3 events beneath the central volcano at the edges of the axial magma chamber and depths superior to the seismic reflector.

Crawford et al. [2013] analysed data from two consecutive one-year OBS deployments part of the MOMAR project. Five OBS were deployed around the volcano from July 2007 to August 2009. A total of 1175 events were located (figure 3.12). Seismicity seems to concentrate in two locations: one beneath the southern peak of the volcano and another north of the central depression beneath the graben. The events are aligned with volcano's vent field and depths up to the seismic reflector. The authors interpreted this seismicity as mostly related to thermal contraction of rocks at the bottom of the hydrothermal cells or contraction of the magma chamber.

Chapter 4

Data

For the four regions described in chapter 3 data from several deployments in the scope of 4 projects and data from the Global Seismographic Network (GSN) and the Portuguese Seismic Network (PM) were used.

4.1 Deployments in Cape Verde

For the Cape Verde Archipelago data from two temporary deployments were used (figure 4.1).

Between July 2002 to September 2004, 7 temporary three-component broadband stations were deployed in the islands of Santo Antão, São Vicente, São Nicolau, Sal, Maio e Fogo (figure 4.1 A). Instruments were Guralp 3Ts with a sampling rate of 50 Hz and data were recorded on local hard disks. The deployment was made by the University of Bristol in collaboration with other institutions with the purpose to investigate shallow and deep mantle structure near a hotspot [Helffrich *et al.*, 2010].

Under the scope of the CV-Plume project 40 temporary three-component broadband stations were deployed between November 2007 and September 2008 (9A network, figure 4.1 B) [Vales *et al.*, 2014]. Stations were equipped with a Guralp CMG40T seismometer and an Earth Data Logger and recorded with a sampling rate of 100 Hz. For security and power purposes stations were generally deployed in power transformer stations. In the case of stations deployed outside they were powered by solar panels. Data were recorded locally on hard disks. The deployment was a collaboration between Instituto Dom Luiz (IDL, Portugal) and the GeoForschungsZentrum (GFZ, Deutschland) with the objective of imaging the seismic structure beneath the archipelago. Data were retrieved from the GFZ Seismological Data Archive in miniseed format.

SACV is a station from the Global Seismographic Network (IRIS-IDA) located in the island of Santiago (figure 4.1 A). Data from its entire working period were used. SACV station is equipped with a Geotech KS-54000 Borehole seismometer with a sampling rate of 20 Hz in the BHN, BHE and BHZ channels. The station is at a depth of 97 m. Data were retrieved from the IRIS Data Management Center in miniseed format.

4.2 Mozambique - project MOZART

In Mozambique, seismic data from a temporary deployment in the scope of project MOZART (Mozambique Rift Tomography) were used [Fonseca *et al.*, 2014] (figure 4.1). This project sought to delineate the active structures of the EARS, study the crust and upper mantle and the processes of continental rifting and rifting initiation in the region of Mozambique.

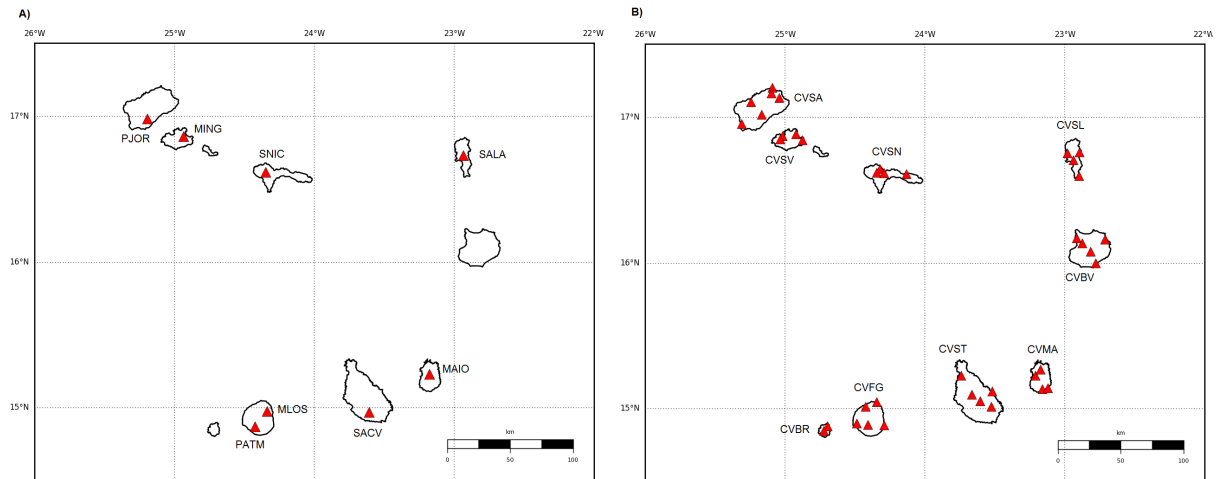


Figure 4.1: Locations of the stations from the two temporary deployments and the permanent SACV station. A) 2002-2004 deployment and SACV station from the Global Seismological Network. B) 2007-2008 deployment. Coordinates of stations are given in appendix F.

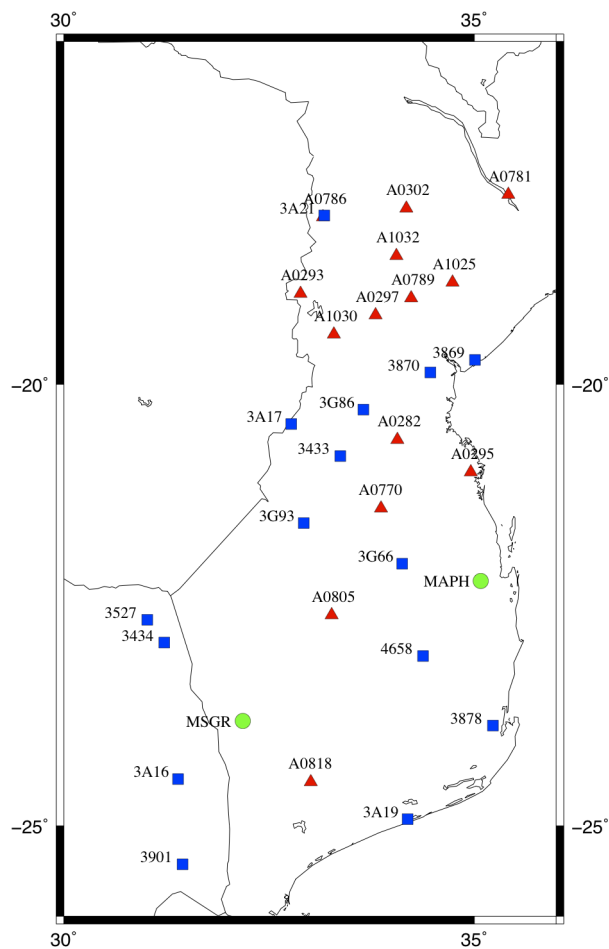


Figure 4.2: Locations of the stations from the MOZART deployment between 2011 and 2013. Red triangles - Taurus stations; Blue squares - Guralp stations; Green circles - stations of Africa Array. Coordinates of stations are given in appendix F.

Thirty three-component broadband stations were deployed in central and southern Mozambique and in NE South Africa in the Kruger Park along the border. The deployment started in March 2011 and the stations were recovered in August 2013. The deployment was made in two phases, a first phase with the deployment of only 9 stations in the northern part of the study area and a second phase with the deployment of the other 21 stations in November and December 2011. Average interstation distances were about 100 km and varied between 35 to 940 km. The stations consisted of CMG-3T (120 s) seismometers and Nanometrics Taurus or Guralp CMG-DMC dataloggers and GPS clocks from the SEIS-UK Equipment Pool. Stations were deployed in sites away from cultural noise sources like busy roads and in good underground conditions, in general, taking in account the bedrock type. In sites with no shelter the instruments were buried in the ground. Stations were powered by solar panels and data were recorded directly to a hard disk.

Some stations were affected by problems like cyclonic rainfall and power issues and some were vandalized, leading to relocation of some of the stations.

Data from two three component broadband stations of the Africa Array were also used. The MSGR station deployed in Massingiri in August 2011 and the MAPH station deployed in Mapinhane in July 2011, both equipped with a Nanometrics Trillium Compact (120 s) seismometer and a Reftek 130 Datalogger.

The data were in miniseed format and some problems were found during its conversion to SAC format because some of the dataless files sampling rate were not in accordance with the one registered in the miniseed files.

4.3 OBS deployments in the Lucky Strike Volcano

For the Lucky Strike segment data from 4 yearly OBS deployments around the Lucky Strike volcano were used (figure 4.5). These deployments were part of the MOMAR project and were deployed by 4 cruises [*Crawford et al.*, 2013]:

- BBMOMAR I - July 2007; deployed 4 short period OBSs (O1 - O3) and 2 broadband OBSs (O7 and O8);
- BBMOMAR II - August 2008; retrieved previous OBSs and deployed 4 short period OBSs (O1 - O4) and 1 broadband OBS (O7);
- BATHYLUCK09 - September 2009; retrieved previous OBSs and deployed 4 short period OBSs (C1 - C4) and 1 broadband OBS (C7);
- MomarSat2010 - October 2010; retrieved previous OBSs and deployed 4 short period OBSs (D1 - D4);
- MomarSat2011 - July 2011; retrieved previous OBSs.

All OBSs had a sampling rate of 62.5 Hz and 4 components X, Y, Z (vertical) and hydrophone. The array aperture for the first three deployments was of about 7-8 km.

The short period OBSs were equipped with a Mark Products L-28LB three-component Geophone and an Hitech HYI-90-U hydrophone. The broadband OBSs were equipped with a Nanometrics Trillium T240 seismometer and a differential pressure gauge.

Data were in GSE format and were converted to miniseed using ObsPy before choosing the relevant data. Data in all components have abrupt jumps that last for some seconds with a periodicity of about 2 hours and 40 minutes, only the broadband station C7 does not have this data problem (figure 4.4).

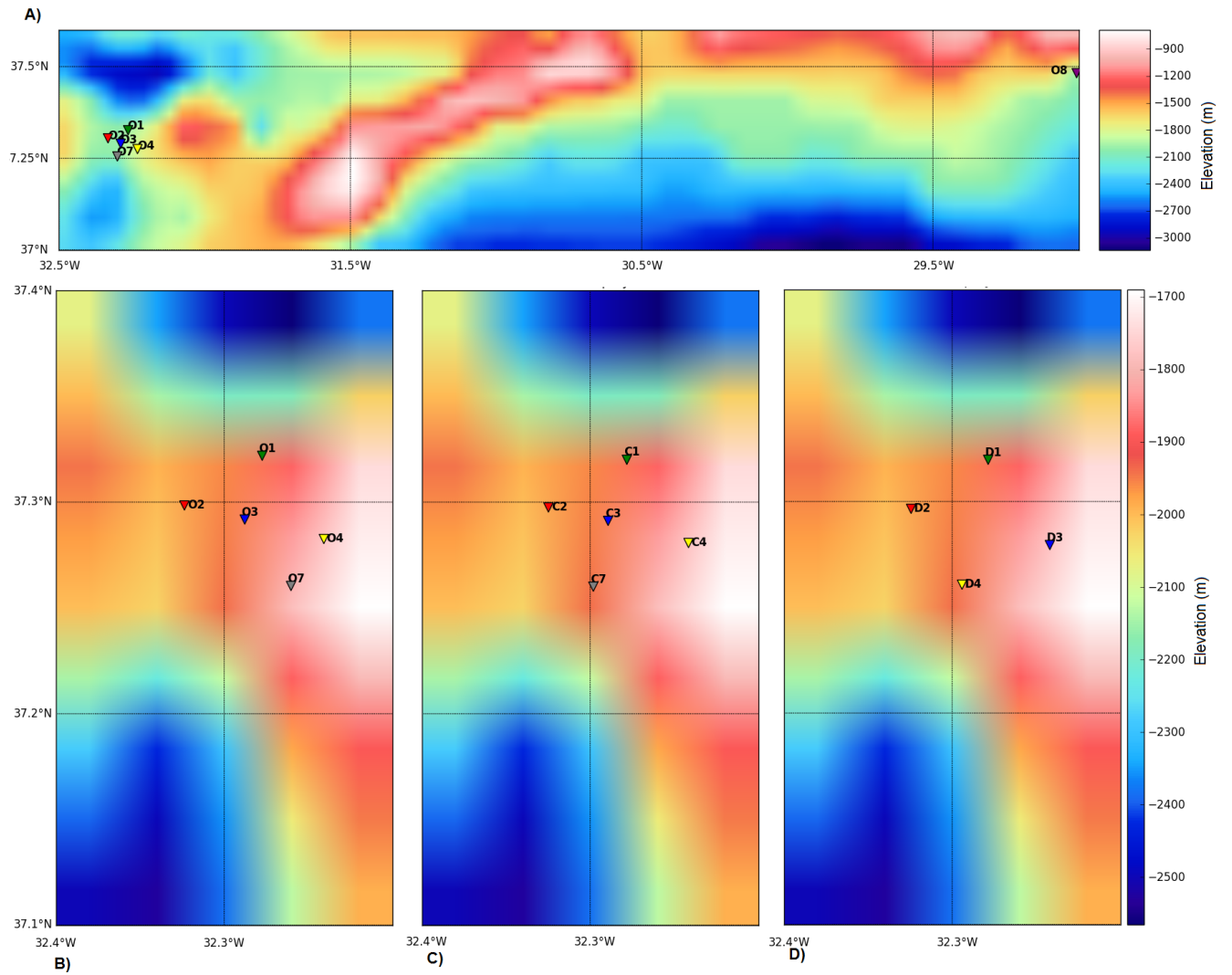


Figure 4.3: Locations of the OBSs deployed as part of the MOMAR project. A) BBMOMAR I; B) BBMOMAR II; C) BATHYLUCK09; D) MomarSat2010. Coordinates of OBSs are given in appendix F.

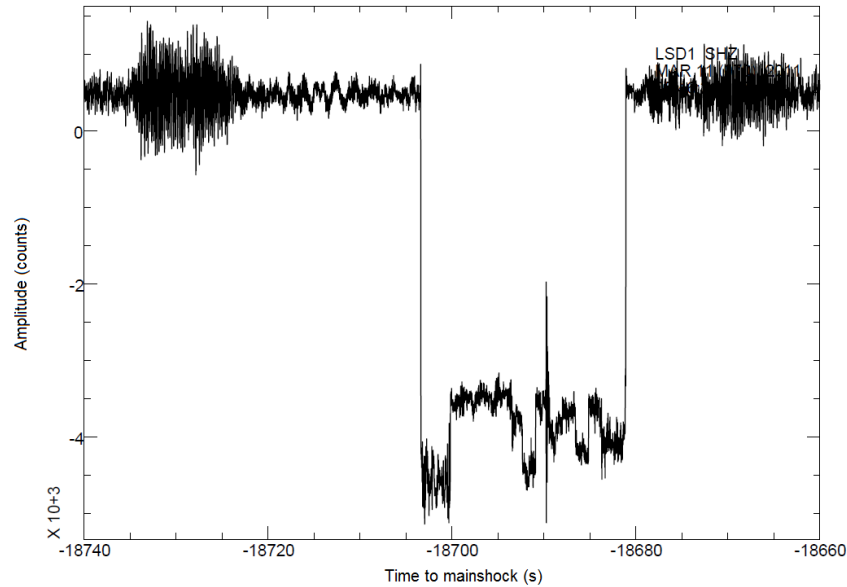


Figure 4.4: Abrupt jump in data observed in several OBS stations. This was recorded in station D1 before the arrival of mainshock C that will be analyzed in section 8.1

4.4 Permanent stations in the Azores Archipelago

In Azores data from the CMLA station from the Global Seismographic Network (IRIS/IDA) and from the ROSA station from the Portuguese Seismic Network for their entire working period were used. Data from both stations were retrieved in miniseed format from the IRIS Data Management Center.

CMLA is a permanent station located at Chã de Macela in the island of São Miguel. Data used were from a three-component broadband Geotech KS-54000 borehole seismometer at a depth of 97 m. Data from this station are available since March 1996. Data have a sampling rate of 20 Hz.

ROSA is a station located at Rosais in the island of São Jorge and is a three-component broadband station. It is equipped with a Guralp CMG-3ESPc seismometer (120 s) and a 5T datalogger. Data since March 2008 are available. Data have a sampling rate of 20 Hz.

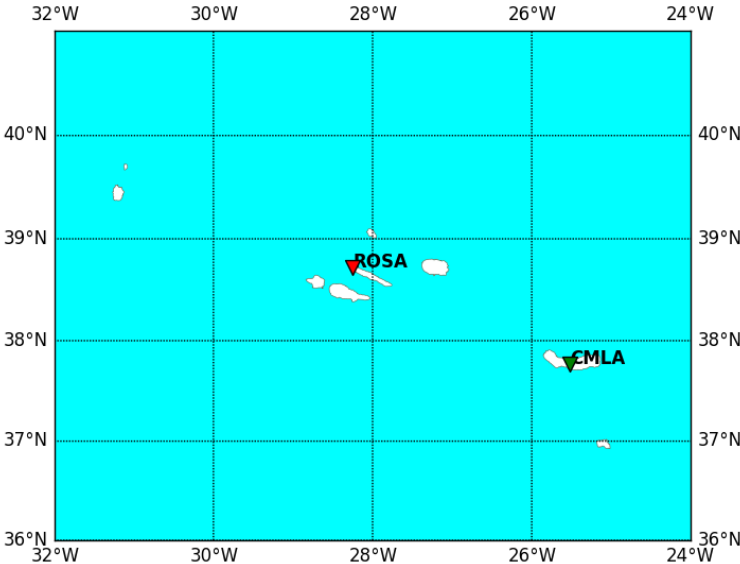


Figure 4.5: Locations of the permanent stations in Azores. ROSA station is located in São Jorge island and CMLA in São Miguel island. Coordinates of stations are given in appendix F.

Chapter 5

Methods

5.1 Selection of distant mainshocks

A selection of the distant shallow mainshocks to analyze was made taking into account the expected dynamic stress which in turn depend on the earthquake magnitude, distance to study region and hypocentral depth.

Firstly, for each study region a reference station was chosen that was used for the distance and dynamic stress criteria. Ideally this station is at the center of the study area. In the Lucky Strike Volcano the station considered as reference was O3, in Cape Verde was the CVSN4 station for the 2007-2008 deployment and the SNIC station for the 2002-2004 deployment and in Mozambique was the A0770 station.

Secondly, a catalogue with all earthquakes with magnitude ≥ 5.5 , depth ≤ 100 km and epicentral distance to reference station ≥ 100 km for each case was downloaded from the USGS (United States Geological Survey) Earthquake archives.

Thirdly, for each of these earthquakes the expected dynamic stress at the reference station was estimated using magnitude relationships as in *van der Elst and Brodsky* [2010]. The dynamic stress (σ) is roughly proportional to the ratio between the particle velocity (V) and the seismic wave velocity (C_S) (Equation 5.1). In the near-field (events at distances < 800 km) velocity was estimated with equation 5.2 that relates the Peak Ground Velocity (PGV) with the event magnitude (M) and the epicentral distance (r) in km. For the far-field (events at distances ≥ 800 km) equation 5.3 that relates the surface wave magnitude (M_S) with the amplitude (A_{20}) of the surface Rayleigh wave, with a period (T) of 20 s, and the epicentral distance (Δ) in degrees was used. Dynamic stress was then estimated considering a velocity of 3.5 km/s for the 20 s period Rayleigh wave and a shear modulus (μ) of 35 GPa. This calculation assumes that the magnitude reported in the catalogue is the surface wave magnitude. Although the magnitude reported in the catalogs is usually Mw, the assumption does not hinder the analysis.

$$\sigma \approx \frac{V\mu}{C_S} \quad (5.1)$$

$$\log_{10}PGV = -2.83 + M - 1.29\log_{10}\sqrt{r^2} \quad (5.2)$$

$$\log_{10}A_{20} = M_S - 1.66\log_{10}\Delta - 2, \quad V \approx \frac{2\pi A_{20}}{T} \quad (5.3)$$

Finally, only the events with a dynamic stress ≥ 1 kPa were selected for analysis.

Due to the reduced number of events chosen for Cape Verde with these criteria for the 2007-2008 de-

ployment period, additional ones were selected taking into account only earthquake magnitude, distance to study region and hypocentral depth. A catalogue of earthquakes with magnitude ≥ 7 , depth ≤ 100 km and epicentral distance to reference station ≥ 1000 km was retrieved from USGS Earthquake archives.

5.2 Data processing

This section describes the processes applied to the waveform data before the event detection. Processing was mainly done in *MATLAB*, in *Python* with *ObsPy* (Python Framework for Seismology, *Beyreuther et al.* [2010]) and some steps with *SAC* (Seismic Analysis Code).

For each of the events previously chosen we retrieved the three-component waveform data for 6 hours before and after the mainshock and converted to SAC format, using *ObsPy*. Only stations with data for the three components for all the 12 hours were used.

Instrument response is removed by performing a deconvolution and a convolution is applied to obtain velocity with a flat response between 0.005 Hz and $0.8f_N$ (f_N is the Nyquist frequency), using the polezero files for each station. North and East component were also rotated to the Great Circle Path (GCP) to obtain Radial and Transverse component, this was not done with the OBS data because the horizontal components are not oriented.

To remove the long period signals from the distant mainshock and possible aftershocks each component is filtered using a Butterworth, two-way, 4th order filter. In a first attempt we try a high-pass filter > 5 Hz because we are searching for local seismic activity. If a contamination of the results by noise was observed this step was repeated using band-pass filters. The identification of possible noise frequencies was made with spectrograms. Before applying the filter the data was tapered with a Hann window with 0.05 width and the mean was removed.

The envelope function of each filtered component was computed using a Hilbert transform with *SAC*. The envelope function is defined by $E(t) = \sqrt{s(t)^2 + \bar{s}(t)^2}$, where s is the seismogram and \bar{s} is the Hilbert transform, and can be described as a positive outline of the seismogram.

The envelope of each component were then smoothed with a moving window with a half-width of 2.5 s and taken its log-based-10. The resulting log-envelopes of each component were stacked to obtain an averaged envelope function to increase the signal to noise ratio. The resulting envelope stack was decimated to 2 samples/s. This final averaged envelope was used in the high-energy bursts detection explained in the next section.

In summary, the steps for the processing of the waveform data were:

1. Retrieve data for ± 6 hours around the mainshock for each component;
2. Remove instrument response;
3. Rotate to GCP (not in the case of OBS data);
4. High-pass filter;
5. Take envelope of filtered components;
6. Compute averaged envelope function and decimate to 2 samples/s.

Determination and Timing of Phase Arrivals

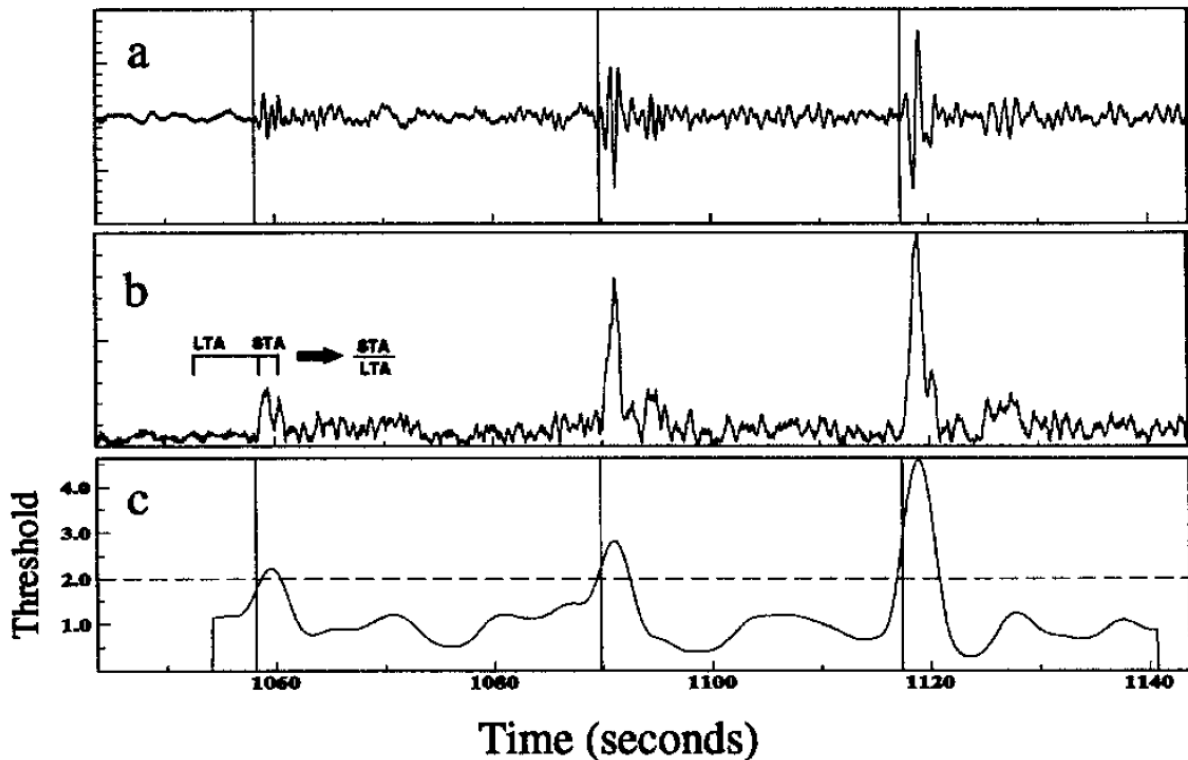


Figure 5.1: Example of a STA/LTA automatic detection algorithm to determine phase arrivals. (a) Short-period seismogram with autopicks plotted as vertical lines. (b) Envelope function and STA-LTA windows. The LTA and STA windows have been enlarged for visualization. (c) STA/LTA ratio (solid) and threshold (dashed). The trigger points are the intersections of the increasing STA/LTA ratio and the threshold. The pick times (vertical lines) are defined by the inflection point that precedes the local maximum immediately following the trigger point. [Adapted from *Earle and Shearer, 1994*]

5.3 Burst detection and triggering statistics

High-frequency bursts in the 12 hours data were automatically detected using a short-term average/long-term average (STA/LTA) algorithm in the averaged envelope. The algorithm used was made by *Peng et al.* [2014], based on *Earle and Shearer* [1994].

The STA/LTA methods use two moving windows or averages. A long-term average (LTA) that is followed directly by a short-term average (STA). The STA measures rapid increases in the amplitude and the LTA measures the local background amplitude [*Earle and Shearer, 1994*]. For each data point, we calculated the ratio of the STA to LTA that is considered a measure of the local signal-to-noise. The algorithm has also a defined STA/LTA ratio threshold value and a positive detection is declared when the ratio is higher than the threshold. Figure 5.1 has an example by *Earle and Shearer* [1994] on the use of a STA/LTA automatic detection algorithm to determine phase arrivals.

The threshold ratio was defined as 1.5 and a STA and LTA of 2 and 10 s, respectively, were used to detect high-frequency short duration bursts and of 10 and 50 s, respectively, to detect longer duration high-frequency bursts.

Using the beta statistics (section 2.5) the β value was calculated considering the events detected before the P wave arrival to compute the background rate and compared it to the the instantaneous triggering window, events detected between the arrival of seismic energy traveling at 5 and 2 km/s when most of

the surface wave energy passes. The cases with $\beta \geq 2$ are considered to have a statistically significant increase of high-frequency bursts. Only after visual inspection of the waveforms of each event were the cases defined as positive or negative cases of triggering, in order to avoid false positive due to instrumental issues, such as clipping, or noise contamination that lead to an increase or reduction of bursts.

Chapter 6

Cape Verde

In Cape Verde 12 mainshocks were selected according to the method that takes into account a minimum dynamic stress, 4 for the 2002-2004 deployment, 3 for 2007-2008 deployment and 5 only recorded in the SACV station. For the 2007-2008 period additional 8 events (section 5.1) with magnitude > 7 and epicentral distance to reference station ≥ 1000 km were selected based in the observations that in some regions higher magnitude earthquakes seem to be more efficient at triggering [Brodsky and Prejean, 2005]. The mainshocks characteristics and the respective number of analyzed stations are given in tables 6.1 and 6.2 and in figure 6.1.

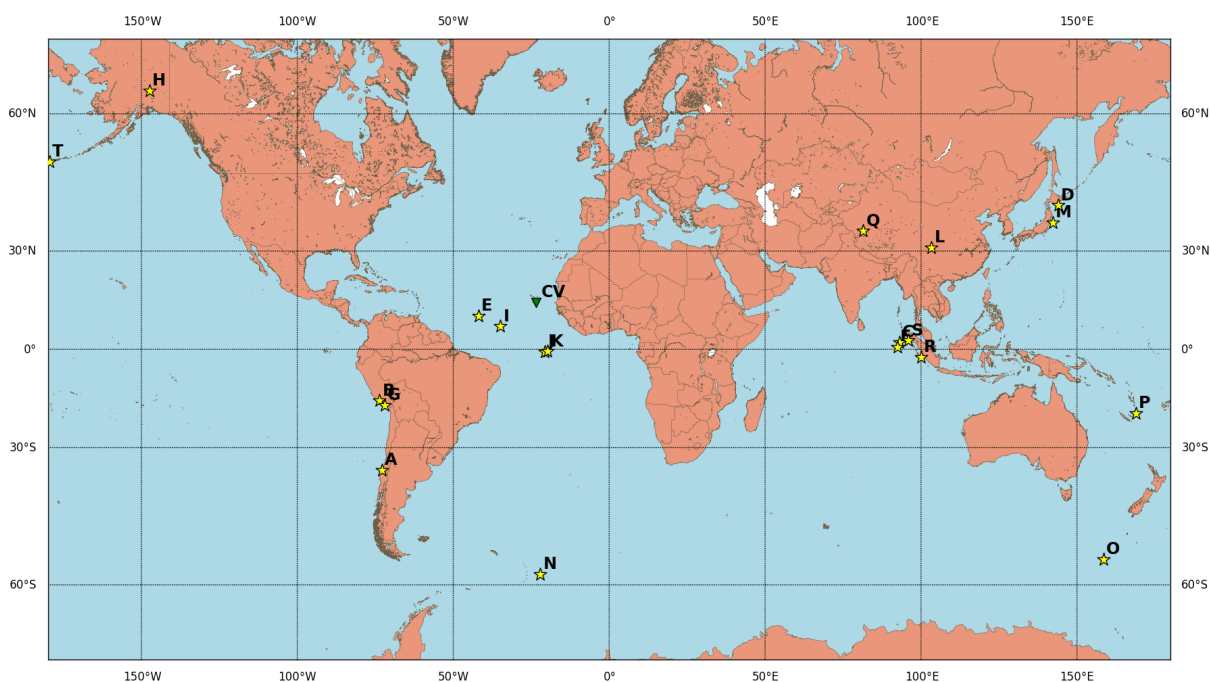


Figure 6.1: Map of 20 mainshocks (tables 6.1 and 6.2) analyzed in Cape Verde (CV - green triangle). The epicenters are marked by the yellow stars. Mainshocks have $M_w \geq 5.5$ and hypocentral depths ≤ 100 .

6.1 Results

In a first run of the STA/LTA detection algorithm the windows for detecting short duration high-frequency energy bursts were used. The analysis of the detected signals revealed that the majority had durations longer than 2 seconds and some were being detected multiple times. A new run of the algorithm was

Attributed identification	Mainshock (UTC)	Longitude	Latitude	Depth (km)	Magnitude (Mw)	Distance (km)	Estimated σ (kPa)	Analyzed Stations
A	2010/02/27 06:34:11.53	-72.898°	-36.122°	22.9	8.8	7663.21	17.599	1
B	2001/06/23 20:33:14.13	-73.641°	-16.265°	33.0	8.4	6487.38	9.238	1
C	2012/04/11 08:38:36.72	93.063°	2.327°	20.0	8.6	12790.96	4.744	1
D	2003/09/25 19:50:06.36	143.910°	41.815°	27.0	8.3	13438.42	2.191	7
E	2008/02/08 09:38:14.10	-41.899°	10.671°	9.0	6.9	2028.44	2.012	38
F	2012/04/11 10:43:10.85	92.463°	0.802°	25.1	8.2	12777.18	1.892	1
G	2001/07/07 09:38:43.52	-72.077°	-17.543°	33.0	7.6	6415.00	1.492	1
H	2002/11/03 22:12:41.00	-147.444°	63.517°	4.9	7.9	9884.12	1.452	5
I	2008/05/23 19:35:34.78	-34.897°	7.313°	8.0	6.5	1557.22	1.243	36
J	2003/12/21 07:40:45.83	-20.601°	-0.769°	10.0	6.6	1964.73	1.063	7
K	2003/11/09 19:52:36.82	-19.689°	-0.674°	10.0	6.6	1977.96	1.052	6
L	2008/05/12 06:28:01.57	103.322°	31.002°	19.0	7.9	12319.74	1.007	34

Table 6.1: Events analyzed in Cape Verde, selected with the criteria including a limitation in expected dynamic stress

Attributed identification	Mainshock (UTC)	Longitude	Latitude	Depth (km)	Magnitude (Mw)	Distance (km)	Estimated σ (kPa)	Analyzed Stations
M	2008/02/20 08:08:30.52	95.964°	2.768°	26.0	7.4	13100.29	0.288	37
N	2008/03/20 22:32:57.93	81.467°	35.490°	10.0	7.2	10301.75	0.271	35
O	2008/06/30 06:17:43.02	-22.099°	-58.227°	8.0	7.0	8293.11	0.245	33
P	2007/12/19 09:30:27.93	-179.509°	51.360°	34.0	7.2	12117.15	0.207	38
Q	2008/02/25 08:36:33.03	99.972°	-2.486°	25.0	7.2	13712.62	0.168	34
R	2008/04/09 12:46:12.72	168.892°	-20.071°	33.0	7.3	18587.97	0.128	35
S	2008/04/12 00:30:12.60	158.453°	-55.664°	16.0	7.1	15675.57	0.107	35
T	2008/07/19 02:39:28.70	142.214°	37.552°	22.0	7.0	13856.27	0.104	32

Table 6.2: Additional events with magnitudes ≥ 7 analyzed in Cape Verde for the 2007-2008 deployment

Station	Mainshock			
	D	H	J	K
MAIO	-2.229		2.878	
MLOS		2.026		
SALA			2.668	2.203
SNIC			2.363	
SACV				4.300

Table 6.3: Cases with $|\beta| \geq 2$ for the stations of the 2002-2004 deployment and the permanent SACV station in Cape Verde

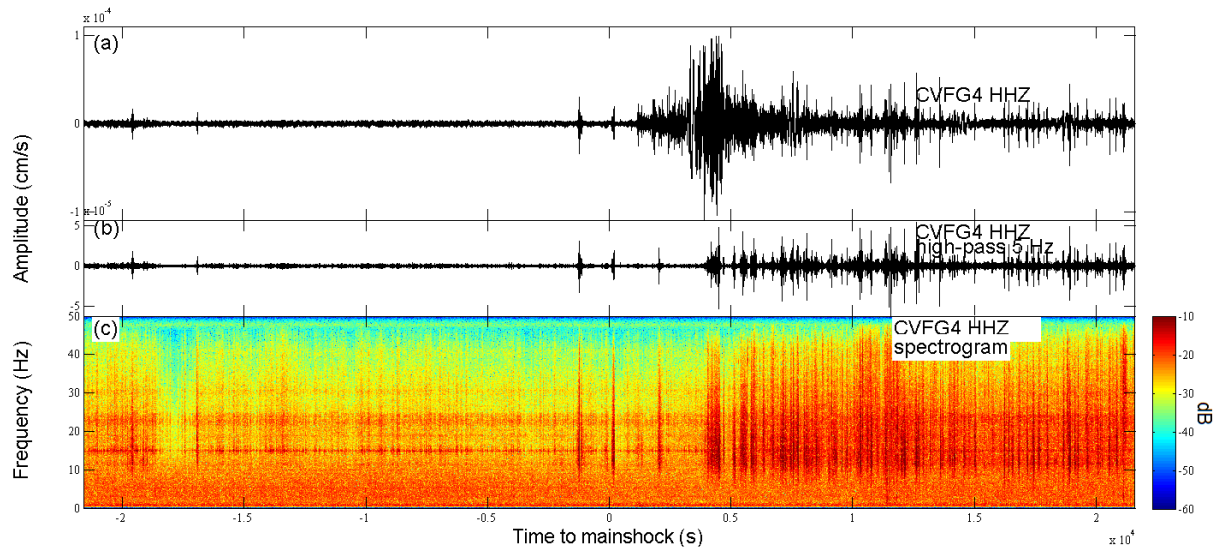


Figure 6.2: Data analyzed for mainshock L in station CVFG4. a) Raw vertical component; b) 5 Hz high-pass filtered vertical component; c) Vertical component spectrogram. An increase in high-frequency energy bursts occurs during the passage of the surface waves that is sustained after the surface wave train end.

made using the windows for detecting longer duration bursts. With this new run the repeated detection of the same signal did not occur. The cases for which the calculated β -values show a significant increase or decrease of high-frequency energy bursts ($|\beta| \geq 2$) can be seen in table 6.3, for the events recorded in the 2002-2004 deployment and SACV stations, and in table 6.4 for the events recorded in the 2007-2008 deployment stations. The determined β -values for all stations for each mainshock are in appendix A.

The results show two mainshocks (mainshock L and O) where a generalized increase in high frequency energy bursts in the southwest islands (Fogo, Brava, Santiago and Maio), in the northwest island of Santo Antão and also in São Vicente, in the case of mainshock O, that coincides with the passage of the seismic waves. Figure 6.2 shows an example of this observation in station CVFG4 during the passage of mainshock L seismic waves. This increase of bursts of high-frequency energy seems to continue even after the surface wave train has ended.

Mainshocks L, M, N, P, Q and R show increases in high-frequency energy activity that start before the arrival of the seismic waves (an example is shown in figure 6.3). In all cases with a $\beta \leq -2$, that indicate that a possible decrease in high-frequency seismic energy activity occurred during the passage of the seismic waves, the decrease in the activity occurs before the arrival of the seismic waves. The decrease is therefore not related to the passage of the seismic waves.

Mainshocks J, K, E and I have a significant increase in activity that result from the detection of 1 or

Station	Mainshock										
	E	I	L	M	N	O	P	Q	R	S	T
CVBR1	2.046		7.349	4.418		6.495		3.987			-2.846
CVFG1			2.765	4.21		5.172	2.044	3.08		-2.118	
CVFG2			5.434	5.756		2.977					
CVFG3	2.759		2.949	6.406				3.975		-2.867	
CVFG4			3.243	4.577		4.735			2.194		
CVFG5			5.577							-2.628	
CVMA1			2.475	5.587		7.923	3.671				
CVMA2				6.527		3.086					-2
CVMA3			2.132		-2.424					-2.023	
CVMA4						4.316					-2.017
CVST1			3.724	2.693		2.69	2.218				
CVST2			2.893	4.014				2.315		-2.604	-3.19
CVST3				5.74							
CVST5	2.425		4.332	5.488	-2.687	3.038	2.749	4.257		-4.54	
CVBV1	2.458		5.098	5.89			3.802	4.671			-2.991
CVBV2					-3.046		3.869				
CVBV4					-2.107	2.489	5.617		2.353		-2.653
CVBV6						2.702	6.299				
CVSA1			2.796	3.028		4.845	3.03	3.821		-4.402	-2.978
CVSA2				7.195				6.689		-2.44	-2.876
CVSA3			2.991	4.008		2.326	2.719	4.063			
CVSA4			2.838	5.483		3.265		3.441		-2.164	-2.608
CVSA5			-2.17							2.836	2.511
CVSA6							-2.164				
CVSL1				3.835				2.454	2.194		-2.828
CVSL2				3.819			2.15				
CVSL3				8.985			6.653				
CVSL4				4.665				4.363		-3.287	-2.566
CVSN1			7.816	6.1		2.996		6.164		-3.219	
CVSN2	3.094					5.153		2.817		-2.227	
CVSN3				5.877458			3.388027				
CVSV1	4.055	6.458		10.28	-2.762	4.67	5.966				
CVSV2				6.754		2.909	3.526				
CVSV3			2.429				3.107				
CVSV4				4.319	-2.311	4.234		3.261		-2.747	-2.035

Table 6.4: Cases with $|\beta| \geq 2$ for the stations of the 2007-2008 deployment in Cape Verde

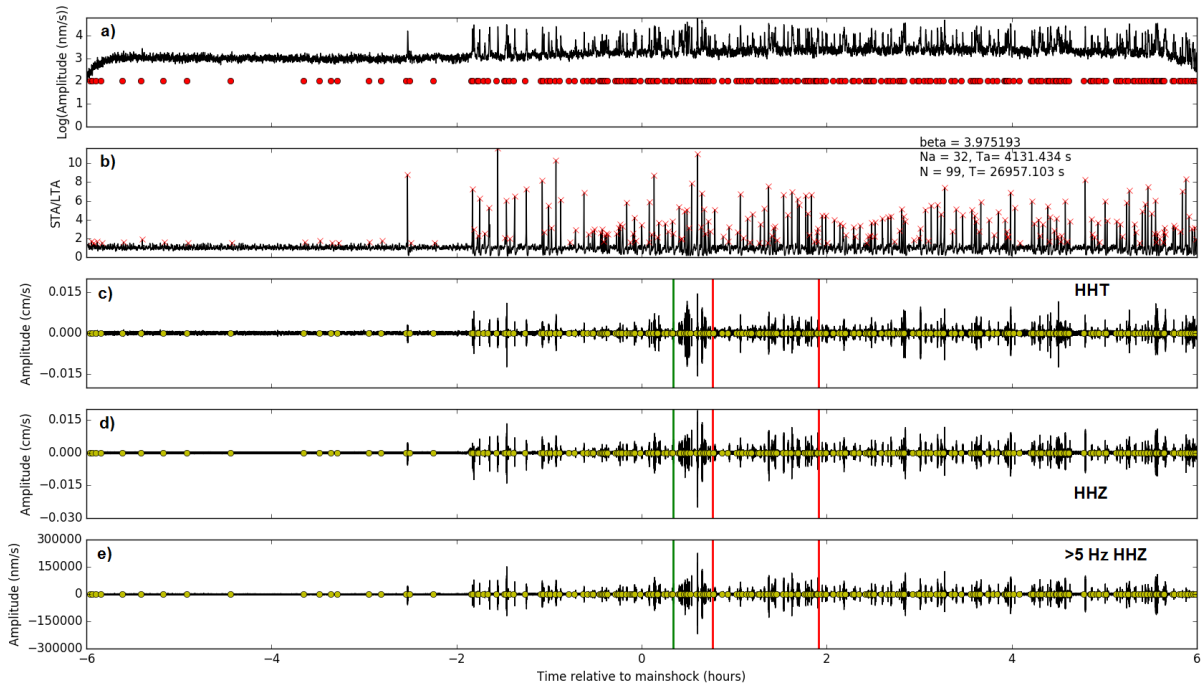


Figure 6.3: Data analyzed from station CVFG3 for mainshock **Q**. a) Three-component average envelope; b) STA/LTA ratio; c) Raw transverse component; d) Raw vertical component; e) 5 Hz high-pass filtered vertical component. Green line marks the manual picked P-wave arrival; Red lines delimit the triggering window. An increase in detected high-frequency signals occurs during the passage of the seismic waves.

2 high-frequency bursts, as detected by the STA/LTA threshold, in the triggering window.

MLOS station, located in Fogo island in the Fogo volcano caldera, records an increase of bursts of high-frequency energy during the passage of the Mw7.9 Denali earthquake (Mainshock **H**) seismic waves (figure 6.4).

6.1.1 Cultural Noise

From the results we identified an increase in high-frequency energy bursts in various stations in the morning that lasts until the afternoon. This led to an analysis of the envelopes of the 5 Hz high-pass filtered vertical components for various days (figure 6.5). From the envelopes of the 10 days before mainshock **L** we recognize a daily pattern of high-frequency energy bursts increase between 6 UTC and 8 UTC in most of the 2007-2008 stations. This pattern is also observable in the majority of the 2002-2004 deployment. The diurnal variation of these high-frequency signals suggests they are noise related to human activity, also referred to as cultural noise. Cultural noise is mainly characterized by high-frequency waves that attenuate in a few kilometers.

Station SACV, a borehole station, and stations MLOS and MAIO, deployed far from populations, do not record this strong pattern of noise.

The noise signals are stronger in frequencies higher than 5 Hz but some appear to be present in all the spectrum. Some attempts to try to filter the noise were made with a 2-4 Hz band-pass filter but the diurnal variation of culture noise was still observable.

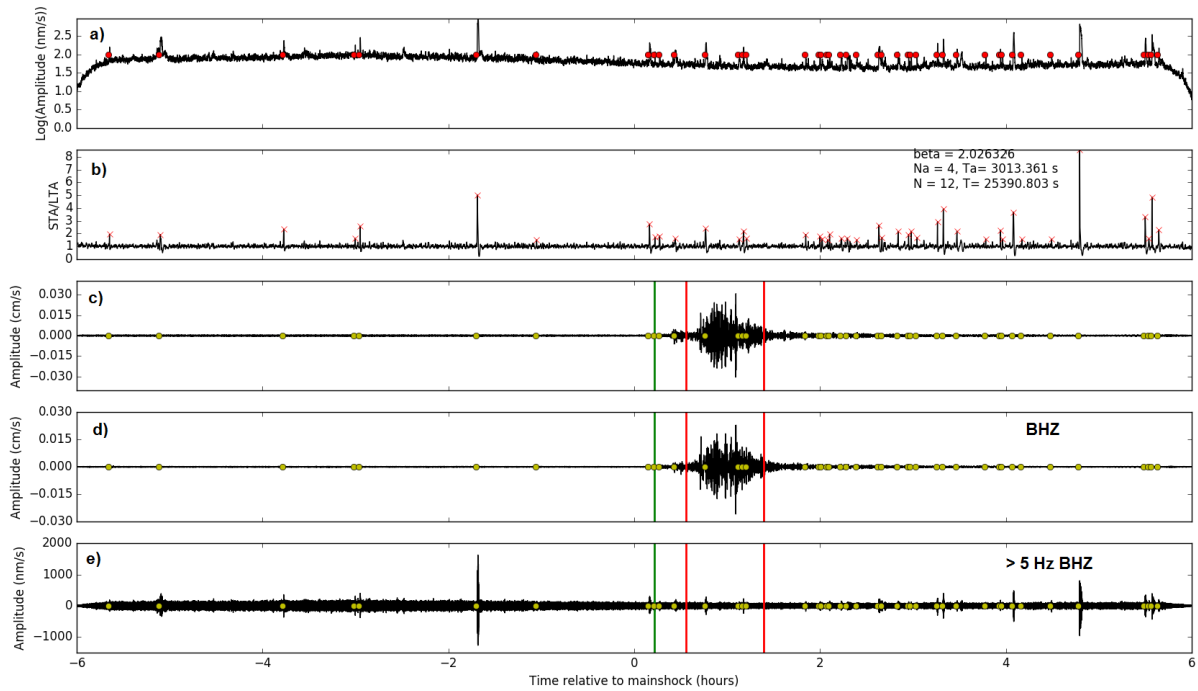


Figure 6.4: Data analyzed from station MLOS for mainshock H. a) Three-component average envelope; b) STA/LTA ratio; c) Raw transverse component; d) Raw vertical component; e) 5 Hz high-pass filtered vertical component. Green line marks the manual picked P-wave arrival; Red lines delimit the triggering window. An increase in detected high-frequency signals occurs during the passage of the seismic waves.

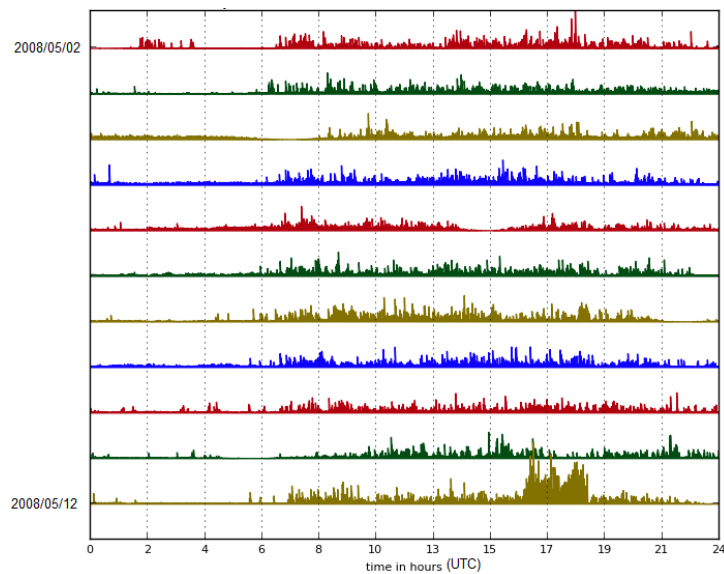


Figure 6.5: Dayplot of the 5 Hz high-pass filtered vertical component envelope from station CVFG4, from 2008/05/02 to 2008/05/12 (day of mainshock L)

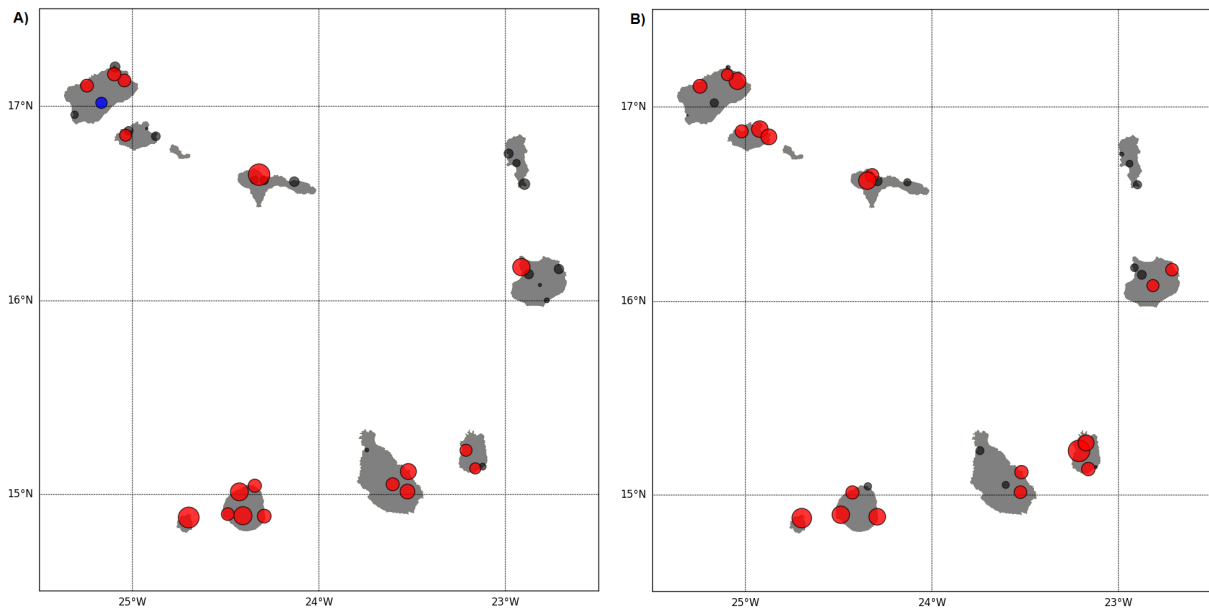


Figure 6.6: Maps with the registered β 's during the passage of the mainshocks **L** (figure A) and **O** (figure B) surface waves. Red circles represent stations with a significant increase in high-frequency activity and blue a significant decrease. A generalised increase is observed in the more western islands.

6.1.2 The May 12th, 2008, Mw7.9 Eastern Sichuan and the June 30th, 2008, Mw7.0 South Sandwich Islands Region earthquakes (Mainshocks L and O)

The passage of the seismic waves generated by the May 12th, 2008, Mw7.9 Eastern Sichuan and the June 30th, 2008, Mw7.0 South Sandwich Islands Region earthquakes (Mainshocks **L** and **O**) correspond to a generalized increase in high frequency bursts ($\beta > 2$) in the southwest islands and in the northwest island of Santo Antão and also in São Vicente in the case of mainshock **O** (figure 6.6). In most of these islands have been identified active volcanic structures or submarine volcanic structures in its surroundings (section 3.1.1). The increase of detected signals starts with the passage of the surface waves in the majority of the stations, although in some stations the increase seems to correspond to the arrival of the S wave (figure 6.7). In the cases the bursts start with the surface waves, the signals appear to start near a velocity maximum (figures 6.8 and 6.9).

The detected signals in the triggering windows are emergent and tremor-like and appear to have a duration of 10 seconds up to more than 4 minutes. No coherent signals between stations were identified.

Mainshock **L** and **O** occurred at a similar time and the P-wave is detected in the archipelago at about 6:47 UTC for mainshock **L** and 6:29 UTC for mainshock **O**, during the period where the start of the cultural noise increase occurs (section 6.1.1).

Making the same analysis for the same time period in the 7 days before the mainshock **L**, using radial and transverse components considering the origin of the mainshock, a significant increase in high-frequency activity is detected in almost every day with β -values that can be greater than those determined during the passage of the mainshock (table 6.5). Only in the day before, a Sunday, this generalized increase in activity is not observed.

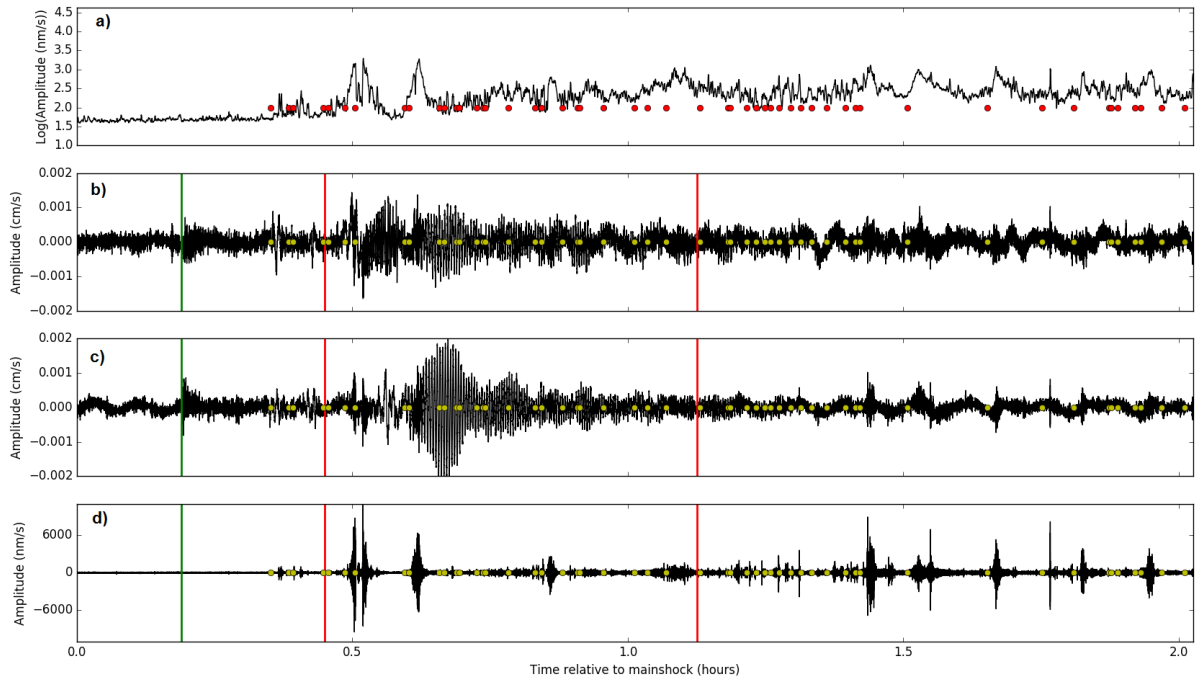


Figure 6.7: Example of a case where the increase in high-frequency activity during the passage of mainshock **O** seismic waves appears to start with the arrival of the S-wave. a) Three-component >5 Hz average envelope; b) Raw transverse component; c) Raw vertical component; d) 5 Hz high-pass filtered vertical component. Detections are marked by the red and yellow circles. The first vertical line (green) corresponds to the picked P-wave arrival and the next two red lines delimit the triggering window.

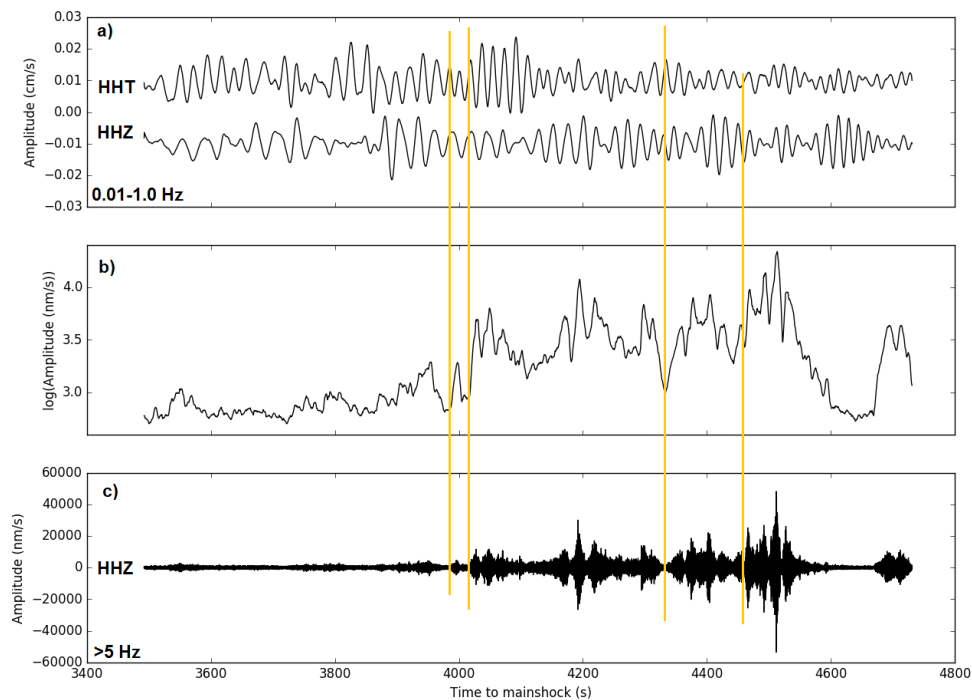


Figure 6.8: Surface waves from mainshock **L** recorded at station CVFG4. a) Transverse (top) and vertical (bottom) 0.01-1.0 band-pass filtered components; b) 3-component >5 Hz average envelope; c) 5 Hz high-pass filtered vertical component. Yellow lines mark the start of some of the high-frequency detected signals. These appear to start near a surface wave velocity maximum.

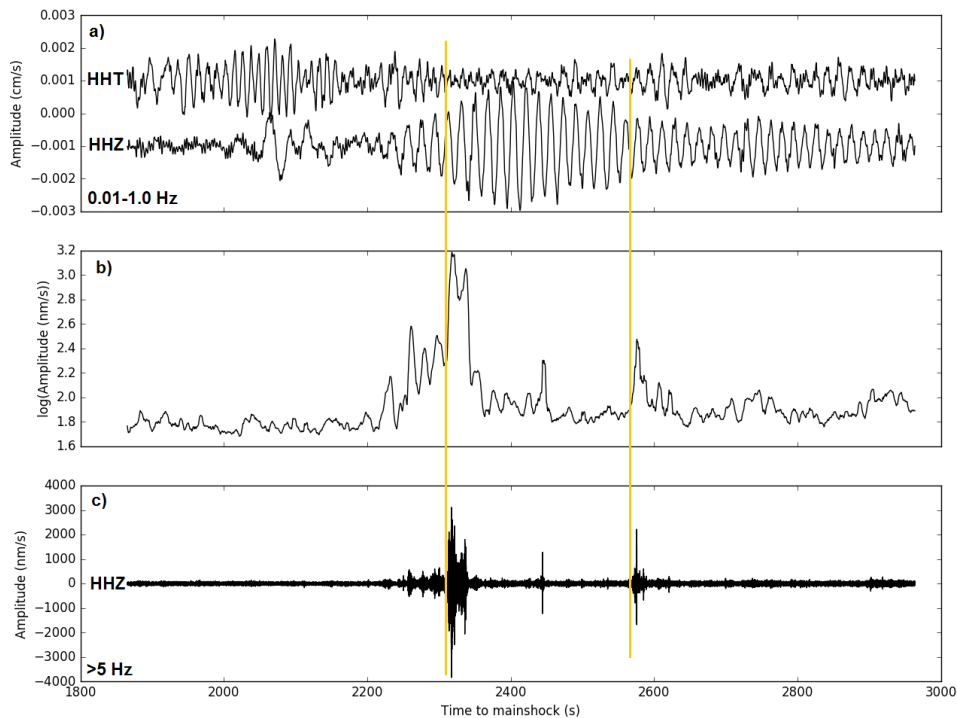


Figure 6.9: Surface waves from mainshock **O** recorded at station CVSN2. a) Transverse (top) and vertical (bottom) 0.01-1.0 band-pass filtered components; b) 3-component >5 Hz average envelope; c) 5 Hz high-pass filtered vertical component. Yellow lines mark the start of some of the high-frequency detected signals. These appear to start near a surface wave velocity maximum.

6.1.3 Mainshocks with epicenter in the Mid-Atlantic Ridge (C, D, E and F)

Mainshocks **C**, **D**, **E** and **F** are the analyzed mainshocks with the smaller epicentral distances to the reference stations, between 1557.22 to 2028.44 km, and all had an epicenter in the Mid-Atlantic Ridge.

In some stations with the $\beta \geq 2$, some of the detected signals are similar in the four mainshocks. Two clear bursts are identified in the filtered (>5 Hz) seismograms (figure 6.10), even in those with $\beta < 2$. The first burst has an impulsive onset and is registered at the a similar time as the arrival of the S-wave at the start of the triggering window and the second burst is recorded after the passage of the surface waves. Comparing with the theoretical arrival times for all seismic phases the first burst can correspond to the higher frequencies of the S-wave or a converted phase, as seen in figure 6.10. Without this detection the β -value does not indicate a significant increase in high-frequency signals. This comparison was made using the *ObsPy taup* package with the *iasp91* model [Kennett and Engdahl, 1991]. For the second burst a localization was attempted for each mainshock. A localization could not be calculated. Using the distance of the stations to the epicenter (r) and the determined arrival times (t) the data was fitted to a linear function $r = vt$, where v is the fitting parameter and corresponds to the average propagation speed, with nonlinear least-squares Marquardt-Levenberg algorithm (example for the **E** mainshock in figure 6.11). Results are in table 6.6. Although the reduced χ^2 values indicate a poor fit an average speed of about 1500 m/s is obtained for all the cases which is the approximate propagation speed of the T wave. This second burst can therefore correspond to T waves that propagated through the SOFAR channel.

These cases were not considered cases of dynamic triggering.

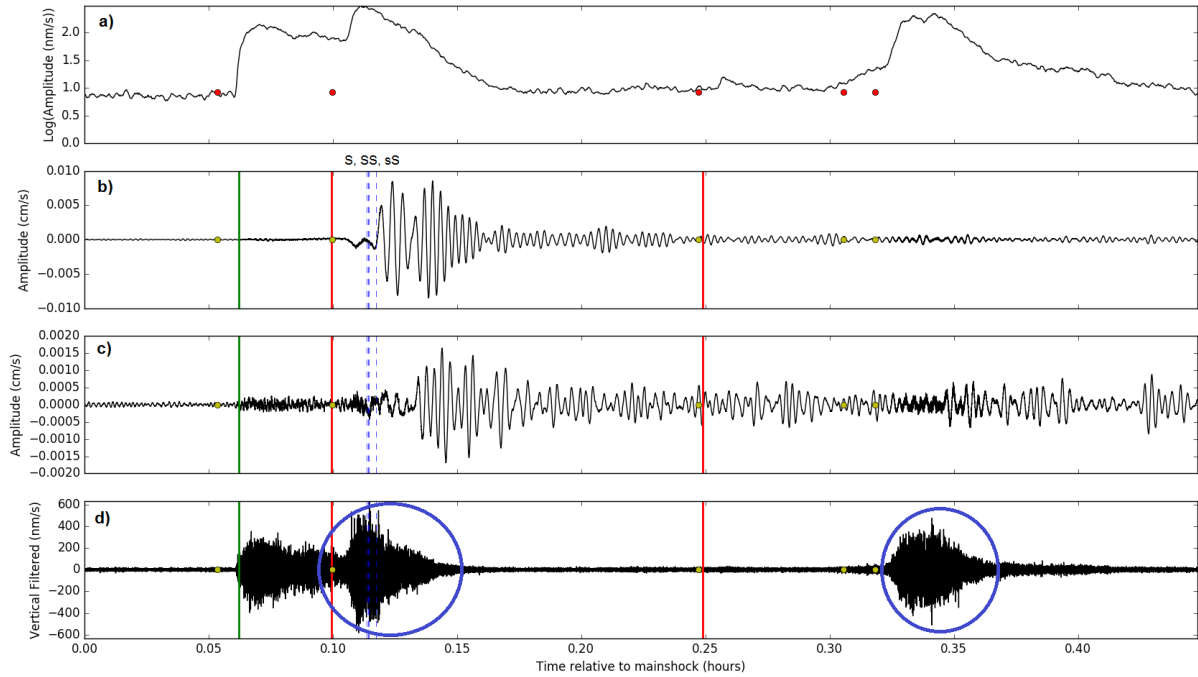


Figure 6.10: Two high-frequency bursts observed during the passage of mainshock **J** in MAIO station (blue circles). These bursts were observed in all the stations. The thin blue dashed lines mark the theoretical arrivals of the S, SS and sS waves, using the *iasp91* model. a) Three-component average envelope; b) Raw transverse component; c) Raw vertical component; d) 5 Hz high-pass filtered vertical component. Green vertical line corresponds to the manual picked P-wave and the red lines delimit the triggering window.

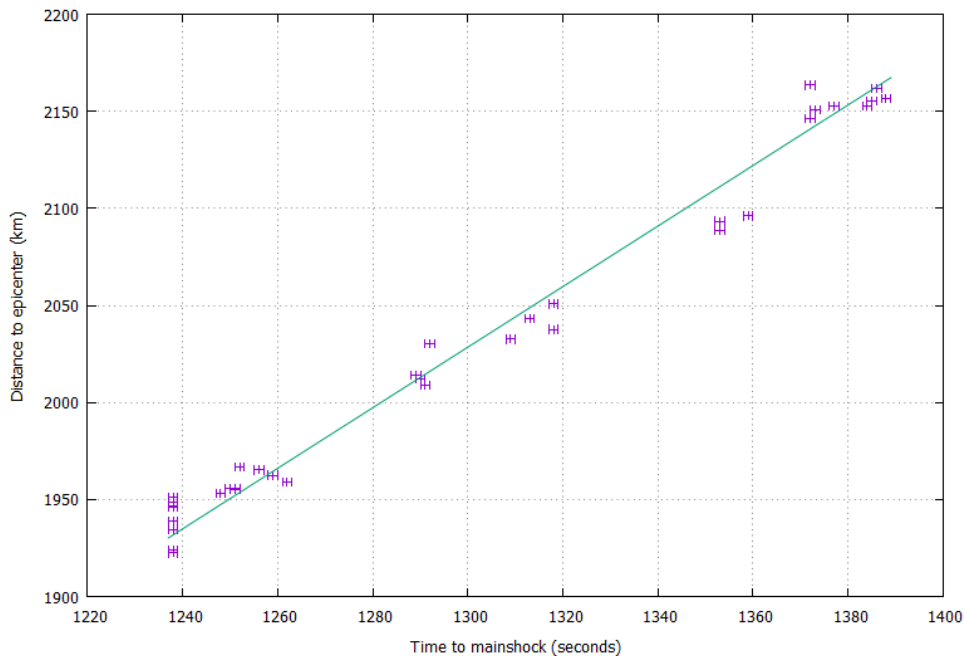


Figure 6.11: Nonlinear least-squares Marquardt-Levenberg fitting of $r = vt$ linear function (green line) to the distance of the stations to the epicenter (r) and the determined arrival times (t) of the observed second burst (in purple) for mainshock **E**. The fitting parameter corresponds to the average propagation speed with a result of 1.560 ± 0.002 km/s equal to the observed approximate propagation speed of the T-wave.

Station	β							
	2008/05/05	2008/05/06	2008/05/07	2008/05/08	2008/05/09	2008/05/10	2008/05/11	2008/05/12
CVBR1	17.985	20.523	16.712	8.737	9.472	6.545	0.89	7.349
CVFG1	21.733	23.584	18.224	17.037	14.325	7.949	3.293	2.765
CVFG2	20.443	19.974	15.087	21.074	11.252	8.256	1.43	5.434
CVFG3	14.848	17.067	10.118	7.972	9.931	2.74	-0.639	2.949
CVFG4	17.989	15.659	18.920	13.248	12.399	3.499	0.276	3.243
CVFG5	20.709	17.628	20.017	14.745	12.916	8.81	1.624	5.577
CVMA1	13.962	14.07	7.394	8.139	10.365	3.97	-1.199	2.475
CVMA3	9.946	3.371	11.704	9.811	5.04	2.903	0.567	2.132
CVMA4	15.953	16.810	10.097	16.051	9.665	3.943	1.577	0.817
CVST2	19.234	15.859	11.691	10.845	8.979	4.314	3.154	2.893
CVST4	7.976	14.553	7.774	6.600	3.392	4.128	-0.302	0.231
CVST5	26.496	23.632	24.238	17.330	11.123	6.617	4.864	4.332
CVBV1	16.114	20.542	21.083	20.607	15.285	8.391	-0.308	5.098
CVBV2	17.493	17.069	15.003	13.272	11.384	4.847	0.713	1.478
CVBV4	21.660	18.178	17.473	16.078	12.945	6.469	0.040	-0.175
CVBV5	10.080	10.253	18.910	5.950	5.596	4.744	0.278	-0.430
CVBV6	10.034	10.382	10.446	6.739	5.322	7.803	0.575	-1.501
CVSA1	27.37	25.945	19.233	18.081	12.258	7.720	2.200	2.796
CVSA2	14.226	9.130		12.474	4.528	1.768	-1.070	1.664
CVSA3	18.408	20.932	18.246	15.086	12.552	7.488	1.074	2.991
CVSA4	25.009	13.940	15.688	17.008	8.090	7.516	1.243	2.838
CVSA5	15.018	8.055	9.403	5.479	6.868	5.518	1.530	-2.170
CVSA6	6.285	2.920	9.792	11.625	6.918	1.367	-1.260	-0.956
CVSL1	14.537	14.819	18.212	10.516	11.612	3.854	-1.412	-1.933
CVSL2	12.380	11.875	12.101	15.018	14.996	3.293	0.391	0.924
CVSL4	1.966	1.681	5.959	2.837	0.383	7.117	-0.321	-1.424
CVSN1	23.891	23.400	20.807	17.128	14.160	9.670	2.294	7.816
CVSN2	-0.465	-0.155	-0.433	-0.452	7.312	1.344	2.130	-0.982
CVSN3	21.333	17.706	11.829	11.630	8.773	4.660	0.943	1.164
CVSN4	4.529	7.386	3.260	5.857	6.552	3.567	-0.237	1.576
CVST1	24.049	22.538	21.046	17.638	12.375	5.831	1.382	3.724
CVSV1	-0.570	3.912	3.027	3.752	4.179	-0.493	2.033	0.107
CVSV2	7.919	7.535	5.859	5.263	1.935	2.688	0.316	1.275
CVSV3	17.555	17.631	15.206	17.826	13.298	8.358	1.642	2.429
CVSV4	18.384	17.622	14.680	6.853	8.038	7.544	0.893	1.304

Table 6.5: Determined β -values for the 7 days before mainshock **L** in the same time period of the passage of the surface waves, for all stations analyzed in this mainshock

6.1.4 The November 3rd, 2002, Mw7.9 Denali earthquake (Mainshock H)

The results for the Denali earthquake (mainshock **H**) have only one station with a significant increase in the high-frequency seismic energy, at station MLOS. This station located near Chã das Caldeiras in the Fogo Volcano caldera does not present the strong cultural noise identified in other stations.

The increase in the detected high-frequency bursts starts with the passage of the Rayleigh waves and appears to be sustained even after the surface wave train has ended (figures 6.4 and 6.12).

The station has a strong continuous noise in the lower frequencies up to 9-10 Hz. The triggered signals

Mainshock	v (km/s)	dof	χ^2/dof	RMS
E	1.560 + 0.002	34	138.502	11.769
I	1.550 + 0.030	33	29024.2	170.365
J	1.508 + 0.027	6	8148.8	90.270
K	1.513 + 0.026	5	5934.7	77.037

Table 6.6: Results of the fitting to the the second bursts identified with a a nonlinear least-squares Marquardt-Levenberg algorithm

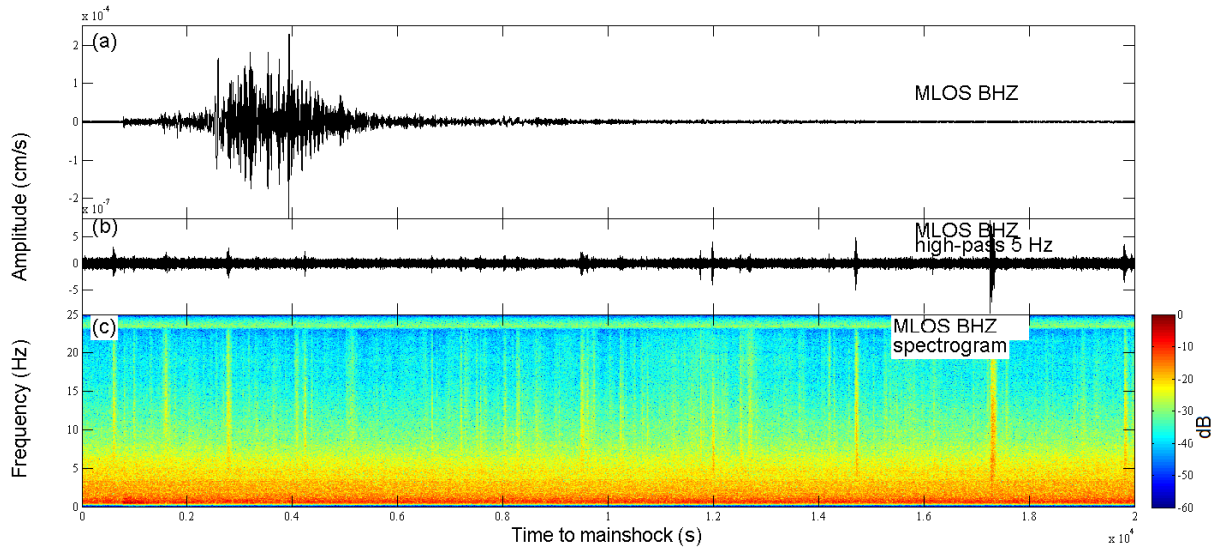


Figure 6.12: Mainshock **H** recorded in station MLOS. a) Raw vertical component; b) 5 Hz high-pass filtered vertical component; c) Vertical component spectrogram. High-frequency energy bursts are detected during the passage of the surface waves and similar signals occur after the surface wave train end. This result does not appear to be affected by the strong cultural noise.

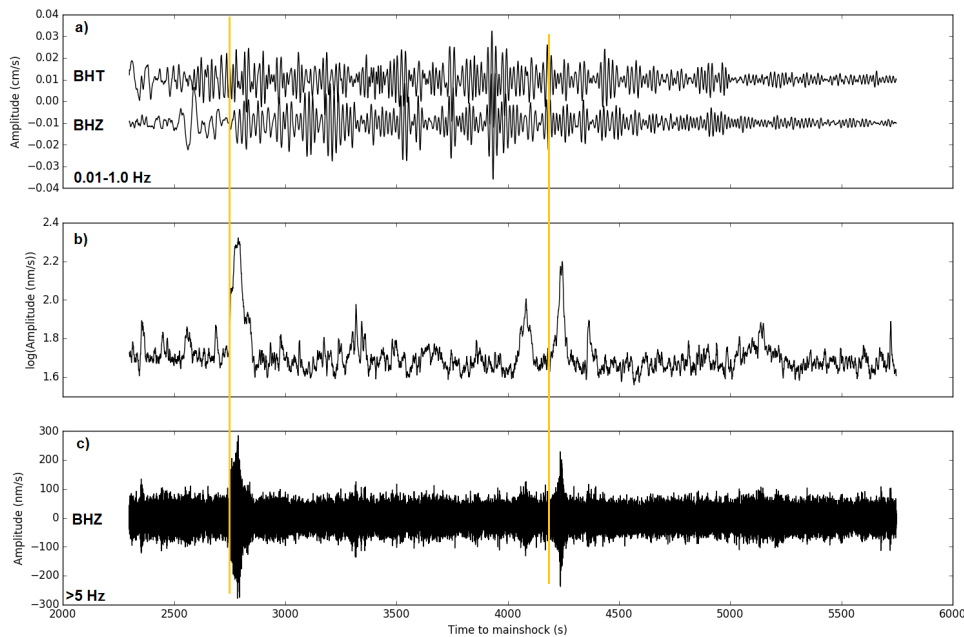


Figure 6.13: Surface waves from mainshock **H** recorded at station MLOS. a) Transverse (top) and vertical (bottom) 0.01-1.0 band-pass components; b) 3-component >5 Hz average envelope; c) 5 Hz high-pass filtered vertical component. Yellow lines mark the start of some of the high-frequency detected signals. These appear to start near a surface wave velocity maximum.

are mostly clearly observed in the frequencies >10 Hz. These high frequency bands are in the band of the observed cultural noise and the signals detected during the passage of the May 12, 2008, Mw7.9 Eastern Sichuan and the June 30, 2008, Mw7.0 South Sandwich Islands Region earthquakes surface waves. The bursts have emergent onsets and durations that go from 5 seconds up to more than one minute and appear to start before a velocity maximum is reached (figure 6.13), same as observed for mainshocks **L** and **O**.

6.2 Discussion

The studied region presents strong daily cultural noise that could affect the results.

Only one case of clear dynamic triggering was identified in only one station in Fogo island during the passage of the November 3rd, 2002, Mw7.9 Denali earthquake and evidences of delayed triggering are also observed. The triggered high-frequency energy bursts frequency band is in the frequency band of the observed cultural noise.

The increased activity observed during the passage of the May 12th, 2008, Mw7.9 Eastern Sichuan and the June 30th, 2008, Mw7.0 South Sandwich Islands Region earthquakes cannot be considered clear cases of dynamic triggering as the increase occurs in the period of the increase in cultural noise and is detected also in the days previous to the mainshock. Other results can also be misleading since the strong culture noise can be hiding an increase in activity due to triggered activity.

A more detailed study would be necessary to locate the detected signals and clearly link their origin to dynamic triggering.

In the analysis of the mainshocks with the smaller epicentral distances to the reference stations the results also seem to be affected by the higher frequencies of the S-wave or converted seismic phases that are detected by the automatic algorithm.

Chapter 7

Mozambique

In Mozambique 4 mainshocks were selected and analyzed, presented in table 7.1 and figure 7.1. Event B is an aftershock of event A.

7.1 Results

After running the automatic detection STA/LTA algorithm with both the windows for detecting short and long duration high-frequency energy bursts the results for the long duration were chosen. Analyzing the detected signals, they had in its majority a duration longer than 2 seconds and up to minutes.

The cases for which the calculated β -values show a significant increase or decrease of high-frequency (>5 Hz) energy bursts ($|\beta| \geq 2$) can be seen in table 7.2. The full results are in appendix B.

The results with $\beta \geq 2$ detected in mainshocks **A** and **B** are due to instrumental problems. The stations appear to be clipped during the passage of the surface waves which is clearly visible in image 7.2. Clipping occurs when the ground motion exceeds the amplitude range that the instruments can record or, what appears to occur in this case, when the mass that records the movement is not correctly centered limiting the correctly recorded amplitudes by the seismometer.

In various stations analyzed for mainshocks **C** and **D**, a high-frequency noise is observable before and after the arrival of the seismic waves, as can be seen in figures 7.8 and 7.5. In some stations, this noise is present in the entire period of analysis. The noise seems to have frequencies ≥ 10 Hz in the stations located in the border with South Africa and in the northern stations the noise has a larger frequency band being stronger for frequencies > 5 Hz.

Attributed identification	Mainshock (UTC)	Longitude	Latitude	Depth (km)	Magnitude (Mw)	Distance (km)	Estimated σ (kPa)	Analyzed Stations
A	2012/04/11 08:38:36.72	93.063°	2.327°	20.0	8.6	6947.37	13.068	13
B	2012/04/11 10:43:10.85	92.463°	0.802°	25.1	8.2	6815.28	5.371	13
C	2013/04/16 10:44:20.18	61.996°	28.033°	80.0	7.7	6246.99	1.962	8
D	2013/02/06 01:12:25.83	165.114°	-10.799°	24.0	8.0	13611.77	1.075	11

Table 7.1: Events analyzed in Mozambique

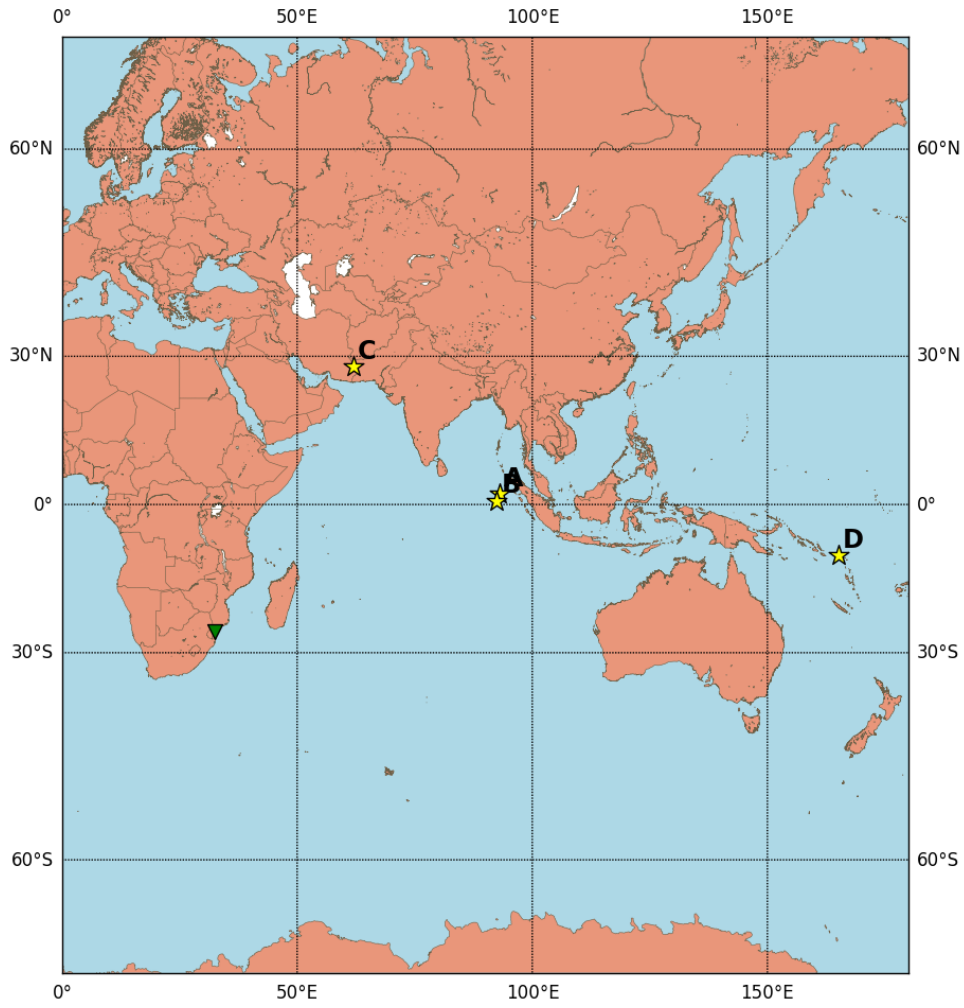


Figure 7.1: Map of mainshocks (table 7.1) analyzed in Mozambique (green triangle). The epicenters are marked by the yellow stars. Mainshocks have $M_w \geq 5.5$ and hypocentral depths ≤ 100 .

Station	Mainshock			
	A	B	C	D
MSGR				2.322
A0302		2.801		
A0805	-3.201	-2.088		
3434	4.865	2.165		
3901	2.252			
3A16	2.776			2.327

Table 7.2: Cases with $|\beta| \geq 2$ in Mozambique, using a 5 Hz high-pass filter

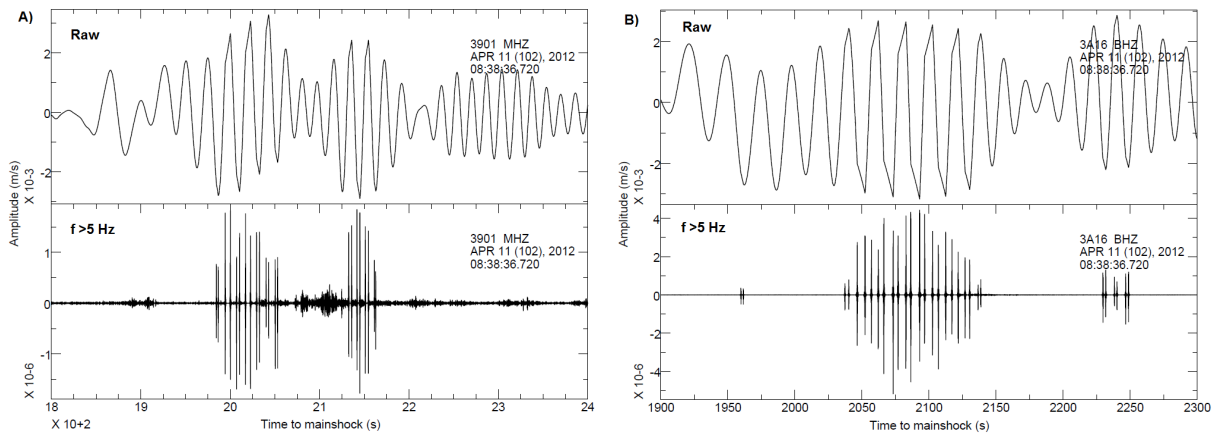


Figure 7.2: Clipped records of the vertical components during the passage of the Rayleigh waves of mainshock A in stations 3901 (A) and 3A16 (B). In high-passed >5 Hz seismograms several impulsive bursts followed by periods of absence of movement are recorded.

Station	Mainshock	
	C	D
A0282		2.002198
A0293		2.182386
A0302		2.034595
A1030		2.180713
3A16	2.941766	

Table 7.3: Cases with $|\beta| \geq 2$ in Mozambique for mainshocks C and D, using a 3-5 Hz band-pass filter

The signals were therefore filtered with a 3-5 Hz band-pass filter and the detection algorithm was rerun. Results with $|\beta| \geq 2$ are in table 7.3.

7.1.1 February 6th, 2013 Mw8.0 Solomon islands earthquake (mainshock D)

For mainshock D, in 4 stations an increase in high-frequency energy bursts is detected. Figure 7.3 shows the location of the stations that recorded the significant increase. The bursts are triggered during the passage of the Love waves and appear to stop short after the surface wave train. An example of the detection done for station A0302 can be seen in figure 7.4 and the respective spectrogram in figures 7.5 and 7.6. The possible triggered signals are in its majority tremor-like with emergent onsets and multiple peaks with a duration of 2 to 20 seconds and peak amplitudes in the orders of 10^1 and 10^2 nm/s. Some lower amplitude signals with impulsive onsets were also identified. No coherent signals were detected in the more than two stations. The detected signals appear to start near a velocity maximum (figure 7.7).

7.1.2 April 16th, 2013 Mw7.7 Saravan earthquake (mainshock C)

Station 3A16 records an increase during the passage of the seismic waves of mainshock C (figure 7.8). The detected signals are impulsive and start before the arrival of the Love wave and continue after the passage of the seismic waves. The signals have impulsive onsets and appear to have two distinct phases, with durations longer than 1 minute and peak amplitudes in the orders of the 10^2 nm/s. The detected signals are also observable in station 3901, although this station does not record a significant increase in high-frequency energy bursts.

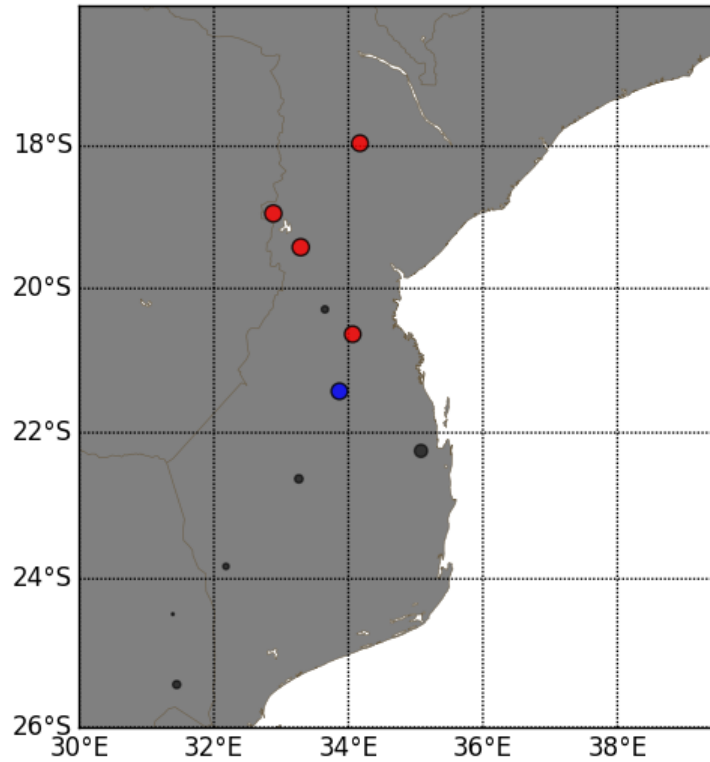


Figure 7.3: A significant increase in high-frequency activity is recorded in 4 stations in the northern part of the study area in Mozambique (Red circles).

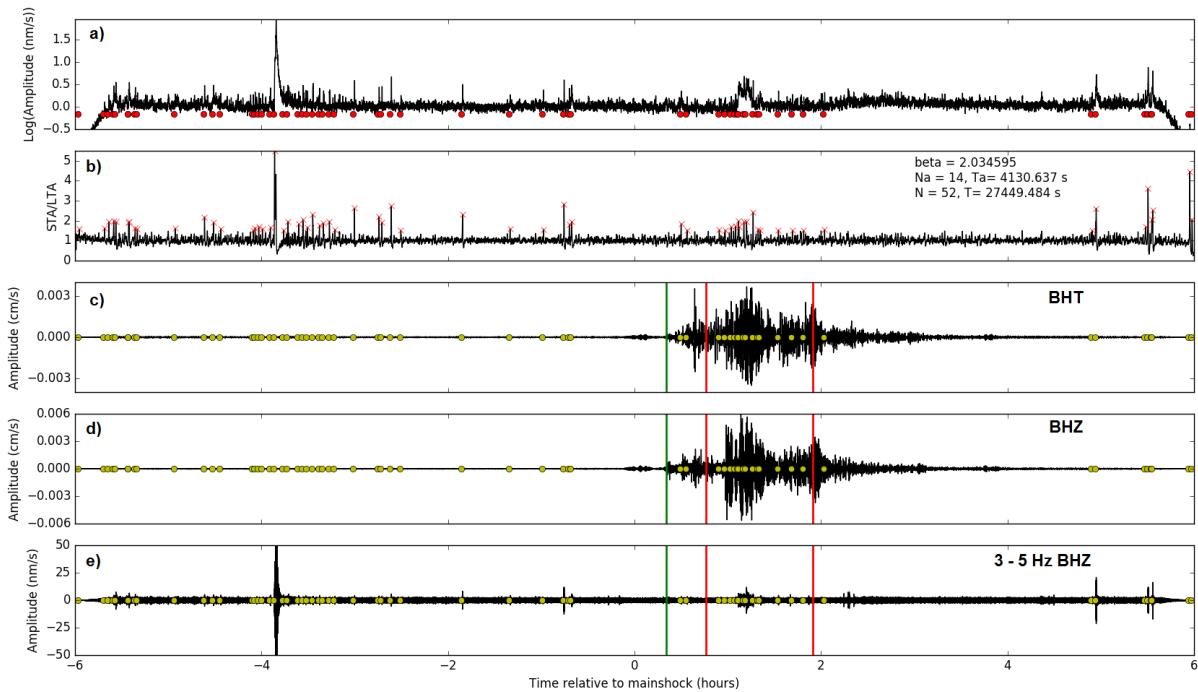


Figure 7.4: Data analyzed from station A0302 for mainshock **D**. a) Three-component average envelope; b) STA/LTA ratio; c) Raw transverse component; d) Raw vertical component; e) 5 Hz high-pass filtered vertical component. Green line marks the manual picked P-wave arrival; Red lines delimit the triggering window. An increase in detected high-frequency signals starts with the arrival of the Love wave.

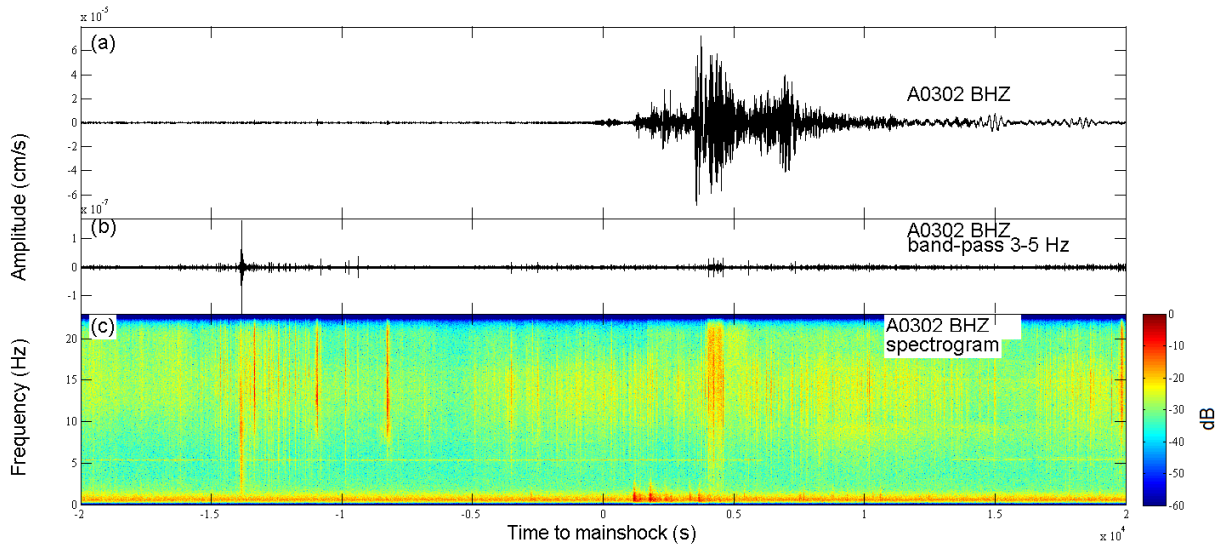


Figure 7.5: Mainshock **D** recorded in station A0302. a) Raw vertical component; b) 5 Hz high-pass filtered vertical component; c) Vertical component spectrogram. An increase in high-frequency energy bursts with a tremor-like signal is detected during the passage of the surface waves.

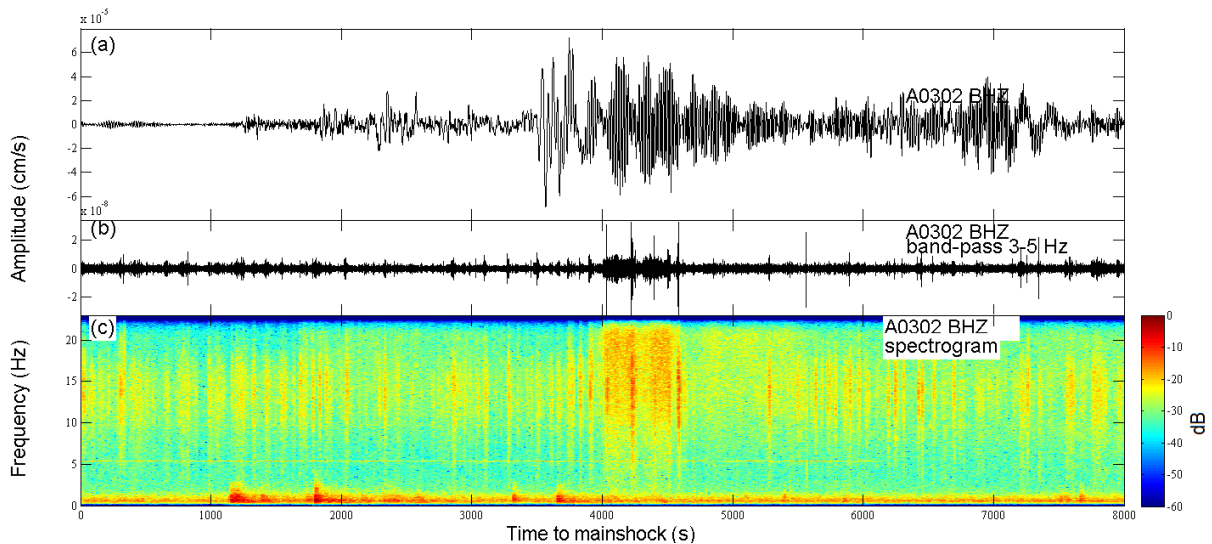


Figure 7.6: Zoom of figure 7.5, from the mainshock origin time to the end of the surface train. a) Raw vertical component; b) 5 Hz high-pass filtered vertical component; c) Vertical component spectrogram.

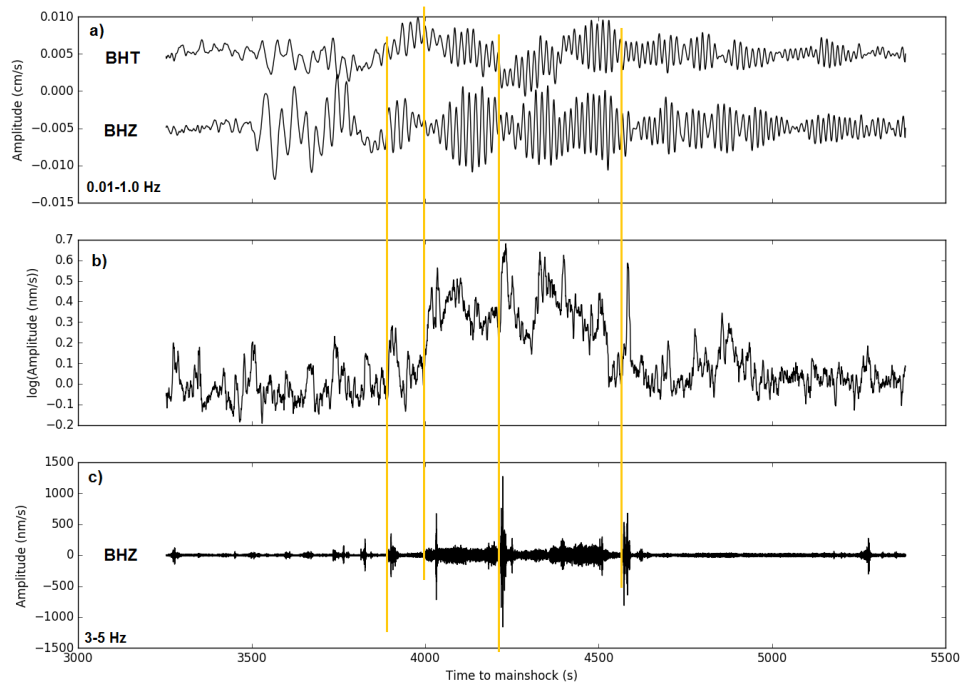


Figure 7.7: Surface waves from mainshock **D** recorded at station A0302. a) Transverse (top) and vertical (bottom) 0.01-1.0 band-pass filtered components; b) 3-component >5 Hz average envelope; c) 3-5 Hz band-pass filtered vertical component. Yellow lines mark the start of some of the high-frequency detected signals. These appear to start near a surface wave velocity maximum.

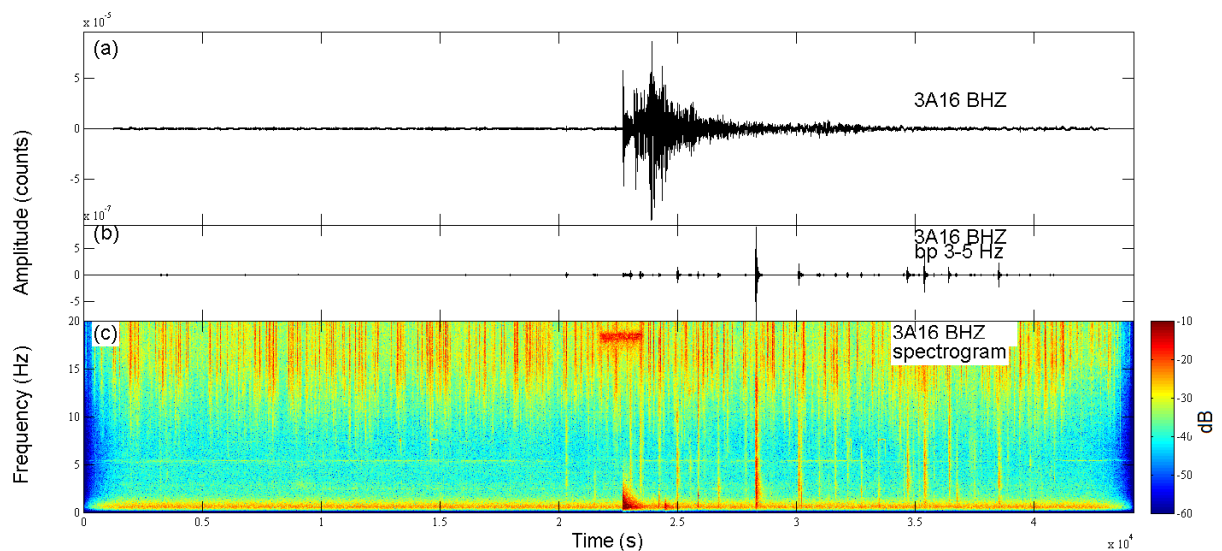


Figure 7.8: Data analyzed for mainshock **D** recorded in station 3A16. a) Raw vertical component; b) 5 Hz high-pass filtered vertical component; c) Vertical component spectrogram. High-frequency noise with frequencies higher than 10 Hz is present in the records. High-frequency energy bursts with a larger frequency band than the noise bursts are detected during the passage of the seismic waves.

7.2 Discussion

During the passage of the seismic waves of two of the studied mainshocks there is a statistically significant increase in high-frequency energy signals.

The February 6th, 2013 Mw8.0 Solomon islands earthquake surface waves appear to trigger high-frequency energy bursts in stations A0282, A0293, A0302 and A1030. These stations were deployed in the region of known active structures in Mozambique. The Rayleigh waves can be interacting with active structures in the region. Study of additional mainshocks would be necessary to understand if the increase in activity is recurrent in this region and the detection of coherent signals would be important to understand if the activity has its origin in any of the known active structures.

The analysis made for the April 16th, 2013 Mw7.7 Saravan earthquake (mainshock C) indicates a statistically significant increase in high-frequency energy bursts in station 3A16. This station was deployed in the Kapvaal Craton near the Lebombo monocline, an area not known to have active structures nearby. The detected signals start before the surface wave train. Further analysis would be necessary to understand if these are triggered by dynamic stresses of the seismic waves or they have another origin and just coincide with the passage of the seismic waves.

Chapter 8

Mid-Atlantic Ocean Ridge

8.1 Lucky Strike volcano

Twelve mainshocks were selected and analyzed for the Lucky Strike volcano deployments (table 8.1, figure 8.1), mainshock L is an aftershock of mainshock C. In these data the observation of the arrival of the P and S waves was not possible in the short period OBSs, even by filtering the data, and the background seismicity was calculated considering the theoretical arrival of the P-wave with the *iasp91* model.

8.1.1 Data problems

As described in section 4.3, data has periodic abrupt jumps and these had to be removed to perform the deconvolution in the removal of the instrument response. Data was cut around these jumps and then was removed the instrument response. The gaps left by the cutting were then filled with an interpolation. However the envelopes had lower values in these periods that resulted in STA/LTA ratios up to 100 that resulted in 1 to 3 detections in these periods (this can be seen in figures 8.2 and 8.3).

This affected the calculation of the background seismicity in all stations, except for station C7.

Detections in the triggering window were also affected in station D3 for mainshock C, station C1 for mainshock K, station D2 for mainshock L and in all stations analyzed for mainshock G.

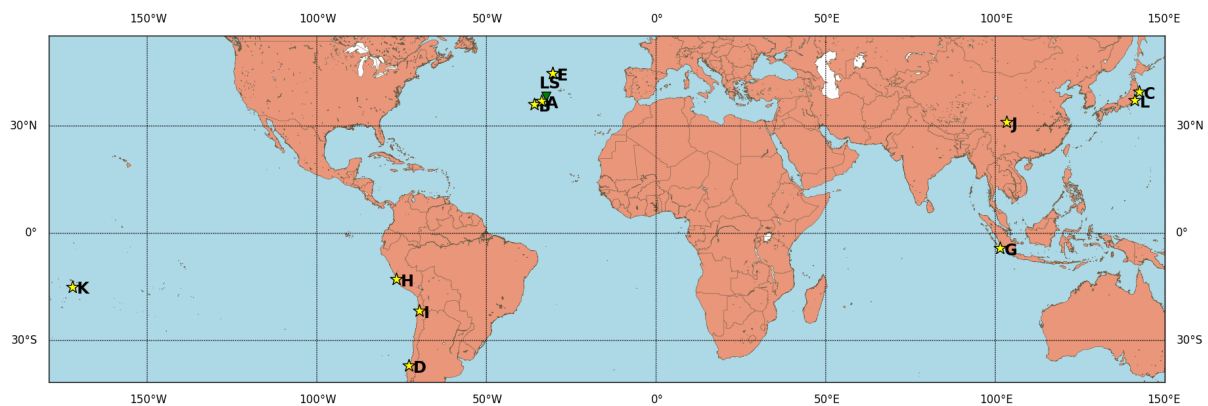


Figure 8.1: Map of mainshocks (table 8.1) analyzed in the Lucky Strike volcano (LS - green triangle). The epicenters are marked by the yellow stars. Mainshocks have $M_w \geq 5.5$ and hypocentral depths ≤ 100 .

Attributed identification	Mainshock (UTC)	Longitude	Latitude	Depth (km)	Magnitude (Mw)	Distance (km)	Estimated σ (kPa)	Analyzed Stations
A	2009/11/04 18:41:43.10	-33.878°	36.155°	2.0	5.9	190.02	61.001	5
B	2010/05/25 10:09:05.78	-35.924°	35.336°	10.0	6.3	392.06	52.430	4
C	2011/03/11 05:46:24.12	142.373°	38.297°	29.0	9.0	11633.48	13.949	5
D	2010/02/27 06:34:11.53	-72.898°	-36.122°	22.9	8.8	9137.82	13.141	5
E	2008/05/24 04:58:18.87	-30.515°	42.386°	10.0	5.5	585.75	6.526	6
F	2009/12/17 14:55:36.29	-30.565°	42.447°	4.0	5.5	591.20	6.449	5
G	2007/09/12 11:10:26.83	101.367°	-4.438°	34.0	8.5	14069.76	3.217	6
H	2007/08/15 23:40:57.89	-76.603°	-13.386°	39.0	8.0	7270.38	3.044	6
I	2007/11/14 15:40:50.53	-69.89°	-22.247°	40.0	7.7	7673.11	1.395	6
J	2008/05/12 06:28:01.57	103.322°	31.002°	19.0	7.9	11161.59	1.187	6
K	2009/09/29 17:48:10.99	-172.095°	-15.489°	18.0	8.1	15386.25	1.104	5
L	2011/03/11 06:15:40.28	141.111°	36.281°	42.6	7.9	11846.74	1.075	4

Table 8.1: Events analyzed in the Lucky Strike volcano

	Mainshock				
Station	E	G	H	I	J
LSo1	2.299	10.839			
LSo2			4.694		
LSo3		-2.731	-7.666	-2.585	
LSo4					3.464
LSo7		-2.723	-3.018		
LSo8				2.048	-2.990
Station	D	F	K		
LSc1	7.569				
LSc2	-4.832				
LSc3	-2.086		-4.645		
LSc4	-3.717		6.939		
LSc7		2.916			
Station	C	L			
LSd1	-2.734	-2.922			
LSd2	-2.619				
LSd3	-3.504	-7.868			
LSd4	-3.796	-2.329			

Table 8.2: Cases with $|\beta| \geq 2$ in the Lucky Strike volcano

8.1.2 Results

After a first run of the detection with the STA/LTA algorithm with the windows for short duration bursts and with the windows for longer duration bursts it was observed that the detected signals are emergent and impulsive with a duration of 1-2 seconds. So the results from the detection with the shorter STA/LTA windows were used. In some stations, emergent signals with longer durations up to more than a minute were also identified.

The cases for which the calculated β -values show a significant increase or decrease of high-frequency energy bursts ($|\beta| \geq 2$) can be seen in table 8.2. The determined β -values for all the stations and all mainshocks are in appendix C.

The determined β -values show significant increase of high-frequency energy bursts only in isolated stations for some mainshocks. None of these cases with $\beta \geq 2$ was classified as a case of clear triggering.

The increase in seismicity in station C1 for mainshock **D** and in station O2 for mainshock **H** starts before the arrival of the P-wave and continues after the passage of the surface waves, and the increase in seismicity does not seem to be associated with the passage of the surface waves (figure 8.2).

Data from station O4 for mainshock **J** and station C2 for mainshock **K** have instrumental problems, station C2 records are clipped.

As with the results in Cape Verde, the detections made for mainshocks at closer epicentral distances seem to include higher frequencies of the S-wave or converted phases. The increased seismicity from the β -values calculated for station O2 in mainshock **E** and station C7 in mainshock **F** is only statistically significant due to the detection of the signals that seem to be higher frequencies of the S-wave or converted phases and so no instant triggering is identified in these stations.

Station O1 records a swarm of activity that starts with the arrival of the surface waves and lasts until the end of the triggering window during the passage of the seismic waves of mainshock **G**, but since this is one of the stations with the data problems referred previously (section 8.1.1) the results can be a

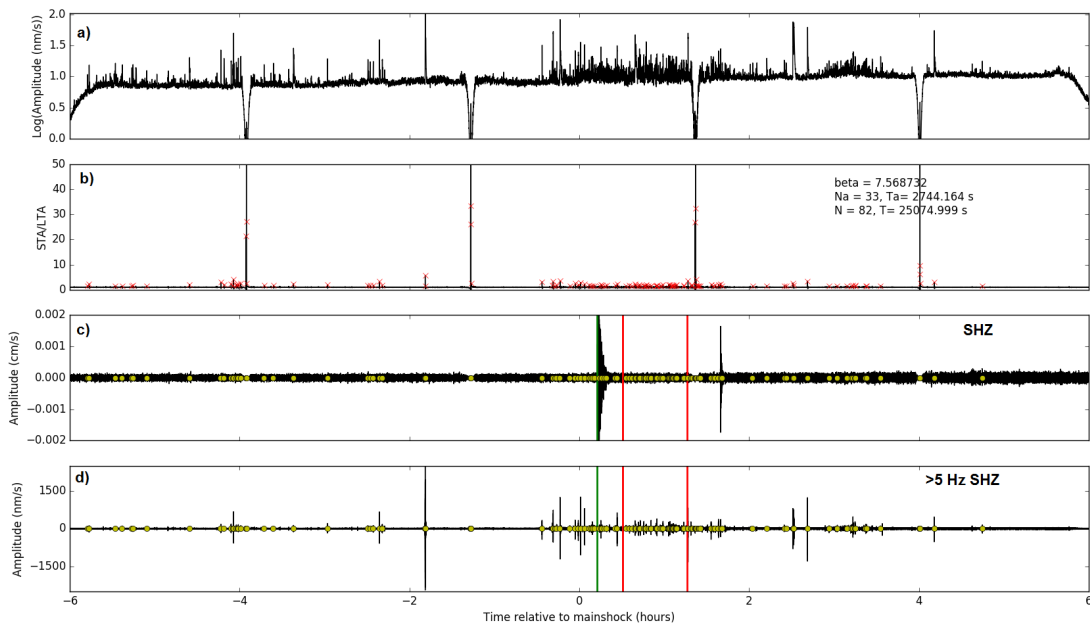


Figure 8.2: Data analyzed from station C1 for mainshock **D** in the Lucky Strike volcano. The increase in high-frequency seismic energy signals starts before the arrival of the seismic waves. a) Three-component average envelope; b) STA/LTA ratio; c) Raw vertical component; d) 5 Hz high-pass filtered vertical component. Green line marks the theoretical arrival of the P-wave with model *iasp91*; Red lines delimit the triggering window.

consequence of the instrumental problems and this is not considered a case of clear triggering.

In the cases with $\beta \leq -2$ after mainshocks **C** and **L** there is a decrease of high-frequency activity in the entire network that starts during the passage of the surface waves from mainshock **C** and **L** seismic waves (figure 8.3). In station D2 and D3 this decrease continues even after the passage of the surface waves. This decrease in detected signals can be related to the seismic waves, but it can also be a consequence of the instrumental problems since some of the stations have a deviation in data inside the triggering window.

8.1.3 Discussion

No clear evidences of dynamic triggering were identified in the Lucky Strike volcano. Although some cases of significant increase and decrease in high-frequency energy signals were identified the instrumental problems can be affecting these results and no conclusion can be made about them.

These results indicate that the Lucky Strike volcano was not susceptible to triggering by the stresses of the seismic waves of remote large earthquakes during the study period. The region can be in a low stress state and the dynamic stresses of the surface waves can be smaller than those necessary to trigger high-frequency activity.

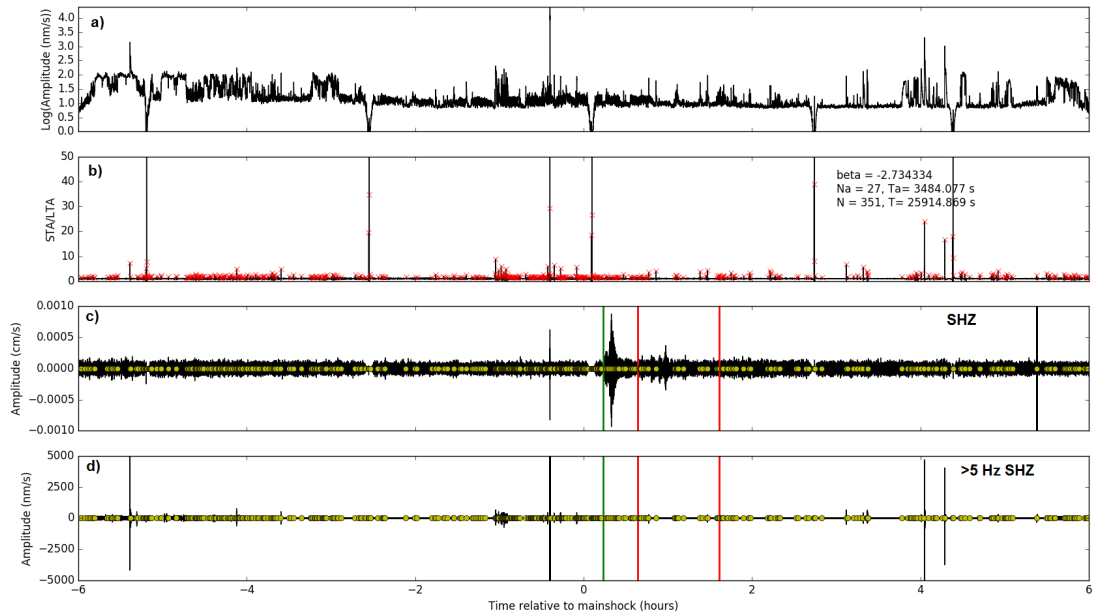


Figure 8.3: Data analyzed from station D1 for mainshock C in the Lucky Strike volcano. A significant decrease in high-frequency activity is detected during the passage of the surface waves. a) Three-component average envelope; b) STA/LTA ratio; c) Raw vertical component; d) 5 Hz high-pass filtered vertical component. Green line marks the theoretical arrival of the P-wave with model *iasp91*; Red lines delimit the triggering window.

8.2 Azores archipelago

In Azores 34 mainshocks were analyzed (tables 8.3 and 8.4, figure 8.4).

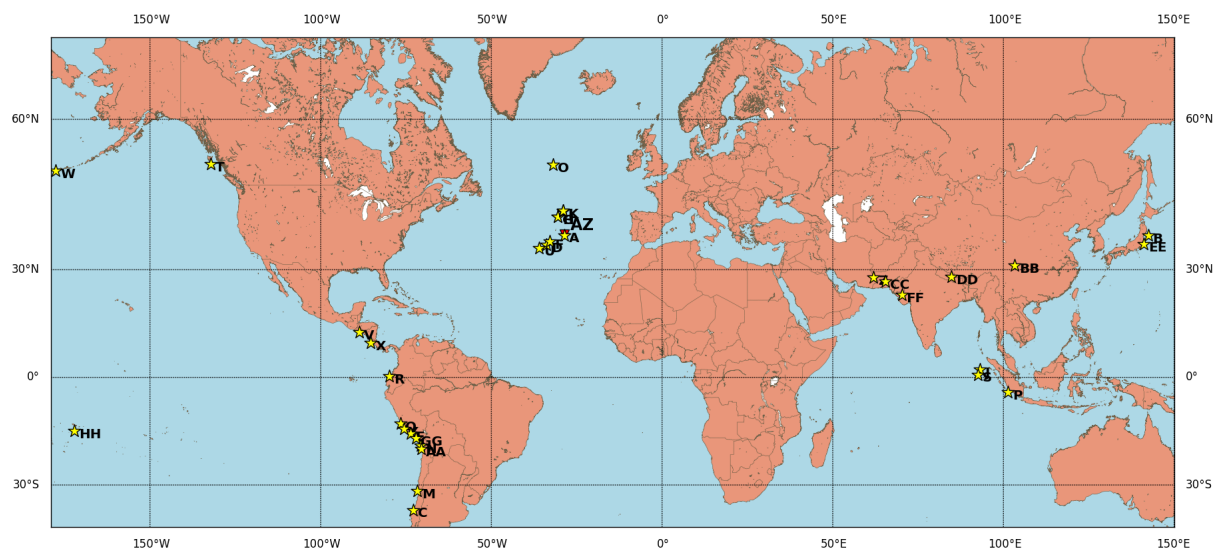


Figure 8.4: Map of mainshocks (table 8.3 and 8.4) analyzed in Azores (AZ - red triangle). The epicenters are marked by the yellow stars. Mainshocks have $M_w \geq 5.5$ and hypocentral depths ≤ 100 .

8.2.1 Results

In a quick analysis of the 5 Hz high-pass filtered data, before running the detection algorithm, bursts observed in the data during the passage of the surface waves have a duration from less than 1 second up

Attributed identification	Mainshock (UTC)	Longitude	Latitude	Depth (km)	Magnitude (Mw)	Distance (km)	Estimated σ (kPa)	Analyzed Stations
A	1997/06/27 04:39:52.72	-26.684	38.334	10.0	5.9	119.86	110.534	1
B	2011/03/11 05:46:24.12	142.373	38.297	29.0	9.0	11508.05	14.202	2
C	2010/02/27 06:34:11.53	-72.898	-36.122	22.9	8.8	9518.98	12.279	1
D	2009/11/04 18:41:43.10	-33.878	36.155	2.0	5.9	764.88	10.120	1
E	2001/06/23 20:33:14.13	-73.641	-16.265	33.0	8.4	7807.87	6.792	1
F	2010/08/13 07:58:48.76	-32.874	36.877	10.0	5.5	658.69	5.609	1
G	2009/12/17 14:55:36.29	-30.565	42.447	4.0	5.5	674.59	5.439	2
H	2008/05/24 04:58:18.87	-30.515	42.386	10.0	5.5	666.70	5.522	1
I	2011/08/31 12:17:27.01	-28.902	43.589	10.0	5.5	707.17	5.118	1
J	2012/04/11 08:38:36.72	93.063	2.327	20	8.6	12315.07	5.052	1
K	1998/06/03 15:47:07.90	-29.02	43.679	10.0	5.5	720.29	4.998	1
L	2003/08/27 14:40:42.15	-28.922	43.741	10.0	5.5	723.18	4.972	1
M	2015/09/16 22:54:32.86	-71.6744	-31.5729	22.4	8.3	9042.53	4.228	2
N	2014/04/01 23:46:47.26	-70.7691	-19.6097	25.0	8.2	7914.95	4.190	2
O	2015/02/13 18:59:12.23	-31.9016	52.6487	16.7	7.1	1727.78	4.163	2
P	2007/09/12 11:10:26.83	101.367	-4.438	34.0	8.5	13500.69	3.445	1
Q	2007/08/15 23:40:57.89	-76.603	-13.386	39.0	8.0	7768.40	2.727	1
R	2016/04/16 23:58:36.98	-79.9218	0.3819	20.6	7.8	6923.36	2.083	2

Table 8.3: 18 of the 34 events analyzed in the Azores archipelago.

Attributed identification	Mainshock (UTC)	Longitude	Latitude	Depth (km)	Magnitude (Mw)	Distance (km)	Estimated σ (kPa)	Analyzed Stations
S	2012/04/11 10:43:10.85	92.463	0.802	25.1	8.2	12377.00	1.995	1
T	2012/10/28 03:04:08.82	-132.101	52.788	14.0	7.8	7748.83	1.728	2
U	2010/05/25 10:09:05.78	-35.924	35.336	10.0	6.3	968.80	1.724	1
V	2001/01/13 17:33:32.38	-88.66	13.049	60.0	7.7	6775.59	1.715	1
W	1996/06/10 04:03:35.48	-177.632	51.564	33.0	7.9	9757.70	1.484	1
X	2012/09/05 14:42:07.80	-85.315	10.085	35.0	7.6	6680.63	1.395	2
Y	1996/11/12 16:59:44.03	-75.675	-14.993	33.0	7.7	7838.12	1.347	1
Z	2013/04/16 10:44:20.18	61.996	28.033	80.0	7.7	7963.09	1.312	2
AA	2014/04/03 02:43:13.11	-70.4931	-20.5709	22.4	7.7	7983.55	1.306	2
BB	2008/05/12 06:28:01.57	103.322	31.002	19.0	7.9	10737.28	1.266	1
CC	2013/09/24 11:29:47.97	65.5009	26.951	15.0	7.7	8316.90	1.220	2
DD	2015/04/25 06:11:25.95	84.7314	28.2305	8.2	7.8	9721.68	1.186	2
EE	2011/03/11 06:15:40.28	141.111	36.281	42.6	7.9	11707.97	1.096	1
FF	2001/01/26 03:16:40.50	70.232	23.419	16.0	7.7	8932.12	1.084	1
GG	2001/07/07 09:38:43.52	-72.077	-17.543	33.0	7.6	7815.77	1.075	1
HH	2009/09/29 17:48:10.99	-172.095	-15.489	18.0	8.1	15910.51	1.044	2

Table 8.4: 16 of the 34 events analyzed in the Azores archipelago

Mainshock	β	σ (kPa)
A	4.176	30.360
I	2.358	0.463
J	5.066	4.140
K	3.532	0.206
M	-2.797	3.189
Q	3.045	3.154
AA	-2.058	2.494
DD	2.689	0.446

center

Table 8.5: Cases with $|\beta| \geq 2$ in Azores and the respective dynamic stress determined by the record peak ground velocity with equation 5.1. Only CMLA station had significant variations.

to around 10 seconds. So the windows for detecting short duration bursts were used.

Cases with $|\beta| \geq 2$ are in table 8.5. The full results are presented in appendix D.

The ROSA station in São Jorge island did not have any case with $|\beta| \geq 2$.

In CMLA station during the passage of the seismic waves of 6 mainshocks was recorded a statistically significant increase in high-frequency energy activity, mainshocks **A**, **I**, **J**, **K**, **Q** and **DD** (table 8.5). Examples for mainshocks **A** and **J** can be seen in figures 8.8 and 8.5, respectively.

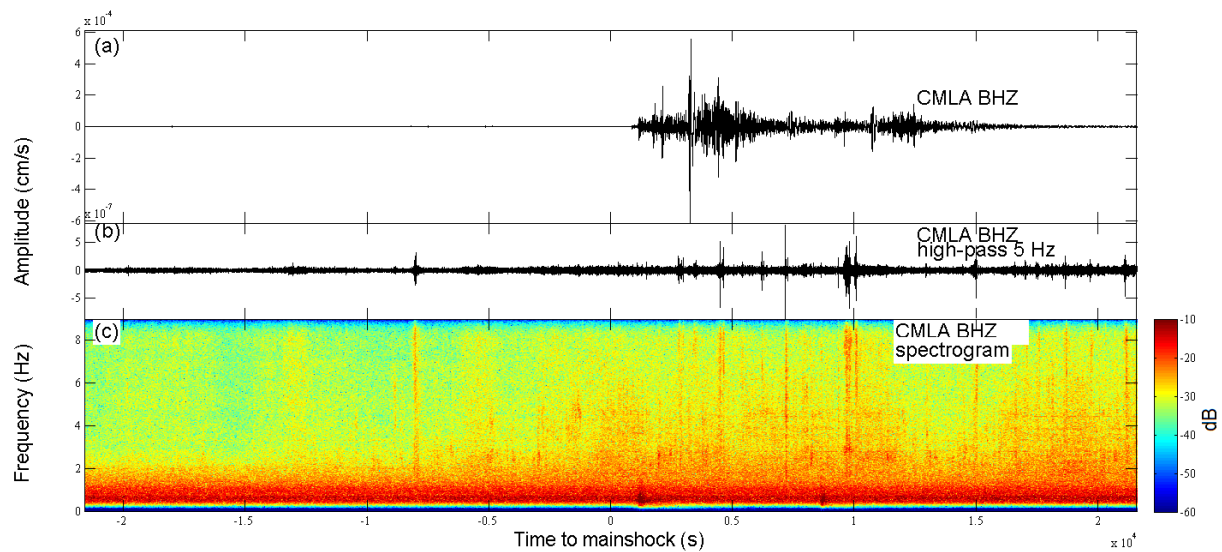


Figure 8.5: Mainshock **J** recorded in Azores archipelago in station CMLA. a) Raw vertical component; b) 5 Hz high-pass filtered vertical component; c) Vertical component spectrogram. An increase in high-frequency energy bursts is detected during the passage of the surface waves.

The case of mainshocks **I** and **K** are not considered cases of triggering as the increase in seismicity is due to only one detection of signals before the actual arrival of the surface waves. All the other cases appear to be clear cases of triggering.

β -values determined for **M** and **AA** indicate a significant decrease in activity. In the case of mainshock **M** this decrease appears to start before the arrival of the seismic waves. A clear decrease in detected signals is seen in the case of mainshock **AA** that is maintained after surface wave train (figure 8.6).

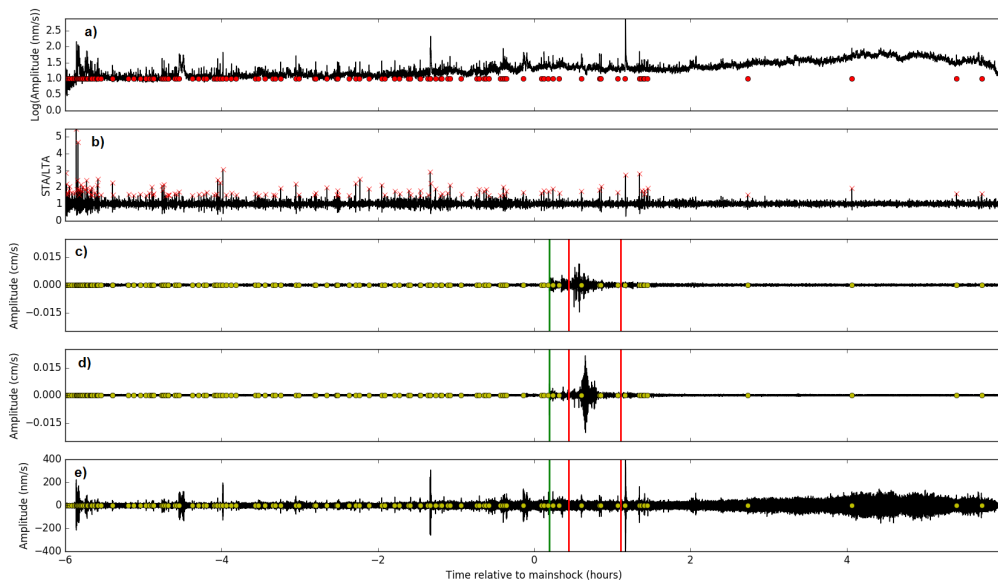


Figure 8.6: Mainshock **AA** recorded in Azores archipelago in station CMLA. A significant decrease in high-frequency activity appears to start with the passage of the seismic. a) Three-component >5 Hz average envelope; b) Raw transverse component; c) Raw vertical component; d) Raw transverse component; e) 5 Hz high-pass filtered vertical component. Detections are marked by the red and yellow circles. The first vertical line (green) corresponds to the picked P-wave arrival and the next two red lines delimit the triggering window.

Mainshock A

From the analysis of mainshock **A** it is not possible to understand if there is instant triggering as the mainshock seismic waves could not be completely filtered. The detections that determined the β -value correspond to the higher frequencies of the seismic waves but observing the data for the 6 hours after the mainshock it is clear that there is an increase in activity (figures 8.7 and 8.8). The detected signals have impulsive and emergent onsets and the majority of the impulsive signals appear to have two distinct phases and could be earthquakes as can be seen in figure 8.9.

This mainshock is the one with smaller epicentral distance. Observing the International Seismological Centre catalog for the location of the mainshock epicenter there is an increase in nearby activity in the next days (figure 8.10 A) due to the aftershocks. For the detected signals with two phases the possible P phase was manually picked in the vertical component and the possible S phase in the horizontal components. This allowed the measure of the time interval between the two phases. The mainshock has a time difference of 14.1502 seconds between the P and S wave arrivals. The 35 detected signals in the hours after the mainshock with two phases have an interval between the two phases in its majority around 14 seconds (figure 8.10 B). This is an indication that this events have its origin at a similar distance of the principal mainshock. The signals were therefore classified as aftershocks and not triggered signals.

Mainshocks J, Q and DD

During the passage of mainshocks **J**, **Q** and **DD** signals with emergent onsets are detected. Signals have various peaks and are tremor-like. The signals appear to be triggered by both the Love and the Rayleigh (figure 8.11) waves but a greater number of signals are detected during the passage of the Rayleigh waves.

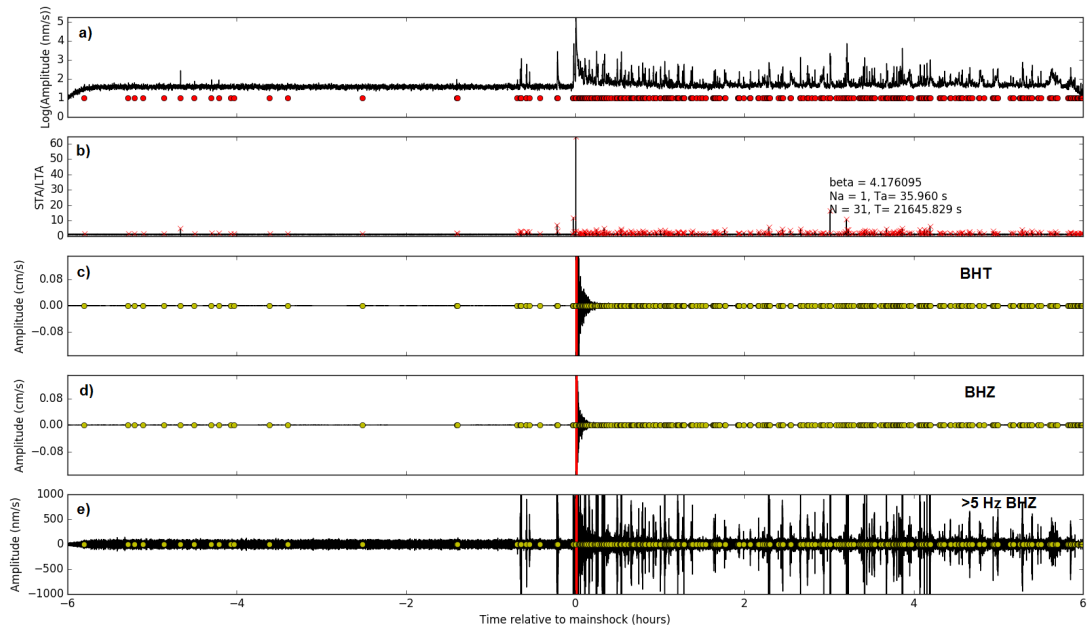


Figure 8.7: Data analyzed from station CMLA for mainshock **A** in Azores archipelago. A clear increase in activity is observed after the passage of the seismic waves. The calculated β is due to the detection of what appear to be the seismic waves higher frequencies, this could not be filtered. a) Three-component average envelope; b) STA/LTA ratio; c) Raw transverse component; d) Raw vertical component; e) 5 Hz high-pass filtered vertical component. Green line marks the theoretical arrival of the P-wave with model *iasp91*; Red lines delimit the triggering window.

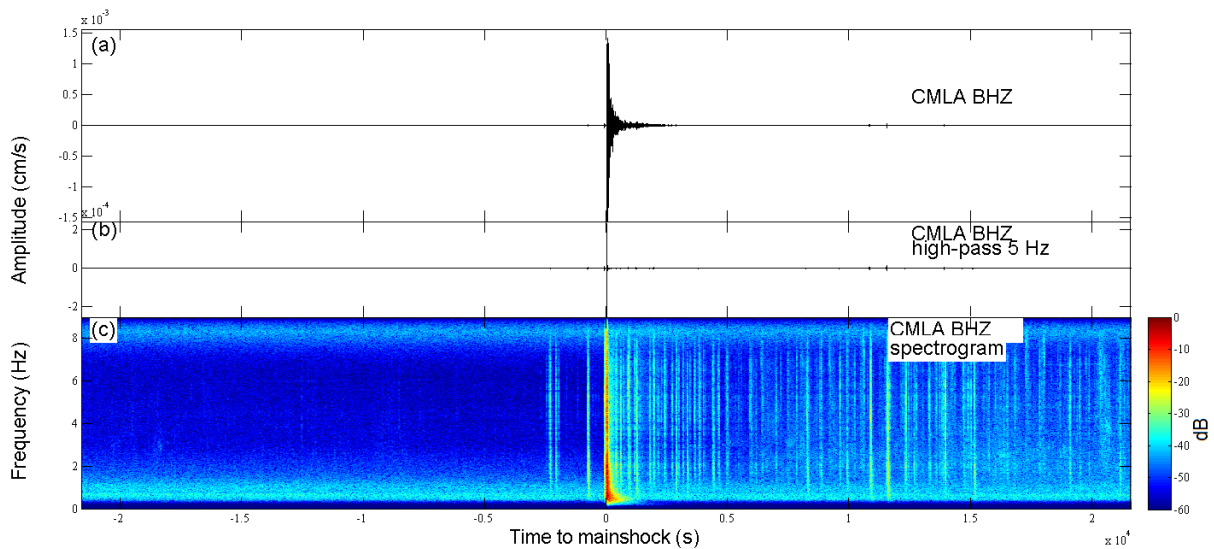


Figure 8.8: Mainshock **A** recorded in Azores archipelago in station CMLA. a) Raw vertical component; b) 5 Hz high-pass filtered vertical component; c) Vertical component spectrogram.

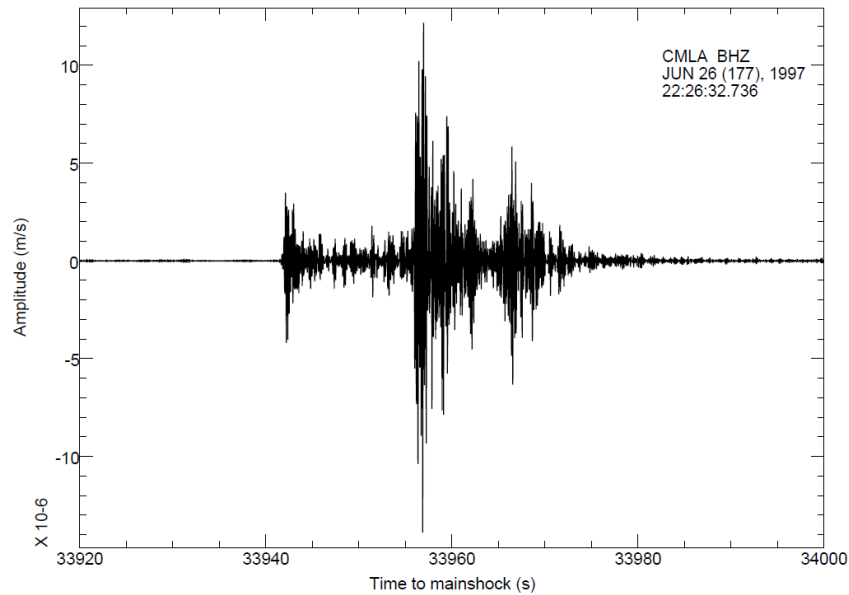


Figure 8.9: Signal detected after the passage of mainshock **A** surface waves in Azores archipelago. It has two impulsive phases.

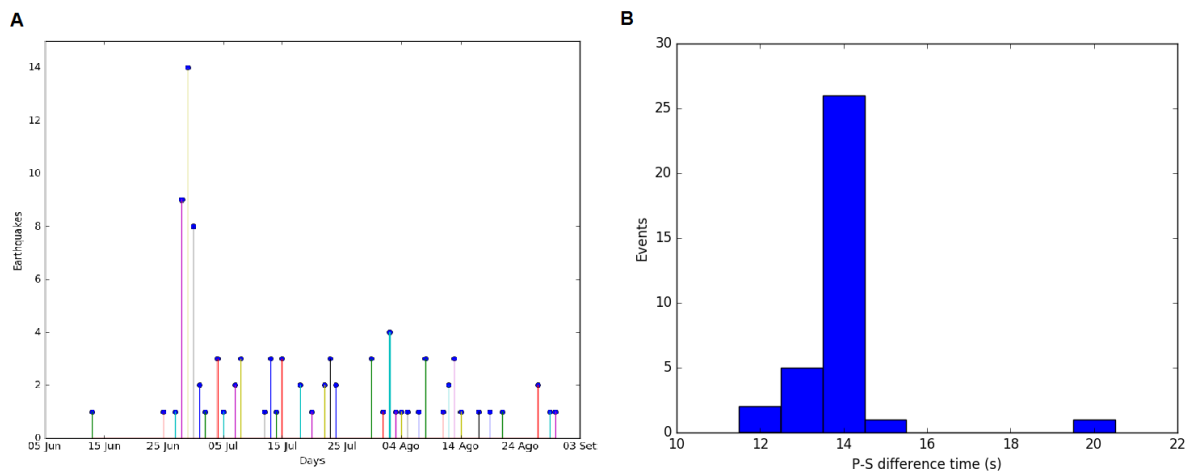


Figure 8.10: A) Stem plot with the events located close to mainshock **A** epicenter in Azores archipelago between 1st June and 31st August, 1997, from the International Seismological Centre catalog. An increase occurs in the day of the mainshock and the days after. B) Histogram with the determined intervals between P and S phases of the 35 impulsive signals detected after mainshock **A**.

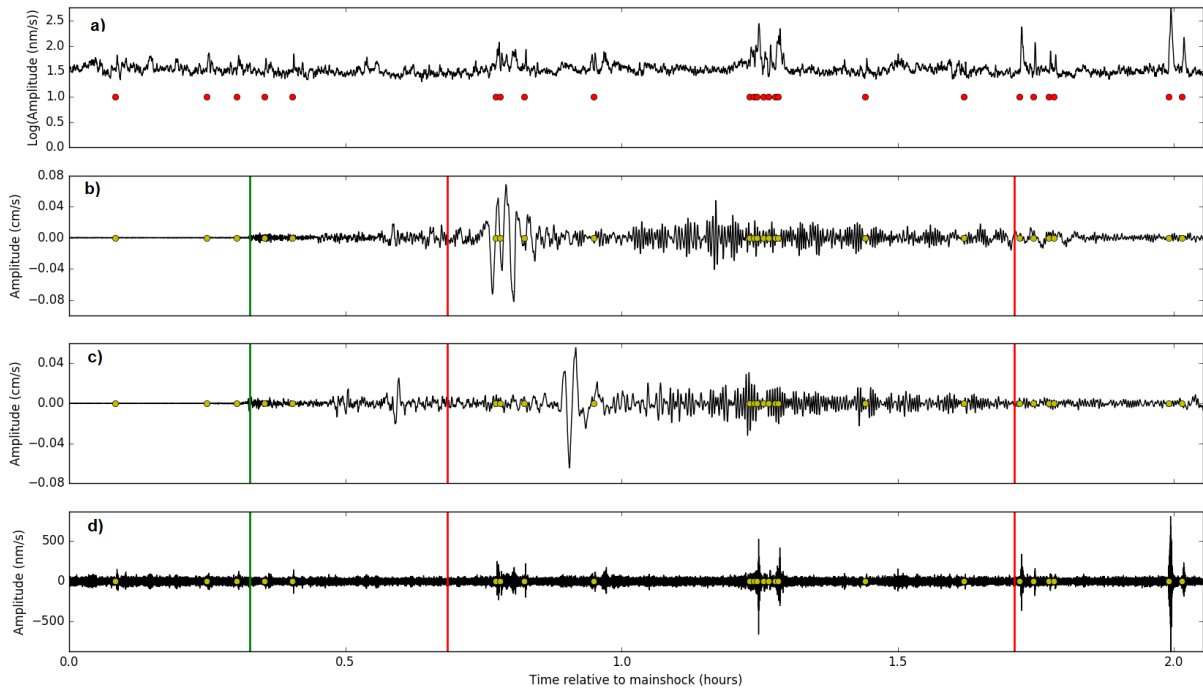


Figure 8.11: Mainshock **J** recorded in Azores archipelago in station CMLA. During the passage of the seismic waves two groups of high-frequency energy bursts were detected. One occurs with the arrival of the Love waves and the other during the passage of the Rayleigh waves. Signals have emergent onsets and are tremor-like. a) Three-component >5 Hz average envelope; b) Raw transverse component; c) Raw vertical component; d) 5 Hz high-pass filtered vertical component. Detections are marked by the red and yellow circles. The first vertical line (green) corresponds to the picked P-wave arrival and the next two red lines delimit the triggering window.

In figure 8.11 triggered tremor-like signals appear to be detected during the passage of the Love and the Rayleigh waves of mainshock **J**. These signals appear to start near velocity maximum (figure 8.12).

8.2.2 Discussion

Results from the analysis of the data for ROSA station in São Jorge indicate that the structures in the island do not respond to the dynamic stresses of distant earthquakes. This could be related to the fact that São Jorge seems to be in a seismic gap (section 3.3.1).

CMLA station in Chã de Macela near the Fogo volcano in the island of São Miguel appears to record various cases of remote triggering. Mainshocks **J**, **Q** and **DD** are cases where a clear significant increase occurs during the passage of the surface waves. Signals are tremor-like and could be volcanic tremor. The seismic waves could disturb the volcanic structures in the area leading to the increase of the high-frequency activity. Measuring the peak ground velocities recorded and calculating the peak dynamic stresses with equation 5.1, a clear relation between the peak dynamic stresses and the occurrence of triggering does not seem to exist (figure 8.13).

For mainshock **A** it is not possible to determine if instant triggering occurs since it was not possible to filter the seismic waves. Signals detected after the mainshock are aftershocks.

One apparent case of a decrease in high frequency activity with the arrival of the surface waves was also identified.

To clearly understand these results data from a larger network would be necessary to understand if the observed signals in the cases with clear increases in activity are also detected in other stations and

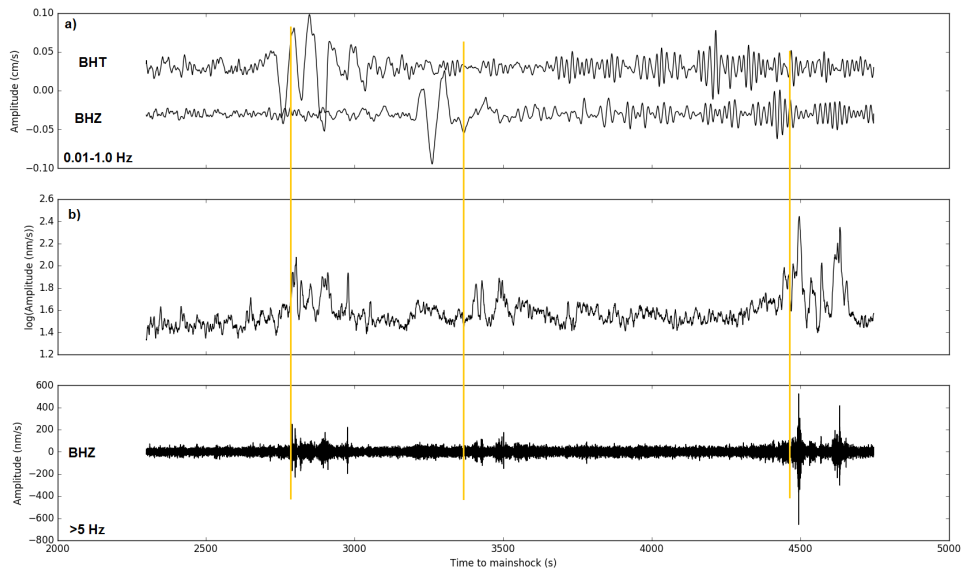


Figure 8.12: Surface waves from mainshock **J** recorded in Azores archipelago at station CMLA. a) Transverse (top) and vertical (bottom) 0.01-1.0 band-pass filtered components; b) 3-component >5 Hz average envelope; c) 3-5 Hz band-pass filtered vertical component. Yellow lines mark the start of some of the high-frequency detected signals. These appear to start near a surface wave velocity maximum.

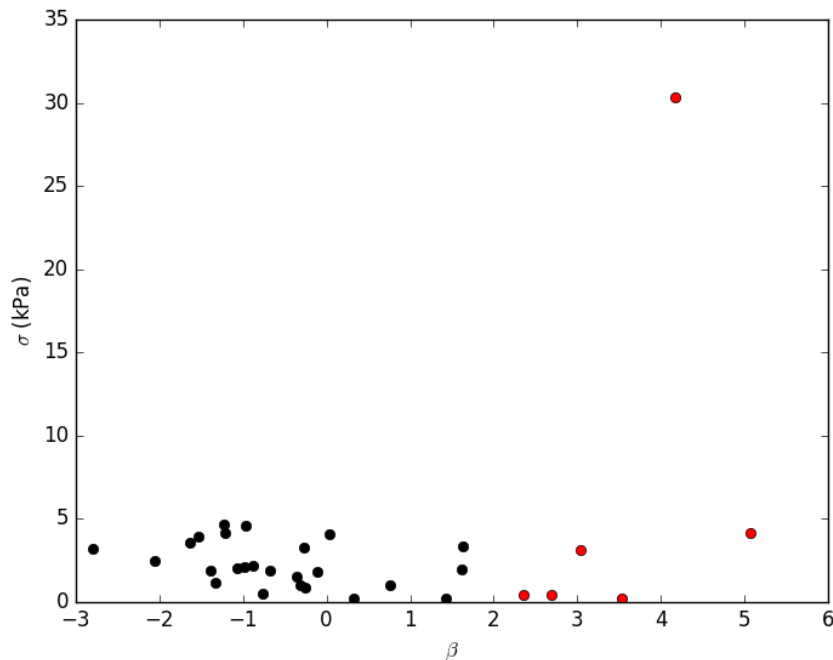


Figure 8.13: Plot of determined β -values vs calculated σ from the recorded peak ground velocities from equation 5.1. A clear relation between the two variables does not appear to exist.

possibly located them. This would allow to determine what structures are being activated by the dynamic stresses imposed during the passage of the surface waves.

Chapter 9

Conclusions

Using an automatic detection STA/LTA algorithm with β -statistics the variations of seismicity during the passage of large earthquakes seismic waves were assessed in four different areas. A total of data from 52 different mainshocks were analyzed and data from 88 different seismic stations were used in this study in 4 different study regions.

In the 4 regions of study 6 cases of possible positive dynamic triggering were detected. One positive case was detected in Cape Verde, 2 cases in Mozambique and 3 cases in Azores. The observed seismicity has in its majority emergent onsets and signals were not detected in more than two stations, which can be interpreted as local seismicity with low magnitudes. Determination of the sources of the observed signals was therefore not possible.

In Cape Verde, a strong cultural noise with diurnal variation was identified. Only one clear case of significant increase in high-frequency seismic energy bursts was identified in the Fogo island in the Fogo volcano during the passage of the 2002 Mw7.9 Denali earthquake. The triggered signals identified in this case had frequencies in the same band of the cultural noise and so this noise could be masking triggered signals. Other two cases of increased high-frequency energy bursts with the passage of the seismic waves in the southwestern and northwestern islands, islands with volcanic structures in the islands or in their vicinity, were identified but these occurred in the period were the increase in cultural noise starts. A method to determine the origin of the identified signals, triggered or noise, is necessary to better interpret the results in the Cape Verde archipelago.

The passage of the surface waves of the February 6th, 2013 Mw8.0 Solomon islands earthquake in Mozambique coincides with a clear significant increase in high-frequency seismic energy bursts in four stations near active tectonic structures in Mozambique. The possible triggered signals do not appear to be coherent between stations and therefore it was not possible to link the signals clearly to the active structures. One other case of increase in high-frequency energy bursts was identified during the passage of the April 16th, 2013 Mw7.7 Saravan earthquake but the increase appears to start before the arrival of the surface waves and no active structures have been identified in the region of the identified station.

Data from the Lucky Strike volcano in the Lucky Strike segment of the Mid-Atlantic Ridge does not show any clear evidence of triggered seismicity in the studied period. The active structures in the area can be in a low stress state and the dynamic stresses of the surface waves might not be enough to trigger activity. Results are also affected by the identified instrumental problems.

In the Azores, no evidence of dynamic triggering was found in the island of São Jorge, which could be related to the fact that the island is located on a known seismic gap. Chã de Macela, in São Miguel, near the Fogo volcano, appears to be a location of repeated triggering. In São Miguel three clear cases of increased high-frequency seismic energy bursts were identified. A clear relation between the occurrence

of increased high-frequency seismic energy bursts and dynamic stresses of the seismic waves does not appear to exist. As these results are recorded only at one station they are not strong evidences of dynamic triggered seismicity. A future study in the archipelago using data from more stations with better spatial coverage of the archipelago and specifically of São Miguel island would help understand if Azores is really an area where repeated triggering occurs and what are the main structures activated by the seismic waves.

In this study were also identified several cases with mainshocks at epicentral distances smaller than ~ 1500 km where the arrival of the S-wave was inside the triggering window and detections that appear to be the S-wave higher frequencies or converted seismic phases were detected wrongly increasing the β -values.

The results of this study show that Azores, Cape Verde and Mozambique are areas where dynamic triggered seismic events possibly occur.

The results also suggest that dynamic triggering is not so frequent and common as proposed by previous studies, particularly in the regions of study.

Data from stations deployed in locations better sheltered from cultural noise sources or a method to better constraint cultural noise signals would probably greatly improve the observations and the comprehension of the phenomenon in this regions.

Bibliography

- Aiken, C., and Z. Peng (2014), Dynamic triggering of microearthquakes in three geothermal/volcanic regions of california, *Journal of Geophysical Research: Solid Earth*, 119(9), 2014JB011,218, doi: 10.1002/2014JB011218.
- Aron, A., and J. L. Hardebeck (2009), Seismicity rate changes along the central california coast due to stress changes from the 2003 m 6.5 san simeon and 2004 m 6.0 parkfield earthquakes, *Bulletin of the Seismological Society of America*, 99(4), 2280–2292, doi:10.1785/0120080239.
- Attanayake, J., and J. F. Fonseca (2016), The intraplate mw 7 machaze earthquake in mozambique: Improved point source model, stress drop, and geodynamic implications, *Journal of African Earth Sciences*, 117, 252 – 262, doi:http://dx.doi.org/10.1016/j.jafrearsci.2016.01.027.
- Beier, C., K. M. Haase, and T. H. Hansteen (2006), Magma evolution of the sete cidades volcano, são miguel, azores, *Journal of Petrology*, 47(7), 1375–1411, doi:10.1093/petrology/egl014.
- Beier, C., K. M. Haase, W. Abouchami, M.-S. Krienitz, and F. Hauff (2008), Magma genesis by rifting of oceanic lithosphere above anomalous mantle: Terceira rift, azores, *Geochemistry, Geophysics, Geosystems*, 9(12), Q12,013, doi:10.1029/2008GC002112.
- Beyreuther, M., R. Barsch, L. Krischer, T. Megies, Y. Behr, and J. Wassermann (2010), Obspy: A python toolbox for seismology, *Seismological Research Letters*, 81(3), 530–533, doi:10.1785/gssrl.81.3.530.
- Brodsky, E. E., and S. G. Prejean (2005), New constraints on mechanisms of remotely triggered seismicity at long valley caldera, *Journal of Geophysical Research: Solid Earth*, 110(B4), n/a–n/a, doi:10.1029/2004JB003211.
- Brodsky, E. E., and N. J. van der Elst (2014), The uses of dynamic earthquake triggering, *Annual Review of Earth and Planetary Sciences*, 42(1), 317–339, doi:10.1146/annurev-earth-060313-054648.
- Chao, K., Z. Peng, H. Gonzalez-Huizar, C. Aiken, B. Enescu, H. Kao, A. A. Velasco, K. Obara, and T. Matsuzawa (2013), A global search for triggered tremor following the 2011 mw 9.0 tohoku earthquake, *Bulletin of the Seismological Society of America*, 103(2B), 1551–1571, doi:10.1785/0120120171.
- Chorowicz, J. (2005), The east african rift system, *Journal of African Earth Sciences*, 43(1–3), 379 – 410, doi:http://dx.doi.org/10.1016/j.jafrearsci.2005.07.019, phanerozoic Evolution of Africa.
- Craig, T. J., J. A. Jackson, K. Priestley, and D. McKenzie (2011), Earthquake distribution patterns in africa: their relationship to variations in lithospheric and geological structure, and their rheological implications, *Geophysical Journal International*, 185(1), 403–434, doi:10.1111/j.1365-246X.2011.04950.x.

- Crawford, W. C., A. Rai, S. C. Singh, M. Cannat, J. Escartin, H. Wang, R. Daniel, and V. Combier (2013), Hydrothermal seismicity beneath the summit of lucky strike volcano, mid-atlantic ridge, *Earth and Planetary Science Letters*, 373, 118–128, doi:10.1016/j.epsl.2013.04.028.
- Dirks, P. H., and H. A. Jelsma (2002), Crust–mantle decoupling and the growth of the archaean zimbabwe craton, *Journal of African Earth Sciences*, 34(3–4), 157 – 166, doi:http://dx.doi.org/10.1016/S0899-5362(02)00015-5, 18th Colloquium of African Geology.
- Domingues, A. (2016), Tomography of the east african rift system in mozambique, Ph.D. thesis, Universidade de Lisboa, Instituto Superior Técnico; Birbeck, University of London.
- Domingues, A., G. Silveira, A. M. G. Ferreira, S.-J. Chang, S. Custódio, and J. F. B. D. Fonseca (2016), Ambient noise tomography of the east african rift in mozambique, *Geophysical Journal International*, 204(3), 1565–1578, doi:10.1093/gji/ggv538.
- Dusunur, D., J. Escartín, V. Combier, T. Seher, W. Crawford, M. Cannat, S. C. Singh, L. M. Matias, and J. M. Miranda (2009), Seismological constraints on the thermal structure along the lucky strike segment (mid-atlantic ridge) and interaction of tectonic and magmatic processes around the magma chamber, *Marine Geophysical Researches*, 30(2), 105–120, doi:10.1007/s11001-009-9071-3.
- Dziak, R. P., D. R. Bohnenstiehl, H. Matsumoto, C. G. Fox, D. K. Smith, M. Tolstoy, T.-K. Lau, J. H. Haxel, and M. J. Fowler (2004), P- and t-wave detection thresholds, pn velocity estimate, and detection of lower mantle and core p-waves on ocean sound-channel hydrophones at the mid-atlantic ridge, *Bulletin of the Seismological Society of America*, 94(2), 665–677, doi:10.1785/0120030156.
- Earle, P. S., and P. M. Shearer (1994), Characterization of global seismograms using an automatic-picking algorithm, *Bulletin of the Seismological Society of America*, 84(2), 366–376.
- Engvik, A. K., E. Tveten, B. Bingen, G. Viola, M. Erambert, P. Feito, and S. De Azavedo (2007), P–t evolution and textural evidence for decompression of pan-african high-pressure granulites, lurio belt, north-eastern mozambique, *Journal of Metamorphic Geology*, 25(9), 935–952, doi:10.1111/j.1525-1314.2007.00736.x.
- Faria, B. (2006), Monitorização geofísica e níveis de alerta do vulcão do fogo, Ph.D. thesis, Universidade Técnica de Lisboa, Instituto Superior Técnico.
- Faria, B., and J. F. B. D. Fonseca (2014), Investigating volcanic hazard in cape verde islands through geophysical monitoring: network description and first results, *Natural Hazards and Earth System Sciences*, 14(2), 485–499, doi:10.5194/nhess-14-485-2014.
- Fenton, C. H., and J. J. Bommer (2006), The mw7 machaze, mozambique, earthquake of 23 february 2006, *Seismological Research Letters*, 77(4), 426–439, doi:10.1785/gssrl.77.4.426.
- Fonseca, J. F. B. D., J. Chamussa, A. Domingues, G. Helffrich, E. Antunes, G. v. Aswegen, L. V. Pinto, S. Custódio, and V. J. Manhiça (2014), MOZART: A seismological investigation of the east african rift in central mozambique, *Seismological Research Letters*, 85(1), 108–116, doi:10.1785/0220130082.
- Gaspar, J. L., G. Queiroz, T. Ferreira, A. R. Medeiros, C. Goulart, and J. Medeiros (2015), Chapter 4 earthquakes and volcanic eruptions in the azores region: geodynamic implications from major historical events and instrumental seismicity, *Geological Society, London, Memoirs*, 44(1), 33–49, doi:10.1144/M44.4.

- Gomberg, J., J. L. Rubinstein, Z. Peng, K. C. Creager, J. E. Vidale, and P. Bodin (2008), Widespread triggering of nonvolcanic tremor in california, *Science*, 319(5860), 173–173, doi:10.1126/science.1149164.
- Grantham, G. H., M. Maboko, and B. M. Eglington (2003), A review of the evolution of the mozambique belt and implications for the amalgamation and dispersal of rodinia and gondwana, *Geological Society, London, Special Publications*, 206(1), 401–425, doi:10.1144/GSL.SP.2003.206.01.19.
- Grevemeyer, I., G. Helffrich, B. Faria, G. Booth-Rea, M. Schnabel, and W. Weinrebe (2010), Seismic activity at cadamosto seamount near fogo island, cape verdes - formation of a new ocean island?, *Geophysical Journal International*, 180(2), 552–558, doi:10.1111/j.1365-246X.2009.04440.x.
- Helffrich, G., B. Faria, J. F. B. D. Fonseca, A. Lodge, and S. Kaneshima (2010), Transition zone structure under a stationary hot spot: Cape verde, *Earth and Planetary Science Letters*, 289(1), 156–161, doi:10.1016/j.epsl.2009.11.001.
- Hill, D., and S. Prejean (2007), 4.09 - dynamic triggering, in *Treatise on Geophysics*, edited by G. Schubert, pp. 257 – 291, Elsevier, Amsterdam, doi:http://dx.doi.org/10.1016/B978-044452748-6.00070-5.
- Hill, D. P., P. A. Reasenber, A. Michael, W. J. Arabaz, G. Beroza, D. Brumbaugh, J. N. Brune, R. Castro, S. Davis, D. dePolo, W. L. Ellsworth, J. Gomberg, S. Harmsen, L. House, S. M. Jackson, M. J. S. Johnston, L. Jones, R. Keller, S. Malone, L. Munguia, S. Nava, J. C. Pechmann, A. Sanford, R. W. Simpson, R. B. Smith, M. Stark, M. Stickney, A. Vidal, S. Walter, V. Wong, and J. Zollweg (1993), Seismicity remotely triggered by the magnitude 7.3 landers, california, earthquake, *Science*, 260(5114), 1617–1623, doi:10.1126/science.260.5114.1617.
- Holm, P. M., J. R. Wilson, B. P. Christensen, L. Hansen, S. L. Hansen, K. M. Hein, A. K. Mortensen, R. Pedersen, S. Plesner, and M. K. Runge (2006), Sampling the cape verde mantle plume: Evolution of melt compositions on santo antão, cape verde islands, *Journal of Petrology*, 47(1), 145–189, doi:10.1093/petrology/egi071.
- Ichihara, M., and E. E. Brodsky (2006), A limit on the effect of rectified diffusion in volcanic systems, *Geophysical Research Letters*, 33(2), doi:10.1029/2005GL024753, 102316.
- Kennett, B. L. N., and E. R. Engdahl (1991), Traveltimes for global earthquake location and phase identification, *Geophysical Journal International*, 105(2), 429–465, doi:10.1111/j.1365-246X.1991.tb06724.x.
- Kilb, D., J. Gomberg, and P. Bodin (2000), Triggering of earthquake aftershocks by dynamic stresses, *Nature*, 408(6812), 570–574, doi:10.1038/35046046.
- King, G. C. P., R. S. Stein, and J. Lin (1994), Static stress changes and the triggering of earthquakes, *Bulletin of the Seismological Society of America*, 84(3), 935–953.
- Kusky, T. M. (1998), Tectonic setting and terrane accretion of the archean zimbabwe craton, *Geology*, 26(2), 163–166, doi:10.1130/0091-7613(1998)026<0163:TSATAO>2.3.CO;2.
- Leinweber, V. T., F. Klingelhoefer, S. Neben, C. Reichert, D. Aslanian, L. Matias, I. Heyde, B. Schreckenberger, and W. Jokat (2013), The crustal structure of the central mozambique continental margin — wide-angle seismic, gravity and magnetic study in the mozambique channel, eastern africa, *Tectonophysics*, 599, 170 – 196, doi:http://dx.doi.org/10.1016/j.tecto.2013.04.015.

BIBLIOGRAPHY

- Linde, A. T., and I. S. Sacks (1998), Triggering of volcanic eruptions, *Nature*, 395(6705), 888–890, doi: 10.1038/27650.
- Lodge, A., and G. Helffrich (2006), Depleted swell root beneath the cape verde islands, *Geology*, 34(6), 449–452, doi:10.1130/G22030.1.
- Lourenço, N., J. Luís, and J. M. Miranda (1997), Azores triple junction bathymetry, *Map edited by Science Faculty, Lisbon University and Algarve University, 1 sheet*.
- Manga, M., and E. Brodsky (2006), Seismic triggering of eruptions in the far field: Volcanoes and geysers, *Annual Review of Earth and Planetary Sciences*, 34(1), 263–291, doi:10.1146/annurev.earth.34.031405.125125.
- Masson, D. G., T. P. Le Bas, I. Grevemeyer, and W. Weinrebe (2014), Flank collapse and large-scale landsliding in the cape verde islands, off west africa, *Geochemistry, Geophysics, Geosystems*, 9(7), Q07,015, doi:10.1029/2008GC001983.
- Matthews, M. V., and P. A. Reasenber (1988), Statistical methods for investigating quiescence and other temporal seismicity patterns, *pure and applied geophysics*, 126(2), 357–372, doi:10.1007/BF00879003.
- Mendes, V. B., J. Madeira, A. Brum da Silveira, A. Trota, P. Elosegui, and J. Pagarete (2013), Present-day deformation in são jorge island, azores, from episodic GPS measurements (2001 - 2011), *Advances in Space Research*, 51(8), 1581–1592, doi:10.1016/j.asr.2012.10.019.
- Obara, K. (2002), Nonvolcanic deep tremor associated with subduction in southwest japan, *Science*, 296(5573), 1679–1681, doi:10.1126/science.1070378.
- Okal, E. A. (2008), The generation of t waves by earthquakes, in *Advances in Geophysics*, vol. 49, edited by R. Dmowska, pp. 1–65, Elsevier.
- Peng, Z., and K. Chao (2008), Non-volcanic tremor beneath the central range in taiwan triggered by the 2001 mw 7.8 kunlun earthquake, *Geophysical Journal International*, 175(2), 825–829, doi:10.1111/j.1365-246X.2008.03886.x.
- Peng, Z., J. E. Vidale, A. G. Wech, R. M. Nadeau, and K. C. Creager (2009), Remote triggering of tremor along the san andreas fault in central california, *Journal of Geophysical Research: Solid Earth*, 114, B00A06, doi:10.1029/2008JB006049.
- Peng, Z., J. I. Walter, R. C. Aster, A. Nyblade, D. A. Wiens, and S. Anandkrishnan (2014), Antarctic icequakes triggered by the 2010 maule earthquake in chile, *Nature Geoscience*, 7(9), 677–681, doi: 10.1038/ngeo2212.
- Pim, J., C. Peirce, A. B. Watts, I. Grevemeyer, and A. Krabbenhoft (2008), Crustal structure and origin of the cape verde rise, *Earth and Planetary Science Letters*, 272(1), 422–428, doi:10.1016/j.epsl.2008.05.012.
- Prejean, S. G., D. P. Hill, E. E. Brodsky, S. E. Hough, M. J. S. Johnston, S. D. Malone, D. H. Oppenheimer, A. M. Pitt, and K. B. Richards-Dinger (2004), Remotely triggered seismicity on the united states west coast following the mw 7.9 denali fault earthquake, *Bulletin of the Seismological Society of America*, 94(6B), S348–S359, doi:10.1785/0120040610.

- Pule, T., and I. Saunders (2009), Recent seismicity in the mozambique region and its impact / effects on south africa, *11th SAGA Biennial Technical Meeting and Exhibition Swaziland*, pp. 385–390.
- Rubinstein, J. L., J. E. Vidale, J. Gomberg, K. C. Creager, P. Bodin, S. D. Malone, and A. G. Wech (2007), Non-volcanic tremor and earthquakes driven by the large transient shear stresses of the 2002 denali earthquake, *AGU Fall Meeting Abstracts*, 12.
- Shearer, P. M. (2009), *Introduction to Seismology*, 2 ed., Cambridge University Press.
- Stamps, D. S., E. Calais, E. Saria, C. Hartnady, J.-M. Nocquet, C. J. Ebinger, and R. M. Fernandes (2008), A kinematic model for the east african rift, *Geophysical Research Letters*, 35(5), L05,304, doi:10.1029/2007GL032781.
- Vales, D., N. A. Dias, I. Rio, L. Matias, G. Silveira, J. Madeira, M. Weber, F. Carrilho, and C. Haberland (2014), Intraplate seismicity across the cape verde swell: A contribution from a temporary seismic network, *Tectonophysics*, 636, 325–337, doi:10.1016/j.tecto.2014.09.014.
- van der Elst, N. J., and E. E. Brodsky (2010), Connecting near-field and far-field earthquake triggering to dynamic strain, *Journal of Geophysical Research: Solid Earth*, 115, B07,311, doi:10.1029/2009JB006681.
- Velasco, A. A., S. Hernandez, T. Parsons, and K. Pankow (2008), Global ubiquity of dynamic earthquake triggering, *Nature Geoscience*, 1(6), 375–379, doi:10.1038/ngeo204.
- Wang, B., R. M. Harrington, Y. Liu, H. Yu, A. Carey, and N. J. van der Elst (2015), Isolated cases of remote dynamic triggering in canada detected using cataloged earthquakes combined with a matched-filter approach, *Geophysical Research Letters*, 42(13), 5187–5196, doi:10.1002/2015GL064377, 2015GL064377.
- Watts, A., C. Peirce, J. Collier, R. Dalwood, J. Canales, and T. Henstock (1997), A seismic study of lithospheric flexure in the vicinity of tenerife, canary islands, *Earth and Planetary Science Letters*, 146(3), 431 – 447, doi:http://dx.doi.org/10.1016/S0012-821X(96)00249-X.
- Yang, Z., and W.-P. Chen (2010), Earthquakes along the east african rift system: A multiscale, system-wide perspective, *Journal of Geophysical Research: Solid Earth*, 115, B12,309, doi:10.1029/2009JB006779.
- Zegers, D. Wit, Dann, and White (1998), Vaalbara, earth's oldest assembled continent? a combined structural, geochronological, and palaeomagnetic test, *Terra Nova*, 10(5), 250–259, doi:10.1046/j.1365-3121.1998.00199.x.

Appendices

Appendix A

Determined β -values for all stations and mainshocks in Cape Verde

Station	Mainshock								
	A	B	C	D	F	G	H	J	K
SACV	-	-	-0.345	-	-0.385	0.317			4.301
MAIO				-2.229				2.878	-0.346
MING				-0.680			-1.465	0.532	-0.610
MLOS				-1.134			2.026	1.666	0.253
PATM				0.122				0.479	0.378
SALA				-0.439			0.345	2.668	2.203
PJOR							-1.425	1.269	
SNIC							-1.016	2.363	

Table A.1: Determined β s for all mainshocks for station SACV and stations from the 2002-2004 deployment.

Station	Mainshock										
	D	I	L	M	N	O	P	Q	R	S	T
CVBR1	2.046	0.453	7.349	4.418	-1.056	6.495	-0.049	3.987	-0.840	-1.253	-2.846
CVFG1	0.997	0.737	2.765	4.210	-1.362	5.172	2.044	3.080	-0.059	-2.118	-0.244
CVFG2	0.704	1.727	5.434	5.756	-1.616	2.977	-0.172	1.074	-0.306	-0.724	1.005
CVFG3	2.759	-1.286	2.949	6.406	-1.462	0.942	-0.537	3.975	0.181	-2.867	-1.243
CVFG4	-0.074	0.235	3.243	4.577	-1.395	4.735	1.685	-0.081	2.194	-1.426	-1.857
CVFG5	-0.139	-0.397	5.577	0.666	-1.487		0.365	-0.881	0.068	-2.628	
CVMA1	0.201	0.599	2.475	5.587	-0.916	7.923	3.671	-0.014	-0.145	-0.496	-1.501
CVMA2	1.628	0.699		6.527	0.512	3.086	-0.848	1.633	-0.546	0.118	-2.000
CVMA3	0.900	-0.209	2.132	0.412	-2.424	0.162	0.873		-1.287	-2.023	1.158
CVMA4	-0.655	0.935	0.817			4.316	-0.283		-0.973	-1.529	-2.017
CVST2	0.516	-0.812	2.893	4.014	-0.570	0.842	1.889	2.315	0.795	-2.604	-3.190
CVST3	0.271			5.740			1.070				
CVST4	-0.153	-0.786	0.231	0.299	-0.892	-1.115	-1.242	-0.662	0.132	1.300	1.884
CVST5	2.425	-1.158	4.332	5.488	-2.687	3.038	2.749	4.257	0.679	-4.540	-1.453
CVBV1	2.458	-0.112	5.098	5.890	0.014	1.011	3.802	4.671	-0.008	-2.268	-2.991
CVBV2	0.204	1.352	1.478	1.894	-3.046	1.376	3.869	-0.716	0.063	-1.070	0.660
CVBV4	-0.144	-1.156	-0.175	-1.388	-2.107	2.489	5.617	0.721	2.353	-0.283	-2.653
CVBV5	-0.708	0.382	-0.430	-0.351			1.174		0.007		
CVBV6	0.804	-0.621	-1.501	-0.441	-0.426	2.702	6.299	-0.470	0.061	0.703	-0.510
CVSA1	0.689	0.707	2.796	3.028	-0.973	4.845	3.030	3.821	1.311	-4.402	-2.978
CVSA2	0.971	1.249	1.664	7.195	0.584	-0.301	1.416	6.689	0.797	-2.440	-2.876
CVSA3	0.272	0.379	2.991	4.008	0.165	2.326	2.719	4.063	0.937	-0.557	-1.062
CVSA4	0.394	0.971	2.838	5.483	-1.825	3.265	-0.960	3.441	0.848	-2.164	-2.608
CVSA5	-0.643	-0.158	-2.170	0.732	-0.740	1.160	-0.296	-0.158	-1.222	-1.967	0.124
CVSA6	0.510	-1.066	-0.956	-2.353	0.236	-0.026	-2.164	-1.848	2.194	2.836	2.511
CVSL1	0.072	-0.033	-1.933	3.835	-1.470	1.151	0.357	2.454	-0.562	0.289	-2.828
CVSL2	-1.046	0.319	0.924	3.819	0.420	0.805	2.150	1.851		0.412	-1.718
CVSL3	0.905			8.985	-1.646		6.653	0.369			
CVSL4	0.290	0.226	-1.424	4.665	-1.176	0.292	1.656	4.363	0.761	-3.287	-2.566
CVSN1	1.282	0.016	7.816	6.100	-0.997	2.996	1.619	6.164	0.291	-3.219	-1.431
CVSN2	3.094	1.487	-0.982	1.641	-1.461	5.153	0.166	2.817	0.518	-	-0.722
CVSN3	0.946	0.017	1.164	5.877	-1.140	1.532	3.388	0.108	-1.140	-2.227	-1.414
CVSN4	0.152	0.962	1.576	0.915	-0.390	-0.902	-1.033	1.296	-0.051	-0.055	1.423
CVST1	0.655	-0.015	3.724	2.693	-0.919	2.690	2.218	0.938	0.070	-0.438	
CVSV1	4.055	6.458	0.107	10.280	-2.762	4.670	5.966	0.922	0.304	-1.081	-
CVSV2	1.360	0.360	1.275	6.754	-0.284	2.909	3.526	0.412	-0.698	0.468	-1.314
CVSV3	0.877	0.901	2.429	1.302	-0.399		3.107	0.530	0.031	-0.715	
CVSV4	0.282	1.183	1.304	4.319	-2.311	4.234	1.390	3.261	-0.309	-2.747	-2.035

Table A.2: Determined β s for all mainshocks for stations from the 2007-2008 deployment.

Appendix B

Determined β -values for all stations and mainshocks in Mozambique

Station	Mainshock			
	A	B	C	D
A0293				-0.251
A0302			-1.816	2.801
A0789	1.659	-0.831		
A1030	-0.890	0.340	-0.196	-0.502
3869	-0.115	-1.144		
3870	-1.035	0.117		
3G86	-0.301	1.663		1.257
A0282	0.968	0.317	-	1.314
A0770	1.249	0.241	-0.133	0.209
A0805	-4.534	-2.088	1.243	-0.913
3878	-0.281	-1.307		
A0818	-0.621	0.714		
3434	4.865	2.165		
3A16	2.776	0.387	-0.006	2.327
3901	2.252	-1.043	-1.170	0.865
MAPH			-1.032	-0.376
MSGR				2.322

Table B.1: Determined β s for all mainshocks for the 5 Hz high-pass filtered data in Mozambique.

Station	Mainshock			
	A	B	C	D
A0293				2.182
A0302			-1.721	2.801
A0789	-0.933	0.362		
A1030	-0.381	0.829	-0.331	2.181
3869	1.468	-2.070		
3870	2.751	0.570		
3G86	0.404	0.366		-0.363
A0282	-1.567	0.761	-	2.002
A0770	-1.382	-2.133	0.578	-2.015
A0805	1.166	-0.658	0.407	-0.496
3878	0.045	0.173		
A0818	-1.030	-0.968		
3434	3.391	1.511		
3A16	4.505	0.907	2.942	-0.041
3901	2.207	0.301	-0.480	-0.455
MAPH			-1.101	-1.247
MSGR				0.272

Table B.2: Determined β s for all mainshocks for the 3-5 Hz band-pass filtered data in Mozambique.

Appendix C

Determined β -values for all stations and mainshocks in Lucky Strike volcano

	Mainshock	
Station	C	L
LSd1	-2.734	-2.922
LSd2	0.0209	-2.619
LSd3	-3.504	-7.868
LSd4	-3.796	-2.329

	Mainshock				
Station	A	B	D	F	K
LSc1	-1.534	-1.551	7.569	-0.157	-1.049
LSc2	-1.082		-1.157	-0.310	-4.832
LSc3	-1.577	-1.629	-2.086	1.067	-4.645
LSc4	-1.250	-1.522	-3.717	-1.210	6.939
LSc7	1.188	-1.396	-0.023	2.916	0.007

	Mainshock				
Station	E	G	H	I	J
LSo1	0.421	10.839	-1.997	-1.336	-1.186
LSo2	2.299	1.464	4.694	-0.588	-1.946
LSo3	-0.468	-2.731	-7.666	-2.585	1.050
LSo4	-0.078	0.037	0.662	1.697	3.464
LSo7	-0.410	-2.723	-3.018	-0.485	-0.485
LSo8	1.715	1.181	-1.523	2.048	-2.990

Table C.1: Determined β 's for all mainshocks for all the OBS deployments.

Appendix D

Determined β -values for all stations and mainshocks in Azores

APPENDIX D. DETERMINED β -VALUES FOR ALL STATIONS AND MAINSHOCKS IN AZORES

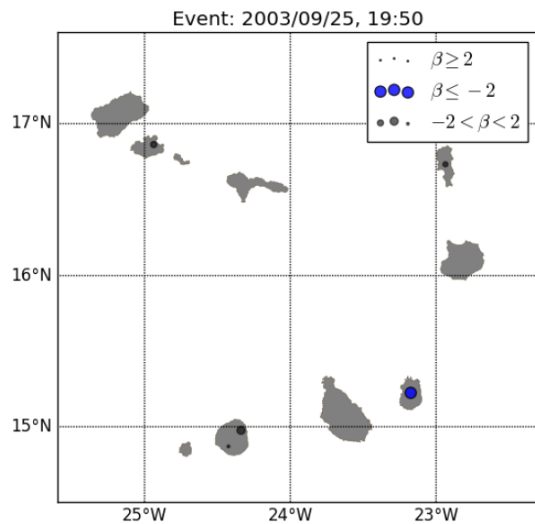
Mainshock	Station	
	CMLA	ROSA
A	4.176	
B	-1.233	0.295
C		-0.203
D	0.767	
E	-1.880	
F	-0.250	
G	-0.772	-0.570
H	1.421	
I	2.358	-1.078
J	5.066	
K	3.532	
L	0.172	
M	-2.797	-1.074
N	-1.180	0.537
O	-0.166	-0.876
P	-0.270	
Q	3.045	
R	-0.842	1.467
S	-0.089	
T	-0.712	-0.019
U	-0.145	1.631
V	-1.467	
W	-0.452	
V	-1.467	
X	1.110	0.148
Y	0.778	
Z	-0.550	-1.665
AA	-2.058	-0.780
BB	-0.671	
CC	-1.313	-0.803
DD	2.689	-1.366
EE	-0.964	
FF	-0.437	
GG	2.130	
HH	-1.208	0.673

Table D.1: Determined β 's for all mainshocks in Azores.

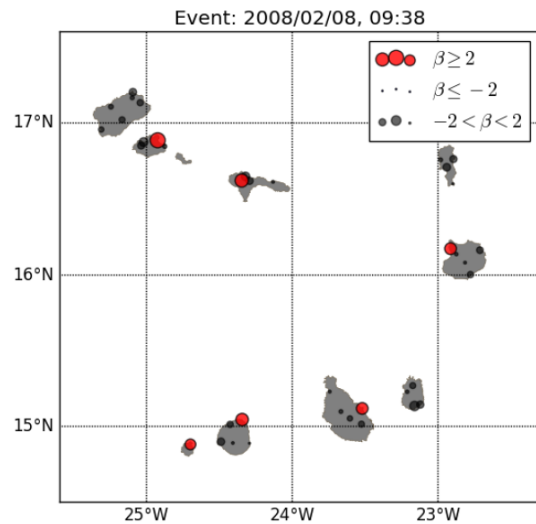
Appendix E

Maps of β for all events analyzed in more than one station in Cape Verde not present in main text

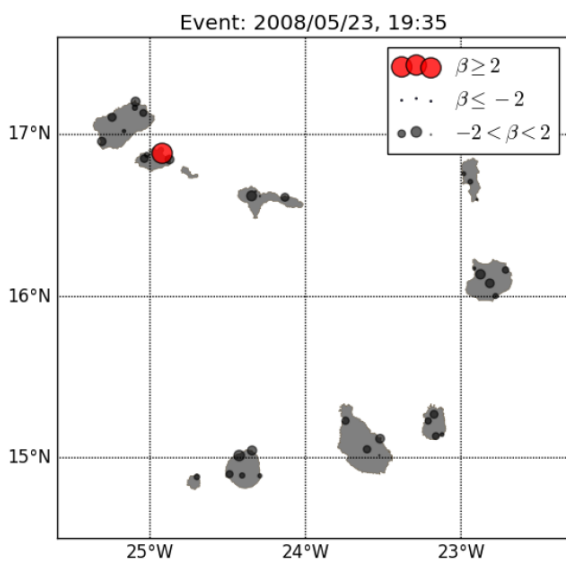
APPENDIX E. MAPS OF β FOR ALL EVENTS ANALYZED IN MORE THAN ONE STATION IN CAPE VERDE NOT PRESENT IN MAIN TEXT



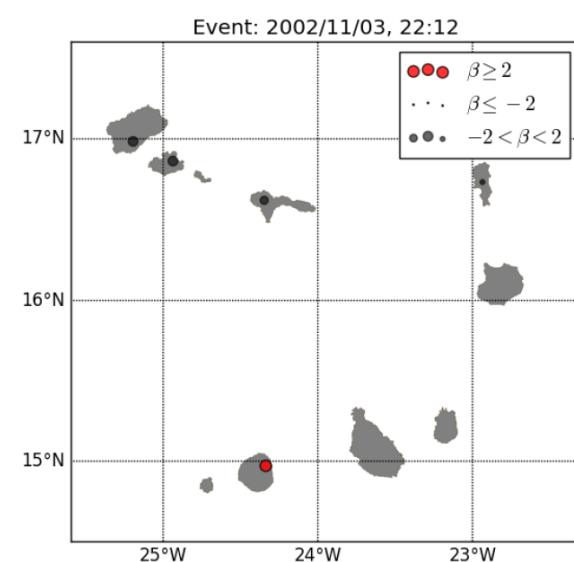
Mainshock D



Mainshock E

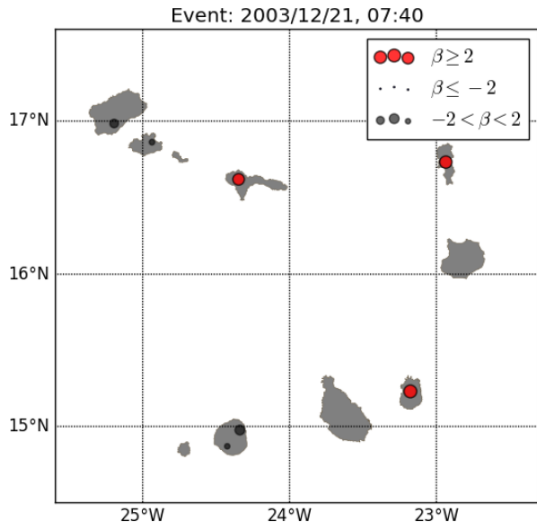


Mainshock H

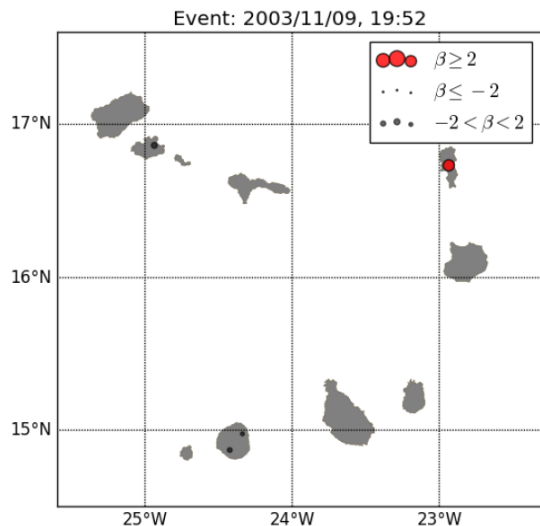


Mainshock I

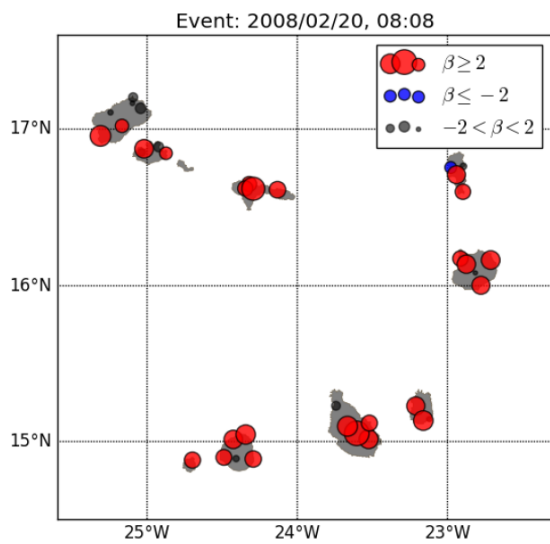
APPENDIX E. MAPS OF β FOR ALL EVENTS ANALYZED IN MORE THAN ONE STATION IN CAPE VERDE NOT PRESENT IN MAIN TEXT



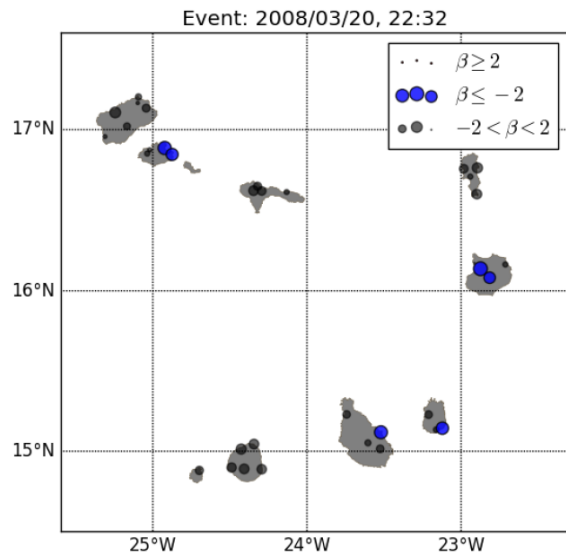
Mainshock J



Mainshock K

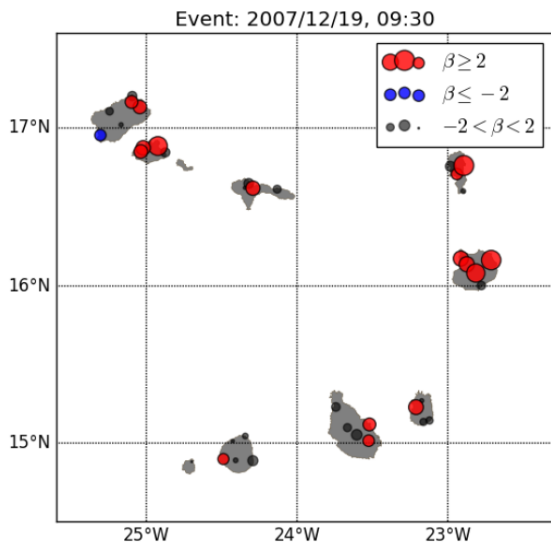


Mainshock M

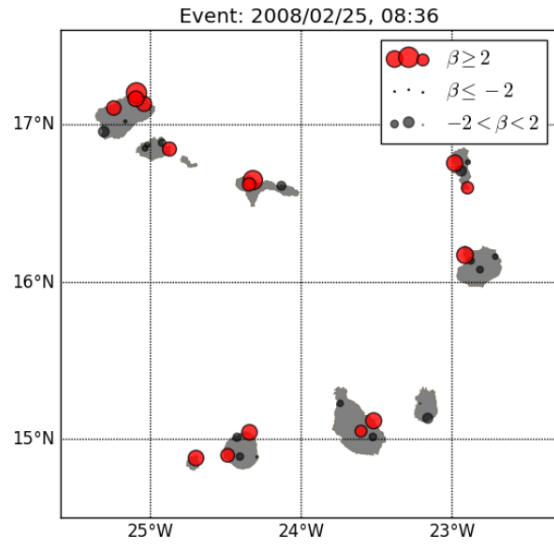


Mainshock N

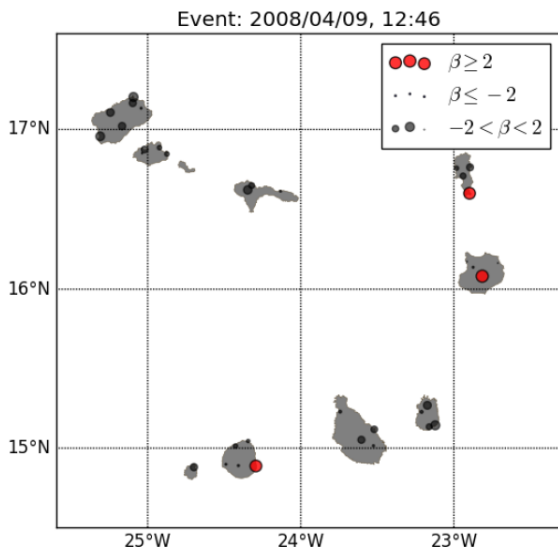
APPENDIX E. MAPS OF β FOR ALL EVENTS ANALYZED IN MORE THAN ONE STATION IN CAPE VERDE NOT PRESENT IN MAIN TEXT



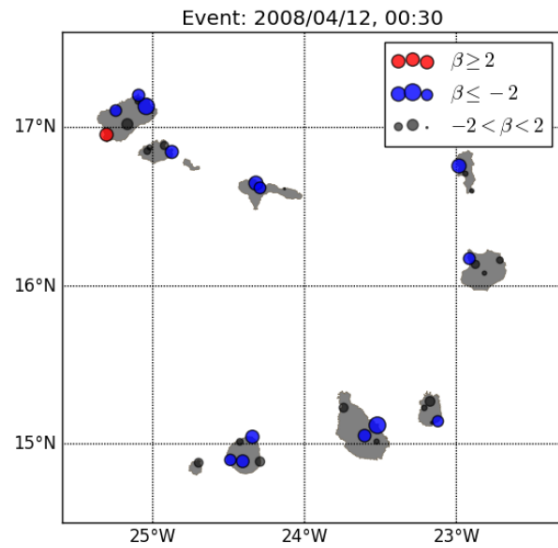
Mainshock P



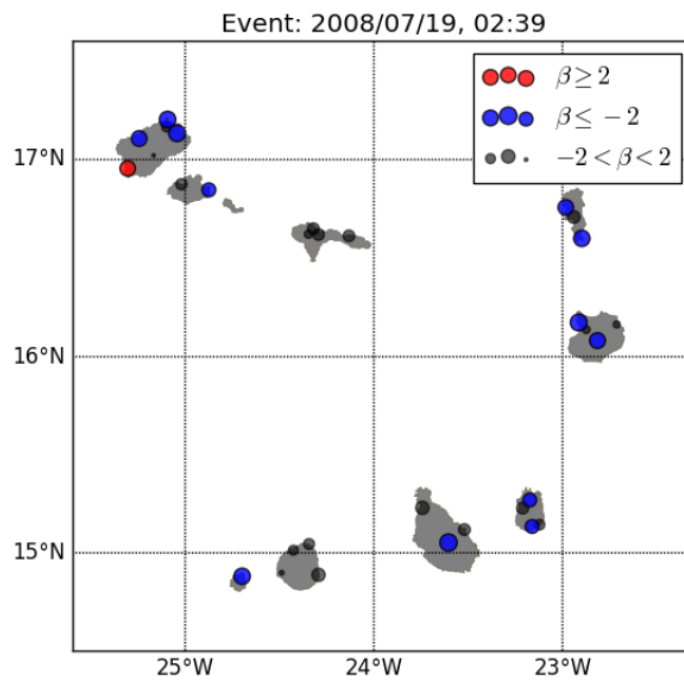
Mainshock Q



Mainshock R



Mainshock S



Mainshock T

Appendix F

Stations coordinates

APPENDIX F. STATIONS COORDINATES

Station	Longitude	Latitude	Depth (m)	Elevation (m)
SACV	-22.936	16.733	97	387
MAIO	-23.177	15.231	0	91
MING	-24.937	16.863	0	1000
MLOS	-24.338	14.976	0	1650
PATM	-24.424	14.869	0	570
PJOR	-25.194	16.984	0	659
SALA	-22.936	16.733	0	60
SNIC	-24.347	16.620	0	1092
CVBR1	-24.698	14.880	0	473
CVBR2	-24.722	14.849	0	622
CVBV1	-22.914	16.174	0	17
CVBV2	-22.875	16.138	0	47
CVBV4	-22.815	16.082	0	74
CVBV5	-22.778	16.003	0	39
CVBV6	-22.713	16.164	0	37
CVFG1	-24.489	14.898	0	201
CVFG2	-24.426	15.014	0	243
CVFG3	-24.343	15.045	0	25
CVFG4	-24.293	14.888	0	323
CVFG5	-24.407	14.890	0	929
CVMA1	-23.211	15.229	0	20
CVMA2	-23.161	15.135	0	56
CVMA3	-23.122	15.144	0	29
CVMA4	-23.173	15.270	0	35
CVSA1	-25.043	17.133	0	301
CVSA2	-25.093	17.202	0	29
CVSA3	-25.097	17.165	0	117
CVSA4	-25.243	17.106	0	314
CVSA5	-25.167	17.021	0	370
CVSA6	-25.310	16.957	0	23
CVSL1	-22.898	16.601	0	19
CVSL2	-22.940	16.709	0	38
CVSL3	-22.894	16.763	0	23
CVSL4	-22.983	16.758	0	15
CVSN1	-24.321	16.650	0	251
CVSN2	-24.347	16.622	0	1058
CVSN3	-24.293	16.620	0	124
CVSN4	-24.132	16.614	0	57
CVST1	-23.525	15.015	0	206
CVST2	-23.604	15.053	0	333
CVST3	-23.666	15.098	0	569
CVST4	-23.743	15.230	0	32
CVST5	-23.520	15.119	0	49
CVSV1	-24.923	16.886	0	67
CVSV2	-25.020	16.875	0	35
CVSV3	-25.036	16.852	0	84
CVSV4	-24.874	16.846	0	24

Table F.1: Coordinates of the stations in Cape Verde.

Station	Longitude	Latitude	Elevation (m)
A0786	33.159	-18.060	628
3A21	33.173	-18.040	616
A0302	34.172	-17.958	352
A0781	35.416	-17.799	71
A0789	34.233	-19.002	82
A1032	34.050	-18.511	679
A1025	34.738	-18.819	151
A0293	32.884	-18.948	781
A0297	33.842	-19.220	281
3522	34.608	-19.525	8
A1030	33.292	-19.422	628
3869	35.011	-19.716	14
3870	34.467	-19.863	32
3G86	33.652	-20.291	119
3A17	32.771	-20.456	985
3433	33.368	-20.824	250
A0282	34.064	-20.636	64
A0295	34.960	-21.006	9
3G93	32.921	-21.589	185
A0770	33.863	-21.421	65
3G66	34.124	-22.052	166
A0805	33.264	-22.635	93
4658	34.378	-23.097	100
3878	35.229	-23.882	45
3A19	34.189	-24.924	112
A0818	33.008	-24.510	32
3527	31.014	-22.690	501
3434	31.222	-22.947	321
3A16	31.390	-24.477	452
3901	31.447	-25.427	354
MAPH	35.080	-22.250	42
MSGR	32.180	-23.830	135

Table F.2: Coordinates of the stations in Mozambique.

Station	Longitude	Latitude
O1 1	-32.232	37.277
O2 1	-32.265	37.328
O3 1	-32.334	37.305
O4 1	-32.289	37.291
O7 1	-32.301	37.256
O8 1	-29.007	37.483
O1 2	-32.278	37.322
O2 2	-32.324	37.298
O3 2	-32.288	37.292
O4 2	-32.241	37.283
O7 2	-32.297	37.297
C1	-32.277	37.322
C2	-32.324	37.299
C3	-32.288	37.293
C4	-32.241	37.283
C7	-32.297	37.261
D1	-32.279	37.320
D2	-32.297	37.297
D3	-32.242	37.280
D4	-32.294	37.261

Table F.3: Coordinates of the OBS stations deployed in Lucky Strike volcano.

Station	Longitude	Latitude	Depth (m)	Elevation (m)
ROSA	-25.524	37.764	0	310
CMLA	-28.247	38.721	97	429

Table F.4: Coordinates of the stations deployed in Azores.

Appendix G

**Fittings for the analysis made in section
6.1.3. Results are shown in table 6.6**

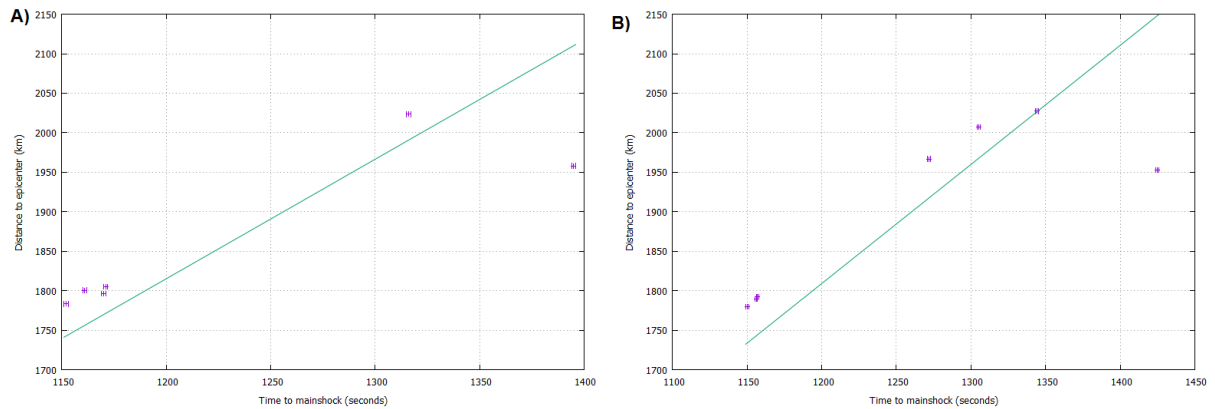


Figure G.1: Nonlinear least-squares Marquardt-Levenberg fitting of $r = vt$ linear function (green line) to the distance of the stations to the epicenter (r) and the determined arrival times (t) of the observed second burst (in purple) for mainshock **J** (A) and mainshock **K** (B) (section 6.1.3). The fitting parameter corresponds average propagation speed with a result of 1.508 ± 0.027 km/s for mainshock **J** and 1.513 ± 0.026 km/s for mainshock **K**.

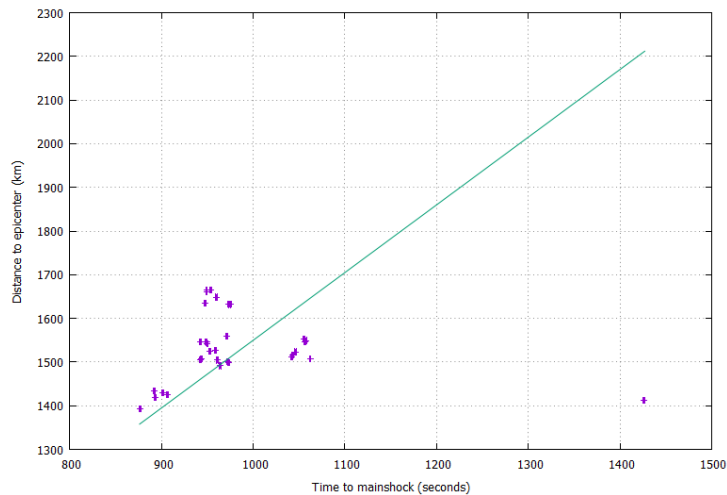


Figure G.2: Nonlinear least-squares Marquardt-Levenberg fitting of $r = vt$ linear function (green line) to the distance of the stations to the epicenter (r) and the determined arrival times (t) of the observed second burst (in purple) for mainshock **I**. The fitting parameter corresponds average propagation speed with a result of 1.550 ± 0.030 km/s.